FIRST MEASUREMENT OF DEEPLY VIRTUAL COMPTON SCATTERING WITH A POLARIZED PROTON TARGET

Name: Shifeng Chen
Department: Department of Physics
Major Professor: Paul Eugenio
Degree: Doctor of Philosophy
Term Degree Awarded: Spring, 2006

Target Spin Asymmetry is first measured in the exclusive Deeply Virtual Compton Scattering (DVCS). The asymmetry is the results of interference between the DVCS and the Bethe-Heitler (BH) process, and gives access to the Generalized Parton Distributions (GPD) $\widetilde{\mathcal{H}}$ and $\mathcal{H}$. The data were recorded with the CLAS detector at the Thomas Jefferson National Accelerator Facility. Both the electron beam (of energy 5.7 GeV) and the solid NH_3 target were longitudinally polarized. Exclusive DVCS events were selected by requiring identifying the scattered electron, recoil proton, and detected photon. Monte-Carlo (MC) simulation is studied to estimate the background from π^0 events. The acceptance corrected single photon asymmetry is well described by the function $F = p_0 sin\phi + p_1 sin2\phi$ with $p_0 = 0.252 \pm 0.042^{stat} \pm 0.020^{sys}$ and $p_1 = -0.022 \pm 0.045^{stat} \pm 0.021^{sys}$. This result agrees rather well with the predictions of a model of GPDs.

THE FLORIDA STATE UNIVERSITY

COLLEGE OF ARTS AND SCIENCES

FIRST MEASUREMENT OF DEEPLY VIRTUAL COMPTON SCATTERING WITH A POLARIZED PROTON TARGET

By

SHIFENG CHEN

A Dissertation submitted to the
Department of Physics
in partial fulfillment of the
requirements for the degree of
Doctor of Philosophy

Degree Awarded:
Spring Semester, 2006

The members of the Committee approve the dissertation of Shifeng Chen defended on February 28, 2006.

Paul Eugenio
Professor Directing Dissertation

Steve Bellenot
Outside Committee Member

Todd Adams
Committee Member

Simon Capstick
Committee Member

Larry Dennis
Committee Member

Alexander Ostrovidov
Committee Member

The Office of Graduate Studies has verified and approved the above named committee members.

To my wife, Erhong Hu, and my daughter, Leah Yujia Chen

ACKNOWLEDGEMENTS

The first person I would like to thank is my advisor, Dr. Paul Eugenio, for his continuous advise, encouragement, and support throughout my graduate school years. He was always ready to offer his help to me on physics, and computing skills, even before he was my advisor. With his encouragement and inspiration I always feel confident in my work, and have enjoyed working with him. Outside of physics, he was always there as a friend.

The next person I would like to acknowledge is my former advisor, Dr. Larry Dennis. It was he who attracted me to nuclear physics. He showed amazing patience in guiding me. After he left the physics department, he always sacrificed his weekend to advise me. I thank him for revising my proposal, conference proceeding, and talk rehearsal. Especially I thank him for writing reference letters several times for my wife's and my visa applications. He is always kind and understanding. I feel I really owe him a lot.

Next, I would like to thank my collaborator, Dr. Volker Burkert, for his tireless work helping me. From the very beginning to the end of the work, as a DVCS expert, Dr. Burkert was always there to answer my physics questions. Without his help it is hard to believe that this work could have been done smoothly.

Next, I would like to thank my collaborator, Dr. Harut Avakian, for his invaluable assistance. He helped me perform the Monte Carlo simulations. He answered thousands of my questions, and when I had difficulties, he always repeated my work to reproduce my errors to help me figure out the problem.

Also, I would like to thank the former and current people in the hadronic nuclear physics group, Dr. Simeon McAleer, Dr. Steve Barrow, Dr. Alexander Ostrovidov, Dr. Volker Crede, Dr. Gregg Riccard, Philip Coltharp, Burnham Stokes, Blake Sharin, Lukasz Blaszczyk, Charles Hanretty. I thank Dr. Simeon McAleer and Dr. Steve Barrow for helping familiarize me with Jefferson Lab. I thank Dr. Alexander Ostrovidov in helping me on both physics and computer skills. I wish to thank Philip Coltharp for his kindness and friendship.

Next, I would like to thank the people in EG1b working group, Gail Dodge, Sebastian Kuhn, Peter Bosted, Angela Biseli, Vipuli Dharmawardane, Yelena Prok, Tony Forest, Ralph Minehart, Raffaella De Vita, Alexandre Deur, Robert Fersch, and Sharon Careccia, etc. I benefited greatly from their helpfulness.

Of course, I would like to thank the Jefferson Lab physicists and professors from other Universities for helping me on this work, in particular, Stepan Stepanya, Latifa Elouhadri, L. Cole Smith, Dennis Weygand, Arne Freyberger, and Mark Ito. I would like to thank L. Cole Smith and Hyon-Suk Jo for teaching me to use GSIM.

Finally, I would like to thank my committee members, Dr. Todd Adams, Dr. Steve Bellenot, and Dr. Simon Capstick.

TABLE OF CONTENTS

LIST OF TABLES

LIST OF FIGURES

ABSTRACT

Target Spin Asymmetry is first measured in the exclusive Deeply Virtual Compton Scattering (DVCS). The asymmetry is the results of interference between the DVCS and the Bethe-Heitler (BH) process, and gives access to the Generalized Parton Distributions (GPD) $\widetilde{\mathcal{H}}$ and $\mathcal{H}$. The data were recorded with the CLAS detector at the Thomas Jefferson National Accelerator Facility. Both the electron beam (of energy 5.7 GeV) and the solid NH_3 target were longitudinally polarized. Exclusive DVCS events were selected by requiring identifying the scattered electron, recoil proton, and detected photon. Monte-Carlo (MC) simulation is studied to estimate the background from π^0 events. The acceptance corrected single photon asymmetry is well described by the function $F = p_0 sin\phi + p_1 sin2\phi$ with $p_0 = 0.252 \pm 0.042^{stat} \pm 0.020^{sys}$ and $p_1 = -0.022 \pm 0.045^{stat} \pm 0.021^{sys}$. This result agrees rather well with the predictions of a model of GPDs.

CHAPTER 1

INTRODUCTION

1.1 Introduction

Since the electromagnetic form factors were first measured on the proton [1] in the 1950s, both form factors and parton distributions have been measured using exclusive processes and inclusive processes respectively. Elastic electron scattering measures the Q^2 dependence of form factors which give us information about the nucleons' charge and current distributions, while Deep Inelastic Scattering (DIS) measures the x dependence of structure functions which give us the information about the internal composition of the nucleon, such as the quark's longitudinal momentum and helicity distributions. Both form factors (t dependence) and parton distribution functions (x dependence) represent different one-dimensional projections of the nucleon's internal structure, that, until recently seemed to be unconnected.

The recently developed formalism of "Generalized Parton Distributions" (GPDs)[2, 3, 4, 5] relates the $x-$ and $t-$dependence of the parton distributions and the form factors. In the forward limit, the GPDs can be reduced to the usual parton distributions, and with a sum rule, the first moment of GPDs can be related to the form factors. In addition to the parton distributions and form factors, GPDs contain more information, which so far is unmeasured, such as, the quark orbital angular momentum contribution of nucleon's spin, the interference between quarks, the transverse parton distributions, etc. Therefore, GPDs provide a unified description of a hadron structure.

The GPDs can be accessed in hard exclusive processes. One of the simplest processes is Deeply Virtual Compton Scattering (DVCS) in which electrons scatter off the proton in hard processes producing a real photon. DVCS can be described in terms of GPDs.

First experimental results on beam spin asymmetry of DVCS have been reported from both CLAS[6] and HERMES[7] collaborations. A broad program for studying GPDs via DVCS is proposed for CLAS at 6 GeV [8] as well as at the energy upgrade at CLAS-12[9].

In this work, we measured target spin asymmetry in the reaction $\vec{e}\vec{p} \rightarrow ep\gamma$. The data for this analysis are from EG1b which were taken from Sep. 2000 through Apr. 2001 with both longitudinally polarized electron beam and longitudinally polarized proton target.

1.2 Generalized Parton Distributions

GPDs were first introduced by F.M. Dittes, and D. Müller, et al. (see Ref[2, 3]). The physical significance on GPDs were unclear until Ji's discovery[4] that GPDs provide access to the quark orbital angular momentum contribution of nucleon's spin, which is unknown so far. In the past few years, both experimental and theoretical physicists have shown strong interest in GPDs, and the full picture of the role of GPDs in nucleon structure has emerged. Fig. 1.1 visualizes the relationship between GPDs and hard exclusive processes. More reviews of GPDs can be found in Ref[11, 12, 13, 14, 15].

1.2.1 Notations

To define GPDs, we naturally use light-cone coordinates which are defined by,

$$v^{+} = \frac{1}{\sqrt{2}}(v^{0} + v^{3}), \tag{1.1}$$

$$v^{-} = \frac{1}{\sqrt{2}}(v^{0} - v^{3}), \tag{1.2}$$

$$\mathrm{v}_{\perp} = (v^{1}, v^{2}) \tag{1.3}$$

for any four-vector v, and $\mathrm{v}_{\perp}$ is the two dimensional transverse vector.

For hard exclusive processes where GPDs appear we use the common notation

$$\bar{P} = \frac{p + p'}{2}, \qquad \Delta = p' - p, \qquad t = \Delta^{2}, \tag{1.4}$$

where p and p' are the four-momenta of the initial and final nucleon, respectively. For $\gamma^{*}p$ collisions (see Fig 1.2) we have the standard variables

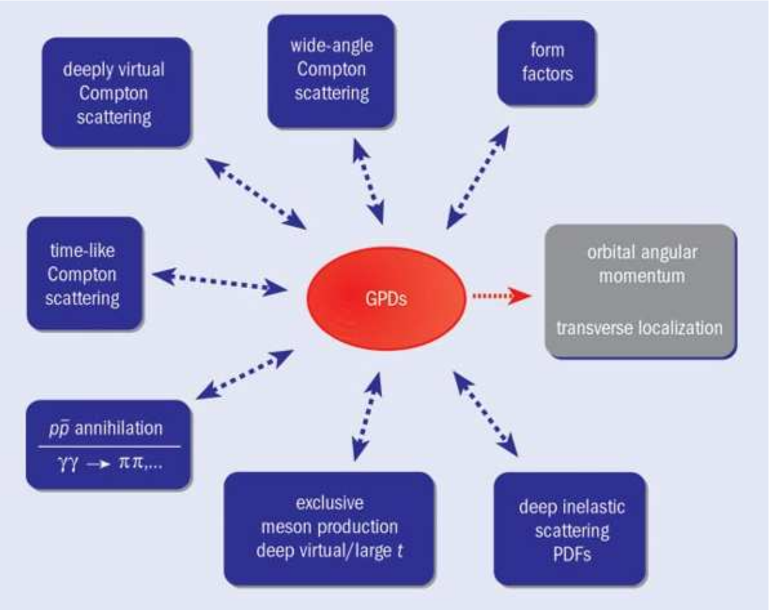

Figure 1.1. Schematic overview of different hard processes and fundamental observables related to GPDs. Figure taken from Ref[10]

$$Q^2 = -q^2, \qquad W^2 = (p+q)^2, \qquad x_B = \frac{Q^2}{2(p \cdot q)}, \tag{1.5}$$

with q for the virtual photon γ^* four-momentum. Here, W is the hadronic mass, and x_B, the Bjorken scaling variable, represents the inelasticity of the process.

In the calculation of exclusive cross section, we define the Center of Momentum System (CMS) using virtual photon (q) and the average momentum of initial nucleon and final nucleon ($\bar{P}$), in order that $\bar{P}$ and virtual photon are collinear along z-axis and in opposite direction.

Another two variables related to GPDs are skewedness variable ξ and the averaged momentum fraction of the quark x,

$$\xi = -\frac{\Delta^+}{2\bar{P}^+} = \frac{p^+ - p'^+}{p^+ + p'^+} \tag{1.6}$$

where Δ^+, $\bar{P}^+$, p^+, and p'^+ are light-cone four-momenta.

$$x = \frac{k^+}{\bar{P}^+} \tag{1.7}$$

where k is the quark loop momentum. From the above definitions, it is easy to see that ξ is the longitudinal fraction of the four momentum transfer Δ, and x is the average momentum fraction carried by a struck quark in the quark loop. Both ξ and x will be used to parameterize GPDs functions.

1.2.2 Definitions of GPDs

One way to define GPDs is to start from hard exclusive reactions, such as DVCS or Deeply Virtual Meson Production (DVMP), see Fig. 1.2. Factorization allows to separate the amplitude for hard exclusive processes into a hard-scattering part, which is exactly calculable in pQCD, and a non-perturbative nucleon structure (represented by the lower blobs in Fig. 1.2) described by GPDs. In Fig. 1.2, DVCS is described with a so-called hand-bag diagram: a quark with plus-momentum $(x+\xi)\bar{P}^+$ absorbs a virtual photon, produces a real photon, and the quark plus-momentum becomes $(x-\xi)\bar{P}^+$.

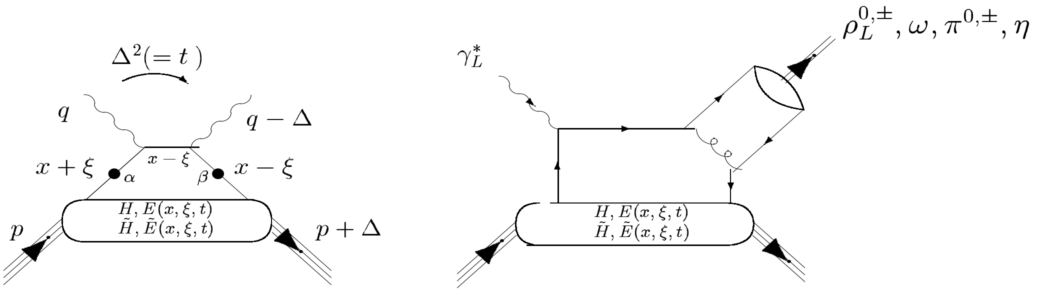

Figure 1.2. Hand-bag diagrams for DVCS (left) and meson production (right).

Through light-cone matrix elements of the quark operators, the non-perturbative amplitude (represented by the lower blobs of Fig. 1.2) can be parameterized as[16]:

$$\begin{aligned}
&\frac{\bar{P}^+}{2\pi}\int dy^- e^{ix\bar{P}^+y^-}\langle p^{'}|\bar{\psi}_\beta(-y/2)\psi_\alpha(y/2)|p\rangle\bigg|_{y^+=\vec{y}_\perp=0} \\
=\ &\frac{1}{4}\Big\{(\gamma^-)_{\alpha\beta}\Big[H^q(x,\xi,t)\ \bar{N}(p^{'})\gamma^+N(p) \\
&\qquad\qquad + E^q(x,\xi,t)\ \bar{N}(p^{'})i\sigma^{+\kappa}\frac{\Delta_\kappa}{2m_N}N(p)\Big] \\
&+(\gamma_5\gamma^-)_{\alpha\beta}\Big[\tilde{H}^q(x,\xi,t)\ \bar{N}(p^{'})\gamma^+\gamma_5N(p) \\
&\qquad\qquad + \tilde{E}^q(x,\xi,t)\ \bar{N}(p^{'})\gamma_5\frac{\Delta^+}{2m_N}N(p)\Big]\Big\}, \qquad (1.8)
\end{aligned}$$

where $N(p)$ and $N(p')$ are nucleon spinors, ψ is the quark field, q is the flavor of the struck quark (u, d, s), and m_N is the nucleon mass. The left hand side of Eq. (1.8) is a Fourier integral which transforms the matrix element from light-cone distance y^- into momentum space $\bar{P}^+$. The physical model is hand-bag diagram, and it can be interpreted as the process that at the space-time $y/2$ one quark is taken out, and then returns to the nucleon at space-time $-y/2$. At leading twist accuracy, the right hand side of Eq. (1.8) parametrizes the nucleon structure (represented by lower blob) as four GPDs, i.e., the unpolarized distributions H^q, E^q, and the polarized distributions $\tilde{H}^q$, $\tilde{E}^q$, which depend upon x, ξ and t.

As an example, Fig. 1.3 shows GPD H as functions of x, ξ and t at $t = 0$ point.

1.2.3 Properties of GPDs

In the Fig. 1.2, the active quark longitudinal momentum is $(x+\xi)\bar{P}^+$ in the initial nucleon and $(x-\xi)\bar{P}^+$ in the final nucleon. The variable x is between -1 to 1, and variable ξ runs from 0 to 1. Therefore, both $x+\xi$ and $x-\xi$ can be either positive or negative. Since the positive (negative) momentum corresponds to the quark (anti-quark), there are three regions for the GPDs:

- for $x > \xi$, both partons are quarks.
- for $x < -\xi$, both partons are anti-quarks.
- $-\xi < x < \xi$, the initial parton is a quark and the final one an anti-quarks.

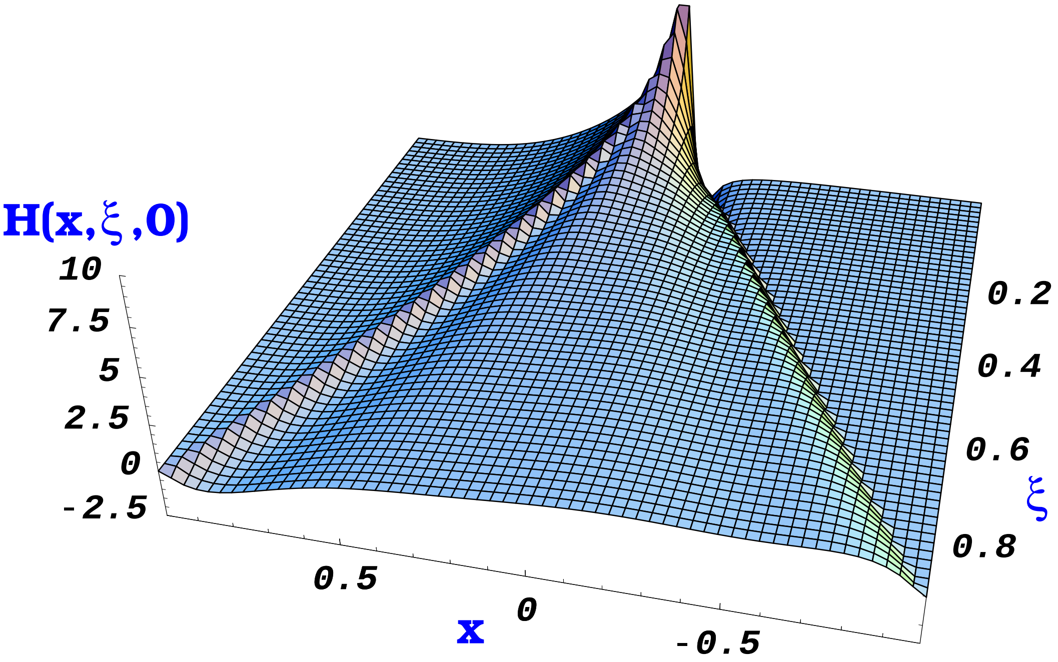

Figure 1.3. GPD $H(x,\xi,t)$ at $t=0$ calculated using the model of Ref. [17]

Since $-\xi < x < \xi$ is absent in Deeply Inclusive Scattering (DIS), we only think about the regions $x < -\xi$ and $x > \xi$. In these two regions, the GPDs are generalized descriptions of the usual parton distributions which are measured by DIS. Actually, in the forward limit (Defined by $\Delta = 0$), the GPDs H reduce to the well-known quark density distribution $q(x)$, and GPDs $\tilde{H}$ reduces to the well-known quark helicity distribution $\Delta q(x)$:

$$H^q(x,0,0) = \begin{cases} q(x), & x > 0\,, \\ -\bar{q}(-x), & x < 0\,. \end{cases} \tag{1.9}$$

$$\tilde{H}^q(x,0,0) = \begin{cases} \Delta q(x), & x > 0\,, \\ \Delta\bar{q}(-x), & x < 0\,. \end{cases} \tag{1.10}$$

Since the GPDs E and $\tilde{E}$ are not measurable in DIS, they are new distribution functions at twist-2 level.

Besides the connection to the usual parton distributions, the GPDs are related to the other nucleon structure quantities. At finite momentum transfer (Δ), the first moments of the GPDs give the elastic form factors of the nucleon through sum rules[4].

$$\begin{aligned}\int_{-1}^{+1} dx\, H^q(x,\xi,t) &= F_1^q(t)\,, &(1.11)\\ \int_{-1}^{+1} dx\, E^q(x,\xi,t) &= F_2^q(t)\,, &(1.12)\\ \int_{-1}^{+1} dx\, \tilde{H}^q(x,\xi,t) &= g_A^q(t)\,, &(1.13)\\ \int_{-1}^{+1} dx\, \tilde{E}^q(x,\xi,t) &= g_P^q(t)\,. &(1.14)\end{aligned}$$

where $F_1^q(t)$ and $F_2^q(t)$ are the elastic Dirac and Pauli form factors and $g_A^q(t)$ and $g_P^q(t)$ are the axial-vector and pseudoscalar form factors for quark flavor q in the nucleon.

Also, Ji's sum rule[4] relates the second moment of some GPDs to the fraction of the nucleon's spin carried by a quark. For quark flavor q, we have

$$\int_{-1}^{1} dx\ x\ \left(H^q(x,\xi) + E^q(x,\xi)\right) = 2J^q\,. \tag{1.15}$$

Eq. (1.15) for J^q is valid for $t = 0$. J^q is the fraction of the nucleon's spin carried by a quark of the flavor q. The sum of J^q over all of quark flavors gives the fraction of the nucleon's spin carried by all quarks, $J^Q = \sum_q J^q$. J^Q can be decomposed as

$$J^Q = \frac{\Delta\Sigma}{2} + L^Q, \tag{1.16}$$

where $\frac{\Delta\Sigma}{2}$ is the quark spin contribution, and L^Q is the contribution from the quark orbital angular momentum. From inclusive and semi-inclusive polarized DIS, $\Delta\Sigma$ can be measured. Therefore, in principle L^Q can be derived using Eq. (1.16). It provides a way to measure the quark orbital angular momentum contribution of the nucleon's spin, which is completely unknown, so far.

Ji's sum rule also works for gluons. The gluon's angular momentum contribution of the nucleon's spin is given,

$$J^G = \int_{-1}^{1} dx\ x\ \left(H^g(x,\xi) + E^g(x,\xi)\right)\,. \tag{1.17}$$

The nucleon's spin is given by the gauge invariant sum,

$$\frac{1}{2} = J^Q + J^G\,. \tag{1.18}$$

This shows that the complete knowledge of the quark angular momentum contribution will reveal the gluon angular momentum contribution.

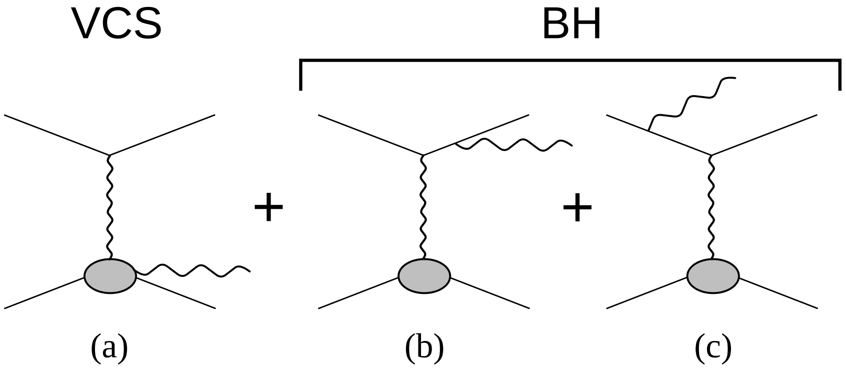

Figure 1.4. Feynman diagrams for DVCS (a) and for the photon radiation from the scattered electron (b) or incoming electron (c) in the Bethe-Heitler process.

1.3 Deeply Virtual Compton Scattering

The GPDs can be accessed by the hard exclusive processes, see Fig. 1.1. The simplest process is DVCS. It turns out that DVCS is the most suitable exclusive process to constrain GPDs from data in the lower energy domain measured with the electroproduction. The reaction $ep \to ep\gamma$ includes not only the DVCS contributions, but also the Bethe-Heitler (BH) process, see Fig. 1.4. They represent different physics, but are indistinguishable. For DVCS, the real photon is radiated by one quark which absorbs the virtual photon, i.e., $\gamma^* p \to \gamma p'$. While in the BH process, the real photon is emitted from incoming or scattered electrons. In the low Q^2 range, the DVCS cross section is much smaller than the BH cross section, and it is difficult to directly measure the DVCS cross section. However we can measure the DVCS contribution through its interference with the BH process.

1.3.1 Cross Section

The four-fold cross section for the process $e(k)p(P_1) \to e(k')p(P_2)\gamma(q_2)$ is given by[18]

$$\frac{d\sigma}{dx_B dy d|\Delta^2| d\phi} = \frac{\alpha^3 x_B y}{16\,\pi^2\,Q^2\sqrt{1+\epsilon^2}} \left|\frac{\mathcal{T}}{e^3}\right|^2 . \qquad (1.19)$$

In Eq. (1.19), the lepton energy fraction is $y = P_1 \cdot q_1 / P_1 \cdot k$, with $q_1 = k - k'$, ϕ is the angle between the scattering plane and the reaction plane, as shown in Fig. 1.5, and $\epsilon \equiv 2x_B \frac{M}{Q}$.

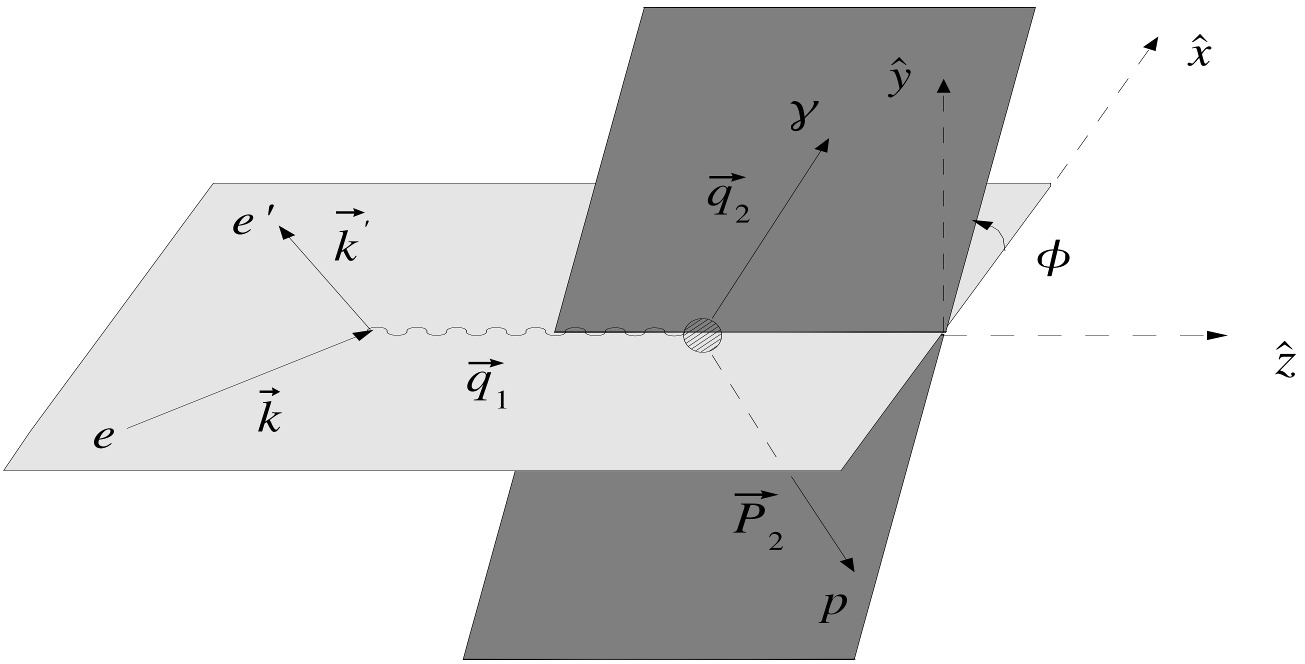

Figure 1.5. Kinematics for the photon electroproduction in the target rest frame. The scattering plane is defined by the direction of incoming electron and of the scattering electron, while the reaction plane is defined by the direction of the outgoing photon and of the recoiled proton. The $\hat{z}$ axis is along the direction of the virtual photon, $\hat{y}$ axis is perpendicular to the scattering plane, and $\hat{x}$ is given by $\hat{x} = \hat{y} \times \hat{z}$. ϕ is the angle between the scattering plane and the reaction plane.

Note that the final state of DVCS is the same as that of BH process, i.e., they are indistinguishable. Therefore, the amplitude ($\mathcal{T}$) of photon production is the sum of the DVCS amplitude ($\mathcal{T}_{DVCS}$) and BH amplitude ($\mathcal{T}_{BH}$), and it reads

$$\mathcal{T}^2 = |\mathcal{T}_{\mathrm{BH}} + \mathcal{T}_{\mathrm{DVCS}}|^2 = |\mathcal{T}_{\mathrm{BH}}|^2 + |\mathcal{T}_{\mathrm{DVCS}}|^2 + \mathcal{I}\,, \tag{1.20}$$

with the interference term

$$\mathcal{I} = \mathcal{T}_{\mathrm{DVCS}}\mathcal{T}^*_{\mathrm{BH}} + \mathcal{T}^*_{\mathrm{DVCS}}\mathcal{T}_{\mathrm{BH}}\,. \tag{1.21}$$

The squared BH amplitude $|\mathcal{T}_{\mathrm{BH}}|^2$, squared DVCS amplitude $|\mathcal{T}_{\mathrm{DVCS}}|^2$, and interference term $\mathcal{I}$ are given by[18]

$$|\mathcal{T}_{\mathrm{BH}}|^2 = \frac{e^6}{x_B^2 y^2 (1+\epsilon^2)^2 \Delta^2\, \mathcal{P}_1(\phi)\mathcal{P}_2(\phi)} \left\{ c_0^{\mathrm{BH}} + \sum_{n=1}^{2} c_n^{\mathrm{BH}} \, \cos{(n\phi)} + s_1^{\mathrm{BH}} \, \sin{(\phi)} \right\}, \tag{1.22}$$

$$|\mathcal{T}_{\mathrm{DVCS}}|^2 = \frac{e^6}{y^2 \mathcal{Q}^2} \left\{ c_0^{\mathrm{DVCS}} + \sum_{n=1}^{2} \left[c_n^{\mathrm{DVCS}} \cos(n\phi) + s_n^{\mathrm{DVCS}} \sin(n\phi) \right] \right\} , \tag{1.23}$$

$$\mathcal{I} = \frac{\pm e^6}{x_B y^3 \Delta^2 \mathcal{P}_1(\phi)\mathcal{P}_2(\phi)} \left\{ c_0^{\mathcal{I}} + \sum_{n=1}^{3} \left[c_n^{\mathcal{I}} \cos(n\phi) + s_n^{\mathcal{I}} \sin(n\phi) \right] \right\} , \tag{1.24}$$

where the + (−) sign in the interference stands for the negatively(positively) charged lepton beam. The $\mathcal{P}_1$ and $\mathcal{P}_2$ are the lepton BH propagators,

$$\mathcal{Q}^2 \mathcal{P}_1 \equiv (k - q_2)^2 = \mathcal{Q}^2 + 2k \cdot \Delta \, , \qquad \mathcal{Q}^2 \mathcal{P}_2 \equiv (k - \Delta)^2 = -2k \cdot \Delta + \Delta^2 \, . \tag{1.25}$$

The coefficients $c_1^{\mathcal{I}}, s_1^{\mathcal{I}}$, c_0^{DVCS}, $c_0^{\mathcal{I}}$, c_1^{DVCS}, s_1^{DVCS}, $c_2^{\mathcal{I}}$,and $s_2^{\mathcal{I}}$ are defined as linear combinations of the Dirac and Pauli form factors F_1 and F_2 with the Compton Form factors (CFFs) $\mathcal{H}, \tilde{\mathcal{H}}, \mathcal{E}, \tilde{\mathcal{E}}$. They are calculated for diverse target polarizations in Ref[18].

For squared BH amplitude,

- Unpolarized target:

$$\begin{aligned} c_{0,\mathrm{unp}}^{\mathrm{BH}} = {} & 8K^2 \left\{ \left(2 + 3\epsilon^2\right) \frac{\mathcal{Q}^2}{\Delta^2} \left(F_1^2 - \frac{\Delta^2}{4M^2} F_2^2 \right) + 2x_B^2 \left(F_1 + F_2\right)^2 \right\} \\ & + (2-y)^2 \Bigg\{ \left(2 + \epsilon^2\right) \left[\frac{4x_B^2 M^2}{\Delta^2} \left(1 + \frac{\Delta^2}{\mathcal{Q}^2}\right)^2 + 4(1 - x_B) \left(1 + x_B \frac{\Delta^2}{\mathcal{Q}^2}\right) \right] \left(F_1^2 - \frac{\Delta^2}{4M^2} F_2^2 \right) \\ & + 4x_B^2 \left[x_B + \left(1 - x_B + \frac{\epsilon^2}{2}\right) \left(1 - \frac{\Delta^2}{Q^2}\right)^2 - x_B(1 - 2x_B) \frac{\Delta^4}{Q^4} \right] \left(F_1 + F_2\right)^2 \Bigg\} \\ & + 8\left(1 + \epsilon^2\right) \left(1 - y - \frac{\epsilon^2 y^2}{4}\right) \Bigg\{ 2\epsilon^2 \left(1 - \frac{\Delta^2}{4M^2}\right) \left(F_1^2 - \frac{\Delta^2}{4M^2} F_2^2 \right) \\ & \qquad\qquad - x_B^2 \left(1 - \frac{\Delta^2}{Q^2}\right)^2 \left(F_1 + F_2\right)^2 \Bigg\} , \end{aligned} \tag{1.26}$$

$$\begin{aligned} c_{1,\mathrm{unp}}^{\mathrm{BH}} = {} & 8K(2-y) \Bigg\{ \left(\frac{4x_B^2 M^2}{\Delta^2} - 2x_B - \epsilon^2 \right) \left(F_1^2 - \frac{\Delta^2}{4M^2} F_2^2 \right) \\ & \qquad\qquad + 2\, x_B^2 \left(1 - (1 - 2x_B) \frac{\Delta^2}{\mathcal{Q}^2} \right) \left(F_1 + F_2\right)^2 \Bigg\}, \end{aligned} \tag{1.27}$$

$$c_{2,\mathrm{unp}}^{\mathrm{BH}} = 8x_B^2 K^2 \left\{ \frac{4M^2}{\Delta^2} \left(F_1^2 - \frac{\Delta^2}{4M^2} F_2^2 \right) + 2\left(F_1 + F_2\right)^2 \right\} . \tag{1.28}$$

- Longitudinally polarized target:

$$
\begin{aligned}
c_{0,\mathrm{LP}}^{\mathrm{BH}} &= 8\lambda\Lambda x_B(2-y)y\frac{\sqrt{1+\epsilon^2}}{1-\frac{\Delta^2}{4M^2}}\left(F_1+F_2\right)\left\{\frac{1}{2}\left[\frac{x_B}{2}\left(1-\frac{\Delta^2}{\mathcal{Q}^2}\right)-\frac{\Delta^2}{4M^2}\right]\left[2-x_B\right.\right. \\
&\left.\left.-\,2(1-x_B)^2\frac{\Delta^2}{\mathcal{Q}^2}+\epsilon^2\left(1-\frac{\Delta^2}{\mathcal{Q}^2}\right)-x_B(1-2x_B)\frac{\Delta^4}{\mathcal{Q}^4}\right]\left(F_1+F_2\right)\right. \\
&\left.+\left(1-(1-x_B)\frac{\Delta^2}{\mathcal{Q}^2}\right)\left[\frac{x_B^2M^2}{\Delta^2}\left(1+\frac{\Delta^2}{\mathcal{Q}^2}\right)^2+(1-x_B)\left(1+x_B\frac{\Delta^2}{\mathcal{Q}^2}\right)\right]\left(F_1+\frac{\Delta^2}{4M^2}F_2\right)\right\},
\end{aligned}
\tag{1.29}
$$

$$
\begin{aligned}
c_{1,\mathrm{LP}}^{\mathrm{BH}} &= -8\lambda\Lambda x_B yK\frac{\sqrt{1+\epsilon^2}}{1-\frac{\Delta^2}{4M^2}}\left(F_1+F_2\right)\left\{\left[\frac{\Delta^2}{2M^2}-x_B\left(1-\frac{\Delta^2}{\mathcal{Q}^2}\right)\right]\left(1-x_B+x_B\frac{\Delta^2}{\mathcal{Q}^2}\right)\left(F_1+F_2\right)\right. \\
&\left.+\left[1+x_B-(3-2x_B)\left(1+x_B\frac{\Delta^2}{\mathcal{Q}^2}\right)-\frac{4x_B^2M^2}{\Delta^2}\left(1+\frac{\Delta^4}{\mathcal{Q}^4}\right)\right]\left(F_1+\frac{\Delta^2}{4M^2}F_2\right)\right\}.
\end{aligned}
\tag{1.30}
$$

For squared DVCS amplitude,

- Unpolarized target:

$$
c_{0,\mathrm{unp}}^{\mathrm{DVCS}} = 2(2-2y+y^2)\mathcal{C}_{\mathrm{unp}}^{\mathrm{DVCS}}\left(\mathcal{F},\mathcal{F}^*\right), \tag{1.31}
$$

$$
\begin{Bmatrix} c_{1,\mathrm{unp}}^{\mathrm{DVCS}} \\ s_{1,\mathrm{unp}}^{\mathrm{DVCS}} \end{Bmatrix} = \frac{8K}{2-x_B}\begin{Bmatrix} 2-y \\ -\lambda y \end{Bmatrix}\begin{Bmatrix} \Re\mathrm{e} \\ \Im\mathrm{m} \end{Bmatrix}\mathcal{C}_{\mathrm{unp}}^{\mathrm{DVCS}}\left(\mathcal{F}^{\mathrm{eff}},\mathcal{F}^*\right). \tag{1.32}
$$

- Longitudinally polarized target:

$$
c_{0,\mathrm{LP}}^{\mathrm{DVCS}} = 2\lambda\Lambda y(2-y)\mathcal{C}_{\mathrm{LP}}^{\mathrm{DVCS}}\left(\mathcal{F},\mathcal{F}^*\right), \tag{1.33}
$$

$$
\begin{Bmatrix} c_{1,\mathrm{LP}}^{\mathrm{DVCS}} \\ s_{1,\mathrm{LP}}^{\mathrm{DVCS}} \end{Bmatrix} = -\frac{8\Lambda K}{2-x_B}\begin{Bmatrix} -\lambda y \\ 2-y \end{Bmatrix}\begin{Bmatrix} \Re\mathrm{e} \\ \Im\mathrm{m} \end{Bmatrix}\mathcal{C}_{\mathrm{LP}}^{\mathrm{DVCS}}\left(\mathcal{F}^{\mathrm{eff}},\mathcal{F}^*\right). \tag{1.34}
$$

For interference of BH and DVCS amplitudes,

- Unpolarized target:

$$c_{0,\mathrm{unp}}^{\mathcal{I}} = -8(2-y)\Re\mathrm{e}\left\{ \frac{(2-y)^2}{1-y} K^2 \mathcal{C}_{\mathrm{unp}}^{\mathcal{I}}(\mathcal{F}) + \frac{\Delta^2}{\mathcal{Q}^2}(1-y)(2-x_B)\left(\mathcal{C}_{\mathrm{unp}}^{\mathcal{I}} + \Delta\mathcal{C}_{\mathrm{unp}}^{\mathcal{I}}\right)(\mathcal{F}) \right\}, \tag{1.35}$$

$$\left\{ \begin{matrix} c_{1,\mathrm{unp}}^{\mathcal{I}} \\ s_{1,\mathrm{unp}}^{\mathcal{I}} \end{matrix} \right\} = 8K \left\{ \begin{matrix} -(2-2y+y^2) \\ \lambda y(2-y) \end{matrix} \right\} \left\{ \begin{matrix} \Re\mathrm{e} \\ \Im\mathrm{m} \end{matrix} \right\} \mathcal{C}_{\mathrm{unp}}^{\mathcal{I}}(\mathcal{F}) , \tag{1.36}$$

$$\left\{ \begin{matrix} c_{2,\mathrm{unp}}^{\mathcal{I}} \\ s_{2,\mathrm{unp}}^{\mathcal{I}} \end{matrix} \right\} = \frac{16K^2}{2-x_B} \left\{ \begin{matrix} -(2-y) \\ \lambda y \end{matrix} \right\} \left\{ \begin{matrix} \Re\mathrm{e} \\ \Im\mathrm{m} \end{matrix} \right\} \mathcal{C}_{\mathrm{unp}}^{\mathcal{I}}\left(\mathcal{F}^{\mathrm{eff}}\right) . \tag{1.37}$$

- Longitudinally polarized target:

$$c_{0,\mathrm{LP}}^{\mathcal{I}} = -8\lambda\Lambda y\Re\mathrm{e}\left\{ \left(\frac{(2-y)^2}{1-y} + 2\right) K^2 \mathcal{C}_{\mathrm{LP}}^{\mathcal{I}}(\mathcal{F}) + \frac{\Delta^2}{\mathcal{Q}^2}(1-y)(2-x_B)\left(\mathcal{C}_{\mathrm{LP}}^{\mathcal{I}} + \Delta\mathcal{C}_{\mathrm{LP}}^{\mathcal{I}}\right)(\mathcal{F}) \right\}, \tag{1.38}$$

$$\left\{ \begin{matrix} c_{1,\mathrm{LP}}^{\mathcal{I}} \\ s_{1,\mathrm{LP}}^{\mathcal{I}} \end{matrix} \right\} = 8\Lambda K \left\{ \begin{matrix} -\lambda y(2-y) \\ 2-2y+y^2 \end{matrix} \right\} \left\{ \begin{matrix} \Re\mathrm{e} \\ \Im\mathrm{m} \end{matrix} \right\} \mathcal{C}_{\mathrm{LP}}^{\mathcal{I}}(\mathcal{F}) , \tag{1.39}$$

$$\left\{ \begin{matrix} c_{2,\mathrm{LP}}^{\mathcal{I}} \\ s_{2,\mathrm{LP}}^{\mathcal{I}} \end{matrix} \right\} = \frac{16\Lambda K^2}{2-x_B} \left\{ \begin{matrix} -\lambda y \\ 2-y \end{matrix} \right\} \left\{ \begin{matrix} \Re\mathrm{e} \\ \Im\mathrm{m} \end{matrix} \right\} \mathcal{C}_{\mathrm{LP}}^{\mathcal{I}}\left(\mathcal{F}^{\mathrm{eff}}\right) . \tag{1.40}$$

In Eq. (1.26) - Eq. (1.39), $\lambda = \pm 1$ is lepton helicity, and $\Lambda = \pm 1$ is the target helicity. $\mathcal{C}^{DVCS}$ and $\mathcal{C}^{I}$ are listed as following,

$$\begin{aligned} \mathcal{C}_{\mathrm{unp}}^{\mathrm{DVCS}}(\mathcal{F},\mathcal{F}^*) = \frac{1}{(2-x_B)^2}\Bigg\{ & 4(1-x_B)\left(\mathcal{H}\mathcal{H}^* + \widetilde{\mathcal{H}}\widetilde{\mathcal{H}}^*\right) - x_B^2\left(\mathcal{H}\mathcal{E}^* + \mathcal{E}\mathcal{H}^* + \widetilde{\mathcal{H}}\widetilde{\mathcal{E}}^* + \widetilde{\mathcal{E}}\widetilde{\mathcal{H}}^*\right) \\ & - \left(x_B^2 + (2-x_B)^2\frac{\Delta^2}{4M^2}\right)\mathcal{E}\mathcal{E}^* - x_B^2\frac{\Delta^2}{4M^2}\widetilde{\mathcal{E}}\widetilde{\mathcal{E}}^* \Bigg\}, \end{aligned} \tag{1.41}$$

$$\begin{aligned} \mathcal{C}_{\mathrm{LP}}^{\mathrm{DVCS}}(\mathcal{F},\mathcal{F}^*) = \frac{1}{(2-x_B)^2}\Bigg\{ & 4(1-x_B)\left(\mathcal{H}\widetilde{\mathcal{H}}^* + \widetilde{\mathcal{H}}\mathcal{H}^*\right) - x_B^2\left(\mathcal{H}\widetilde{\mathcal{E}}^* + \widetilde{\mathcal{E}}\mathcal{H}^* + \widetilde{\mathcal{H}}\mathcal{E}^* + \mathcal{E}\widetilde{\mathcal{H}}^*\right) \\ & -x_B\left(\frac{x_B^2}{2} + (2-x_B)\frac{\Delta^2}{4M^2}\right)\left(\mathcal{E}\widetilde{\mathcal{E}}^* + \widetilde{\mathcal{E}}\mathcal{E}^*\right) \Bigg\}, \end{aligned} \tag{1.42}$$

$$\mathcal{C}_{\mathrm{unp}}^{\mathcal{I}} = F_1\mathcal{H} + \frac{x_B}{2-x_B}(F_1+F_2)\widetilde{\mathcal{H}} - \frac{\Delta^2}{4M^2}F_2\mathcal{E} , \tag{1.43}$$

$$\mathcal{C}_{\mathrm{LP}}^{\mathcal{I}} = \frac{x_B}{2-x_B}(F_1+F_2)\left(\mathcal{H} + \frac{x_B}{2}\mathcal{E}\right) + F_1\widetilde{\mathcal{H}} - \frac{x_B}{2-x_B}\left(\frac{x_B}{2}F_1 + \frac{\Delta^2}{4M^2}F_2\right)\widetilde{\mathcal{E}} . \tag{1.44}$$

The cross section for a polarized target can be written as

$$d\sigma = d\sigma_{\mathrm{unp}} + d\sigma_{\mathrm{LP}}(\Lambda)\,. \tag{1.45}$$

1.3.2 Compton Form Factors

In section 1.3.1, the coefficients of DVCS amplitude are in terms of CFFs $\mathcal{H}, \tilde{\mathcal{H}}, \mathcal{E}, \tilde{\mathcal{E}}$. These complex CFFs are given by flavor sums of convolutions of the corresponding twist-two GPDs with perturbatively calculable coefficient functions $\mathcal{C}^{(\pm)}$ [19, 20, 21] via

$$\begin{aligned}
\{\mathcal{H}, \mathcal{E}\}\,(\xi, t, Q^2) &= \sum_q \int_{-1}^{1} dx\, C_q^{(-)}(\xi, x)\,\{H^q, E^q\}\,(x, \xi, t, Q^2)\,, \qquad (1.46)\\
\left\{\widetilde{\mathcal{H}}, \widetilde{\mathcal{E}}\right\}(\xi, t, Q^2) &= \sum_q \int_{-1}^{1} dx\, C_q^{(+)}(\xi, x)\left\{\widetilde{H}^q, \widetilde{E}^q\right\}(x, \xi, t, Q^2)\,.
\end{aligned}$$

1.3.3 Physical Observables

The most accurate information on GPDs can be deduced from the part of the total cross section, which stems from the interference of the BH process with DVCS amplitude. While, since the cross section of DVCS is small, the alternative method is to measure diverse asymmetries involving charge and spin, respectively.

1.3.3.1 Beam Charge Asymmetry

For facilities with positively and negatively charged lepton beams, one can measure the beam charge asymmetry, which is defined as:

$$A_c(\phi) = \frac{d\sigma^+(\phi) - d\sigma^-(\phi)}{d\sigma^+(\phi) + d\sigma^-(\phi)}, \tag{1.47}$$

where $d\sigma^{+(-)}$ denotes the cross section measurement with positively (negatively) charged lepton beam. From Eq. (1.22) - Eq. (1.24), we can get

$$d\sigma^+ - d\sigma^- \propto \frac{1}{x_B y^3 \mathcal{P}_1(\phi)\mathcal{P}_2(\phi)\Delta^2}\left\{c_0^{\mathcal{I}} + \sum_{n=1}^{3}\left[c_n^{\mathcal{I}}\cos(n\phi) + s_n^{\mathcal{I}}\sin(n\phi)\right]\right\}\,, \tag{1.48}$$

and

$$d\sigma^{+} + d\sigma^{-} \propto \frac{1}{x_B^2 y^2 (1+\epsilon^2)^2 \Delta^2 \, \mathcal{P}_1(\phi)\mathcal{P}_2(\phi)} \left\{ c_0^{\mathrm{BH}} + \sum_{n=1}^{2} c_n^{\mathrm{BH}} \cos{(n\phi)} + s_1^{\mathrm{BH}} \sin{(\phi)} \right\}$$
$$+ \frac{1}{y^2 \mathcal{Q}^2} \left\{ c_0^{\mathrm{DVCS}} + \sum_{n=1}^{2} \left[c_n^{\mathrm{DVCS}} \cos(n\phi) + s_n^{\mathrm{DVCS}} \sin(n\phi) \right] \right\}. \quad (1.49)$$

From Eq. (1.35) - Eq. (1.37), we conclude that the Fourier coefficients s_n^I disappear in Eq. (1.48), assuming the unpolarized beam ($\lambda = 0$). Among the Fourier coefficients c_n^I, both c_0^I and c_1^I are related to the twist-two GPDs, but c_0^I is suppressed by $\mathcal{O}(1/Q)$ compared to c_1^I. The other coefficients c_2^I and c_3^I arise at twist-3 and twist-4 GPDs, respectively, and they are suppressed kinetically comparing to c_1^I. Therefore, in Eq. (1.48), c_1^I is the leading term. In Eq. (1.49), squared BH amplitude dominates and the c_0^{BH} term gives the largest contribution to the squared BH amplitude. Therefore, c_0^{BH} is the leading term in Eq. (1.49). So, the beam charge asymmetry at leading twist can be given by

$$A_C(\phi) \;\; \approx \;\; -\frac{x_B}{y} \frac{c_1^I}{c_0^{BH}} cos(\phi). \quad (1.50)$$

Consequently, the azimuthal angular dependence of the beam charge asymmetry should be a dominant $cos\phi$ function, accompanied by a small offset and by small $cos2\phi$ and $cos3\phi$ modulations.

1.3.3.2 Beam Spin Asymmetry

The azimuthal angular dependence of the beam-spin asymmetry is defined by

$$A_{\mathrm{LU}}(\phi) = \frac{d\sigma^{\uparrow}(\phi) - d\sigma^{\downarrow}(\phi)}{d\sigma^{\uparrow}(\phi) + d\sigma^{\downarrow}(\phi)}, \quad (1.51)$$

where A_{LU} represents the asymmetry (A) measured using a longitudinally (L) polarized beam and an unpolarized (U) target. Here $d\sigma^{\uparrow(\downarrow)}$ is the cross section measurement using the beam which helicity is parallel (anti-parallel) to the beam direction. The Fourier coefficients in Eq. (1.22) - Eq. (1.24) depend or don't depend on λ. Only the coefficients (s_1^I, s_2^I, s_1^{DVCS}) which depend on λ are left in the numerator and the other which don't depend on λ are left in the denominator. Due the same reason which is given for the beam charge asymmetry, the leading term in the denominator is c_0^{BH}. s_1^I arises at twist-two level, while s_2^I and s_1^{DVCS}

arise at twist-three level, and are suppressed by Δ/Q. Therefore, the leading term in the numerator is s_1^I. So, the azimuthal dependence of the beam spin asymmetry is approximately given by the $\sin(\phi)$ function:

$$A_{\mathrm{LU}}(\phi) \sim \pm \frac{x_B}{y} \frac{s^{\mathcal{I}}_{1,\mathrm{unp}}}{c^{\mathrm{BH}}_{0,\mathrm{unp}}} \sin(\phi). \tag{1.52}$$

Combining Eq. (1.36) and Eq. (1.43), we can get a further equation:

$$A_{\mathrm{LU}}(\phi) \propto \Im\mathrm{m} \left\{ F_1 \mathcal{H} + \frac{x_B}{2 - x_B}(F_1 + F_2)\widetilde{\mathcal{H}} - \frac{\Delta^2}{4M^2} F_2 \mathcal{E} \right\} \sin(\phi)\,. \tag{1.53}$$

Hence, $A_{\mathrm{LU}}(\phi)$ is linear in form factors and CFFs. In the kinematics of small Δ and small x_B, A_{LU} is sensitive to $\Im\mathrm{m}\mathcal{H}$. In leading order, $\Im\mathrm{m}\mathcal{H}$ is directly given by the GPDs on the diagonal $x = \pm\xi$[18]. The first measurements of A_{LU} were reported by HERMES[7] and CLAS[6], which will be described in section 1.3.4.3.

1.3.4 Previous Measurements

1.3.4.1 Measurements of Cross Sections

The first DVCS cross section measurements at high energy have been reported by H1[22, 23] and ZEUS[24] collaborations using HERA collider at DESY. The cross section was measured as a function of Q^2, W, and $-t$, respectively. The Q^2-dependence for W=82 GeV/c^2 and $|t| < 1\,\mathrm{GeV}^2/\mathrm{c}^2$ is illustrated in Figure 1.6, as well as W-dependence for $Q^2 = 8\,\mathrm{GeV}^2/\mathrm{c}^2$ and $|t| < 1\,\mathrm{GeV}^2/\mathrm{c}^2$. The t-dependence of the differential $\gamma^* p \rightarrow \gamma p$ cross section is illustrated in Fig 1.7. The data shown are from H1 and ZEUS.

1.3.4.2 Measurements of the Beam Charge Asymmetry

The beam charge asymmetry was measured by HERMES collaboration [25, 26]using HERA. HERA is the only GeV-range accelerator which provides both electron and positron beams. So far, there are no published data for the beam spin asymmetry. The preliminary results of the beam spin asymmetry from HERMES are shown in Fig 1.8.

1.3.4.3 Measurements of the Beam Spin Asymmetry

The first published results of the beam spin asymmetry (A_{LU}) were measured by CLAS [6] and HERMES [7] collaborations. At CLAS, a 4.25 GeV electron beam scattered off

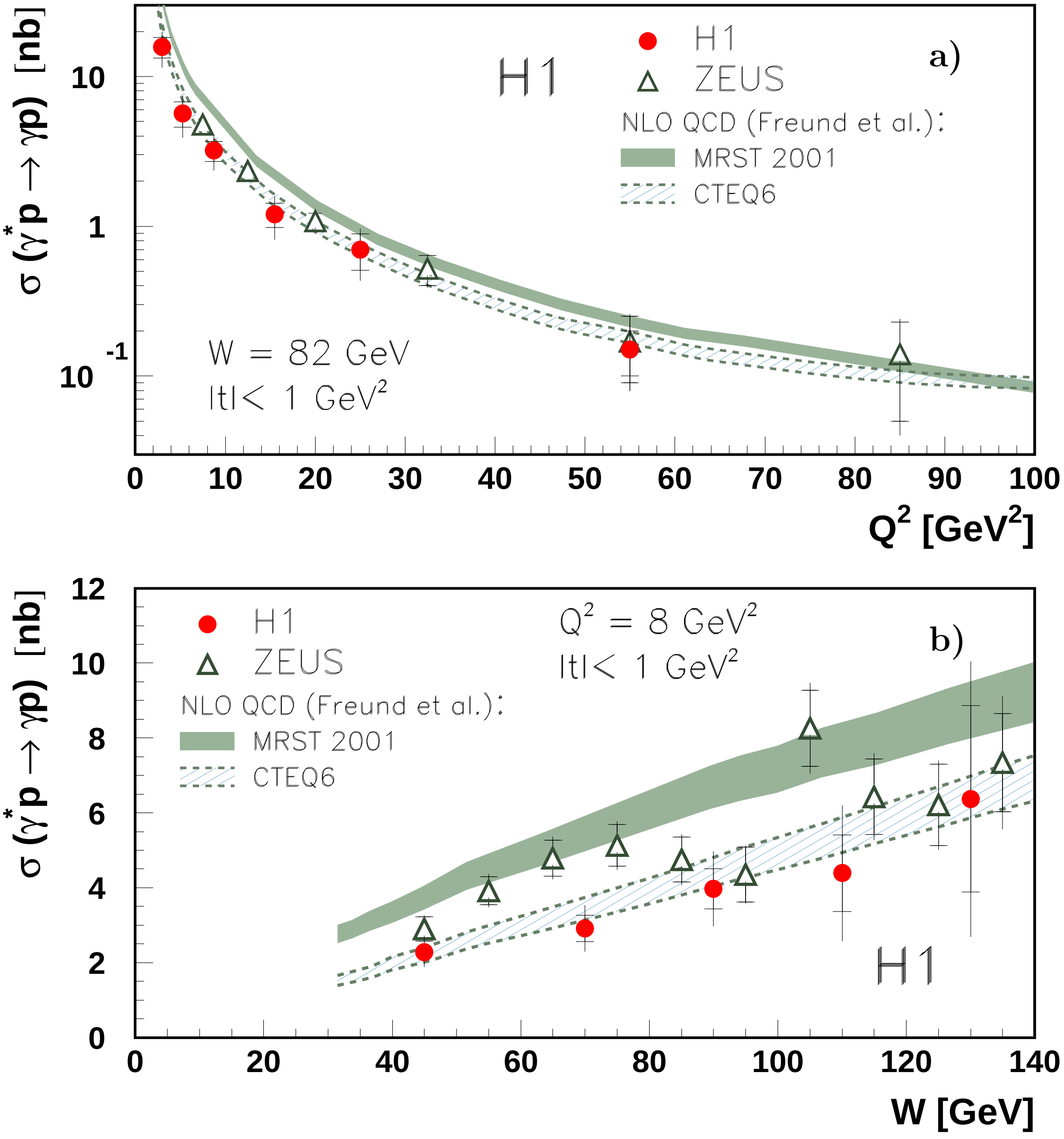

Figure 1.6. The differential $\gamma^* p \rightarrow \gamma p$ cross section a) as a function of Q^2, b) as a function of W, which was measured by H1 and ZEUS in comparison with GPD-based pQCD predictions. The inner error bars denote the statistical and the full error bars the quadratic sum of the statistical and systematic uncertainties. The figure is taken from Ref[23].

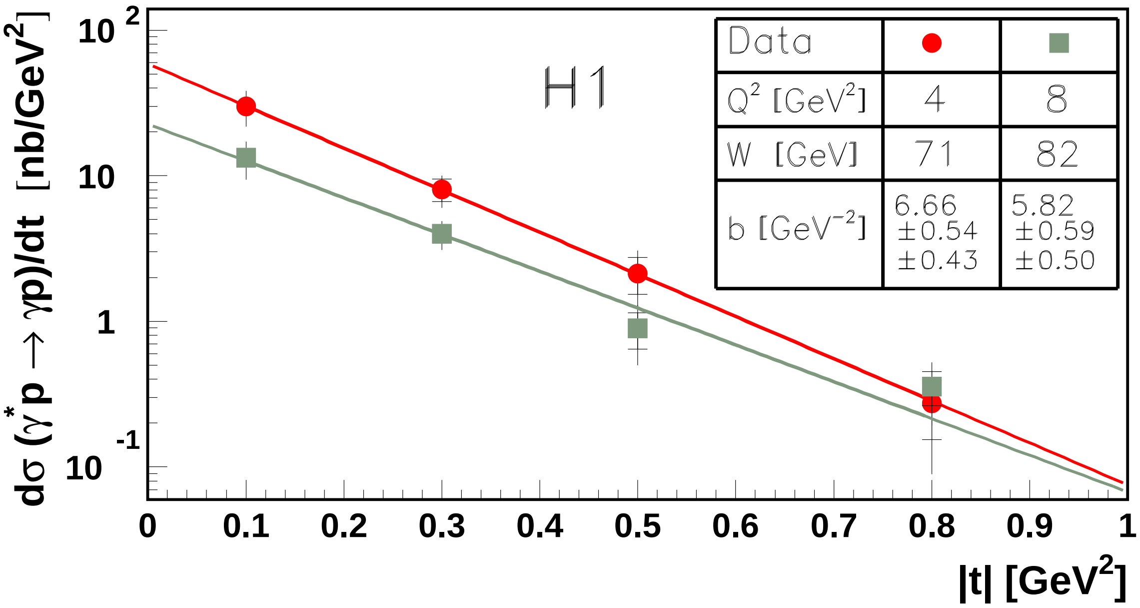

Figure 1.7. The t-dependence of the differential $\gamma^* p \to \gamma p$ cross section measured by H1. The inner error bars denote the statistical and the full error bars the quadratic sum of the statistical and systematic uncertainties. The points are fitted as a function $e^{-b|t|}$. The figure is taken from Ref[23].

the fixed proton target, and the kinematic coverage is: $1\,\mathrm{GeV}^2/\mathrm{c}^2 < Q^2 < 1.75\,\mathrm{GeV}^2/\mathrm{c}^2$, $0.13 < x_B < 0.35$, $0.1\,\mathrm{GeV}^2/\mathrm{c}^2 < -\Delta^2 < 0.3\,\mathrm{GeV}^2/\mathrm{c}^2$, and $W > 2$ GeV/c^2. At HERMES, a 27.6 GeV positron beam scattered off the fixed proton target, and the average values of kinematic variables are $\langle Q^2 \rangle = 2.6\,\mathrm{GeV}^2/\mathrm{c}^2$, $\langle x_B \rangle = 0.11$ and $\langle -\Delta^2 \rangle = 0.27\,\mathrm{GeV}^2/\mathrm{c}^2$. The azimuthal dependence of A_{LU} is shown in Fig. 1.9.

Since at CLAS the Electromagnetic Calorimeter (EC) acceptance coverage is from 8^o to 45^o, most of photons from DVCS can not be detected. Therefore, events containing exactly one proton and one electron were selected. At large missing energy, the missing mass squared of (ep) for $\vec{e}p \to ep'X$ can not separate single photons and π^0s event by event. To determine the number of single photon events, the line shape of the missing mass squared distributions was analyzed. For each ϕ bin and each beam helicity state, the missing mass squared distributions were fitted with a function, which is the sum of two Gaussians and a third order polynomial.

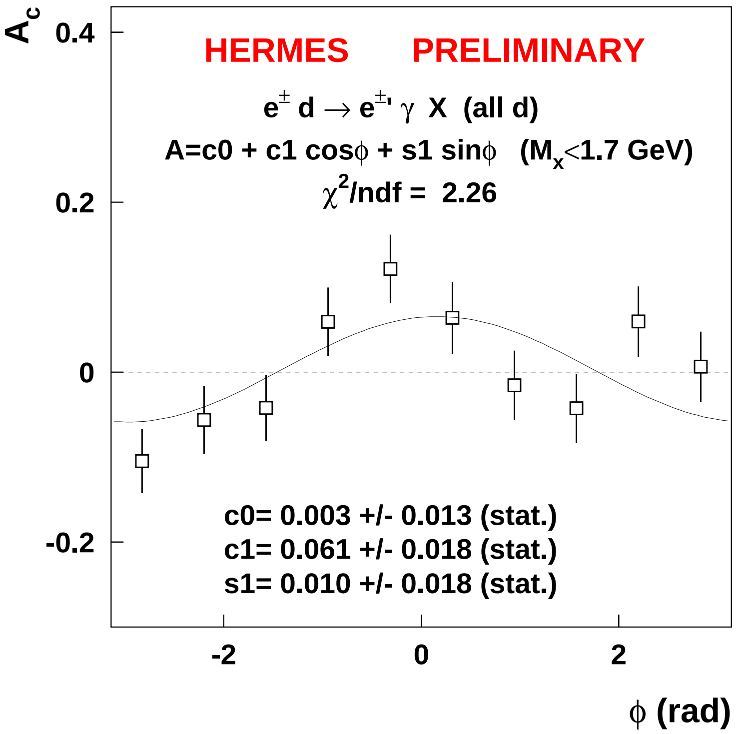

Figure 1.8. The azimuthal angle ϕ dependence of the beam charge asymmetry A_C on deuteron for the hard electroproduction of photons. The error bars are only statistical uncertainties.

At HERMES, the recoiled proton can not be detected, therefore, $\vec{e^+}p \rightarrow e^+\gamma X$ events were used. The missing mass of $e^+\gamma X$ was used to identify the single photon events.

Since both HERMES and CLAS missed one particle of the final state (HERMES did not measure the proton, and CLAS did not measure the photon), it is not very convincing to show the single photon identification. To detect all of three particles of photon electroproduction, a photon detector was added in CLAS to detect photons with polar angle from 3^o to 8^o[27]. From March 2005 through May 2005, the new data were taken with an additional photon detector using CLAS to measure the beam spin asymmetry. This program studies not only the azimuthal dependence, but also the Q^2-, x_B-, and t-dependence of the beam spin asymmetry.

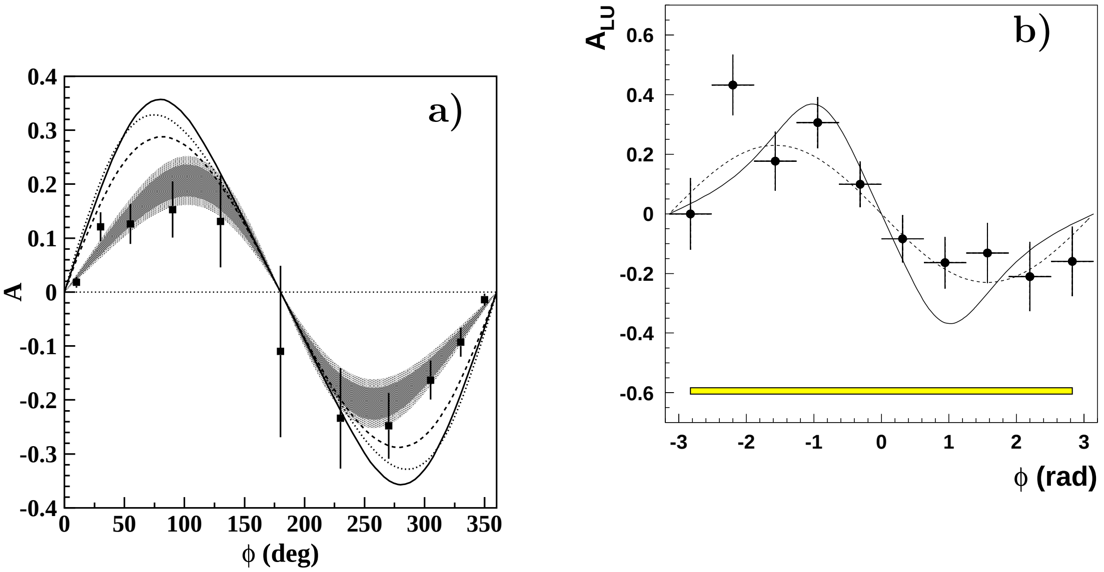

Figure 1.9. The azimuthal dependence of the beam spin asymmetry for the hard electroproduction of photons measured by CLAS[6] (a) and HERMES[7](b). Left panel: the dark shaded region corresponds to the fitted function $A(\phi) = \alpha sin\phi + \beta sin2\phi$ with the statistical errors. The light shaded region corresponds to the fitted function $A(\phi)$ with the quadratic sum of the statistical and systematic uncertainties. The curves are model predictions. Right panel: the error bars correspond to the statistical errors, and the band below correspond to the systematic errors. The dashed curve is $sin\phi$ modulation with an amplitude of 0.23, and the solid curve is a model calculation.

1.4 Target Spin Asymmetry

This work will focus on the target spin asymmetry which is given by

$$A_{\mathrm{UL}}(\phi) = \frac{d\sigma^{\Uparrow}(\phi) - d\sigma^{\Downarrow}(\phi)}{d\sigma^{\Uparrow}(\phi) + d\sigma^{\Downarrow}(\phi)}\,, \tag{1.54}$$

where A_{UL} denotes the asymmetry measured using an unpolarized (U) beam and a longitudinally (L) polarized target. The $\Uparrow$ ($\Downarrow$) represents $\Lambda = +(-)1$ longitudinal polarization. Completely analogous to the beam spin asymmetry, the squared BH amplitude dominates the denominator and c_0^{BH} gives the largest contribution to the squared BH amplitude. In the numerator, the Fourier coefficients (s_1^I, s_2^I, s_2^{DVCS}) which depend on Λ are left. Both s_2^I and s_2^{DVCS} from twist-three level are kinetically suppressed compared to s_1^I. So, we get the approximation,

$$
\begin{aligned}
& A_{\mathrm{UL}}(\phi) \sim \Lambda \frac{x_B}{y} \frac{s^{\mathcal{I}}_{1,\mathrm{LP}}}{c^{\mathrm{BH}}_{0,\mathrm{unp}}} \sin(\phi) \\
& \propto \Im\mathrm{m}\{F_1 \widetilde{\mathcal{H}} + \frac{x_B}{2-x_B}(F_1+F_2)(\mathcal{H} - \frac{x}{2}\mathcal{E}) \\
& - \frac{x_B}{2-x_B}(\frac{x_B}{2}F_1 + \frac{\Delta^2}{4M^2}F_2)\widetilde{\mathcal{E}}\} \sin(\phi)
\end{aligned}
\tag{1.55}
$$

Therefore, the measurement of the target spin asymmetry should reveal a dominant $sin\phi$ dependence, and probably accompanied by a $sin2\phi$ modulation. At the CLAS kinematics, i.e., small Δ and small x_B, A_{UL} is sensitive to the imaginary parts of $\widetilde{\mathcal{H}}$ and $\mathcal{H}$. As we know, the beam spin asymmetry is sensitive to the imaginary part of $\mathcal{H}$. Therefore, combining the measurement of the beam spin asymmetry, the target spin asymmetry allows us to access the imaginary part of $\widetilde{\mathcal{H}}$, which is directly given by the GPDs $\widetilde{\mathcal{H}}$.

This measurement is based on the EG1b data taken using CLAS from Sep. 2000 to Apr. 2001 with the longitudinally polarized electron beam and longitudinally polarized proton target. The main purpose of EG1b experiment is to measure the spin structures of the proton and the neutron, therefore, the beam energy ranges from 1.6 GeV to 5.7 GeV, and two targets, ND_3 and NH_3, are used. As a byproduct, this measurement is based on only part of EG1b data with 5.7 GeV beam energy and NH_3 target. From these data, the DVCS events will be identified and counted for each ϕ bin in each target helicity. Then, the target spin asymmetry will be calculated using

$$
A_{\mathrm{UL}}(\phi) = \frac{\bar{N}^{\Uparrow}(\phi) - \bar{N}^{\Downarrow}(\phi)}{\bar{N}^{\Uparrow}(\phi) + \bar{N}^{\Downarrow}(\phi)}\,, \tag{1.56}
$$

where $\bar{N}$ represents the normalized number of DVCS events.

1.5 Organization

In this thesis, the experiment and the asymmetry measurement are described in detail. In Chapter 2, each detector of CLAS is described, in addition, the polarized target is introduced, including the target materials, and the mechanical system. Chapter 3 introduces the event reconstruction, including how the electron, the proton, and the photon are reconstructed in the reconstruction program. To minimize contamination, more strict identifications for both electrons and protons are developed, especially under the kinematic coverage of the

DVCS process. In addition, details are given for the electron momentum correction and the proton energy loss corrections. Finally, the fiducial cuts are explained for each particle. Chapter 4 listed the data used in this work, and the target polarization measurement is also described. The DVCS events are identified in Chapter 5, but they are contaminated by π^0 events, therefore, the π^0 asymmetry is studied in Chapter 6, and Monte Carlo simulation is performed to estimate the π^0 background in Chapter 7. Results and conclusions are presented in Chapter 8. Finally, the Appendixes list the number of DVCS events as a function of ϕ for each data set, as well as the number of π^0 events, the target spin asymmetry for each data set, and the fraction of π^0 contamination as a function of ϕ.

CHAPTER 2

EXPERIMENTAL SETUP

2.1 Overview

The experiment took place at the Continuous Electron Beam Facility (CEBAF) at the Thomas Jefferson National Accelerator Facility (JLAB) in Newport News, Virginia. JLAB is a U.S. Department of Energy facility. There are three experimental halls, A, B and C at JLAB, and each is designed to investigate the hadronic structure of matter using electron or photon beams. The experimental data presented in this thesis were taken using the CEBAF Large Angle Spectrometer (CLAS), which is housed in Hall-B. CEBAF provide a longitudinally polarized electron beam, and for the data run, a longitudinally polarized target was installed in CLAS. The accelerator, the polarized target, and the CLAS detector will be described in detail in this chapter.

2.2 The Accelerator

The schematic layout of JLAB and experimental halls is shown in Fig. 2.1. The accelerator is composed of two anti-parallel linear accelerators, known as linacs, five sets of recirculation arcs, and a 45-MeV injector. The linac is equipped with 20 cryomodules, and each cryomodule is made of 20 superconducting radio-frequency (RF) cavities. The superconductivity is acquired by holding the RF cavities in 2 K helium bath. The two linacs are connected by two sets of 180^o recirculation arcs so that the beam can be continually accelerated. Several quadrupole and dipole magnets are used to steer and focus the beam as it passes through the accelerator. The electron beam is continuously generated with 45 MeV at the injector and accelerated through the two linacs. After the beam reaches the desired energy, it is delivered to one or more of the experimental Halls. In Hall-B, some runs

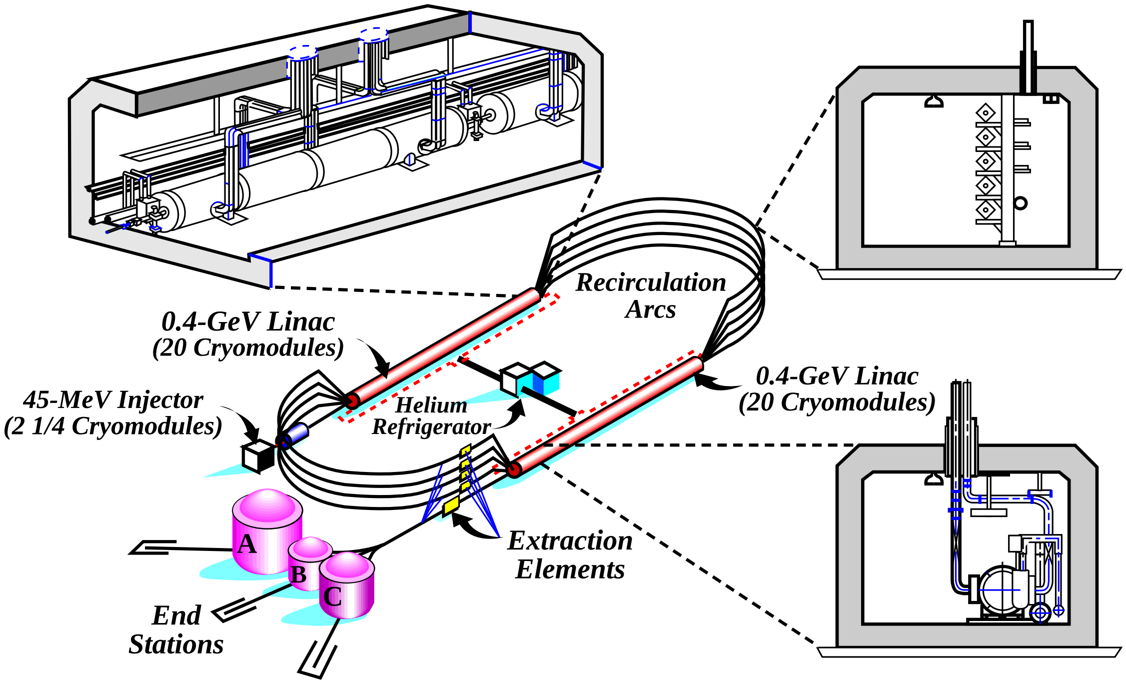

Figure 2.1. Continuous electron beam accelerating facility at Thomas Jefferson National Accelerator Laboratory

are operated using a photon beam. The photon beam is produced by directing the electron beam to a thin target, i.e., the radiator. The produced photons from the radiator continue forward, whereas the electrons are bended away the beam line by the tagging spectrometer. Fig. 2.2 shows the position of photon-tagging system (the radiator and tagging spectrometer). Ref[28] gives more details about photon-tagging system. By controlling th polarization of the electron beam, non-polarized, or circularly polarized, or linearly polarized photon beams can be acquired according to experiment requirements. Although photon beams are available, the experiment for this analysis only used the electron beam.

2.3 The CEBAF Large Acceptance Spectrometer

The CEBAF Large Acceptance Spectrometer, as depicted in Fig. 2.2, Fig. 2.3, and Fig. 2.4, is azimuthally divided into six independent sectors within a large superconducting toroidal magnet. Each sector is equipped with three regions of drift chambers (DC)

[29, 30, 31] for track reconstruction and momentum spectrometry of charged particles between 8^o and 142^o in polar angular range and within up to 80% azimuthal coverage. Particle identification utilizes a set of scintillator counters (SC)[32] to determine the time of flight (TOF) for charged particles. A forward angle electromagnetic calorimeter (EC)[33, 34] is used to identify and measure electromagnetic showering particles (electrons and photons) and neutrons. Threshold gas Cerenkov counters (CC)[35] are used in conjunction with the EC for electron identification and triggering. Each detector subsystem of the CLAS will be described in details in the following sections.

2.3.1 Torus Magnet

The torus magnet is composed of six individual superconducting coils around the electron beam line. It provides a magnetic field in the ϕ direction. Therefore, as the charged particles transverse through the CLAS, their trajectories in the ϕ direction remain unchanged whereas the trajectories are bent either toward or away from the beam line depending on the charge of the particle and the polarization of the torus. The magnetic field thus allows one to analyze the momentum of the charged particles.

The maximum designed current in the torus coils is 3860 A, corresponding the integral magnetic field 2.5 T m in the forward direction, and 0.6 T m at a polar angle of 90^o. During the run (EG1b), the torus was operated with 4 different values: 1500, -1500, 2250, -2250 A, with respective to 38.9% and 58.3% of maximum magnetic field, respectively. When the current is positive, the magnetic field resulting from the torus bends the electron toward beam line, therefore, the data taken with positive torus current are called inbending data. Whereas, the data taken with negative torus current are called outbending data.

2.3.2 Drift Chambers

The drift chambers in each sector are divided into three regions: region 1 (R1), region 2 (R2), and region 3 (R3), see Fig. 2.3 and Fig. 2.4. R1 chambers are located close to the target and in an area of low magnetic field. R2 chambers are larger and reside between the torus coils in an area of high magnetic field. R3 chambers are the largest, radially located outside

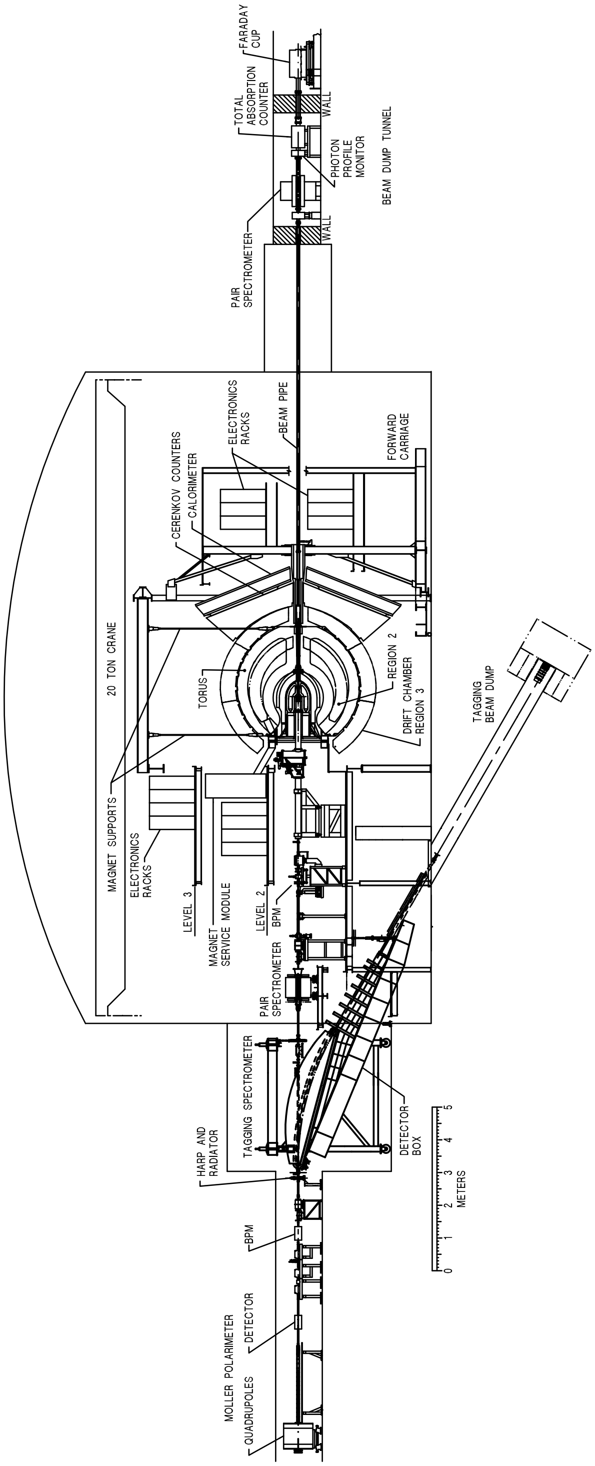

Figure 2.2. Side view schematic of the CLAS detector in Hall B

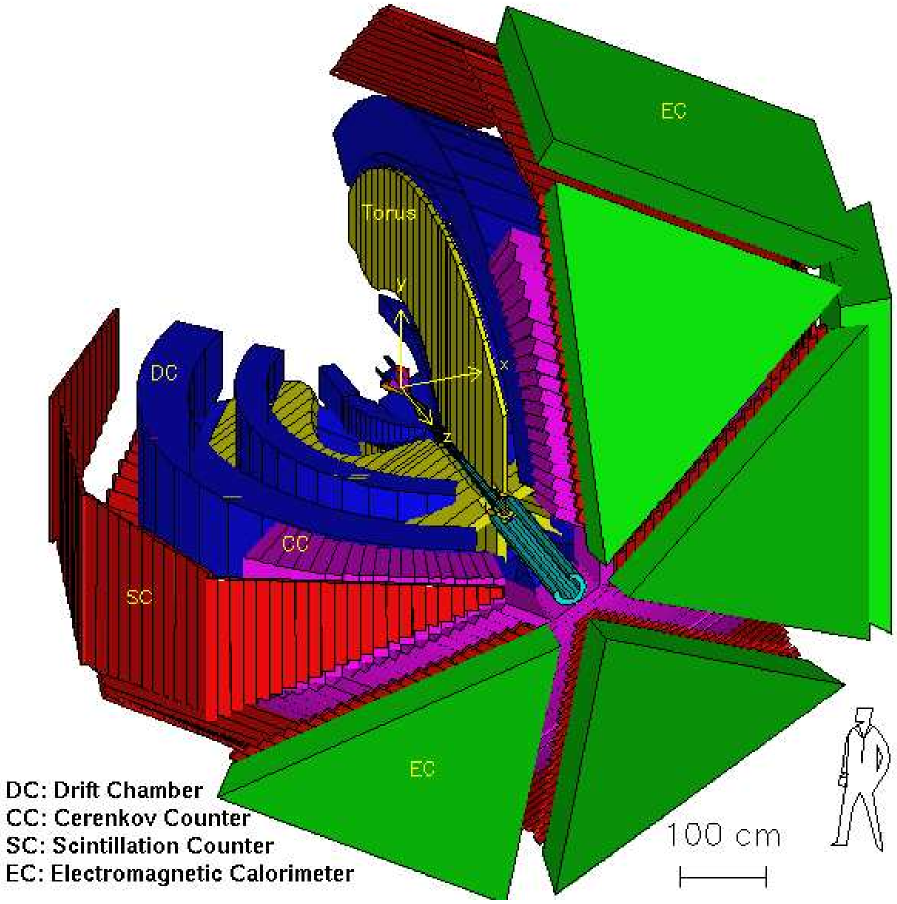

Figure 2.3. A three dimensional view of the CLAS detector. Some detector components are pulled out to show the details. The figure at the right bottom of the figure shows the scale. The beam enters from the back side and the non-interacting beam emerges out the front through a beam pipe.

of the torus magnet. Both Fig. 2.3 and Fig. 2.4 show the relative position of three regions of chambers. All drift chamber regions used together form the momentum spectrometer.

Each drift chamber region is subdivided into two separate superlayers. Each superlayer consists of six layers of drift cells, except for superlayer one in region one which has only 4 layers of drift cells. The drift cell has one sense (anode) wire at a positive potential surrounded by six normal wires (cathode) in an hexagonal shape at negative potential (see Fig. 2.5). There are totally 35,148 individually wired drift cells. The CLAS is filled with the gas of a 90% Ar -10% CO_2 mixture. Therefore, as the charged particle passes through

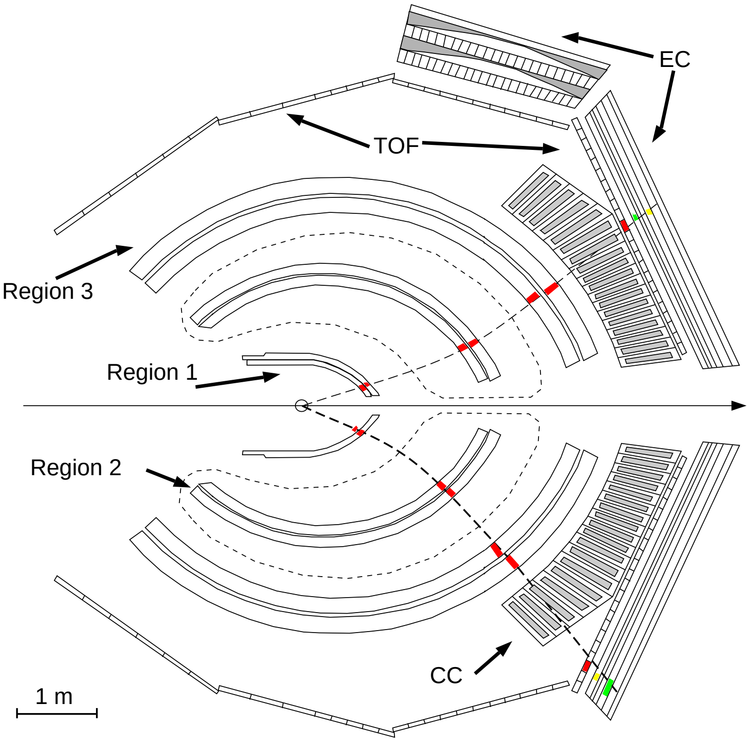

Figure 2.4. A schematic view of the CLAS detector, showing a cut along the beam line. The detector components are labeled, and the trajectories of two charged particles are shown on the figure. The beam enters from the left.

the gas in the DC, it ionizes the atom and produces the ion pairs. The negative ions drift to the sense wire and create a voltage pulse on the sense wire. The pulse is presented to the time-to-digital converters (TDC) for digitization. The online data acquisition system measures and stores these raw TDC times.

2.3.3 Cerenkov Counters

Beyond the drift chambers are threshold Cerenkov counters, which are used to trigger electrons and identify electrons from pions. These detectors cover the polar scattering angle from 8^o to 45^o. The location of the Cerenkov counters in CLAS is shown in Fig. 2.3 and Fig. 2.4.

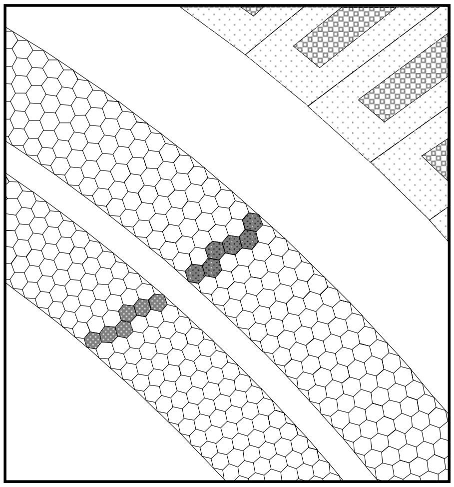

Figure 2.5. Region 3 showing the two superlayers each consisting of six layers of drift cells. The highlighted cells show a track passing through the DC. The upper right corner is the edge of a Cerenkov counters. The drift cell has one sense (anode) wire at a positive potential surrounded by six normal wires (cathode) in an hexagonal shape at negative potential. There are totally 35,148 individually wired drift cells.

When charged particles pass through a medium with speed exceeding the speed of light in that medium, they emit radiation known as Cerenkov light. The threshold at which Cerenkov radiation occurs is given by $v \geq \frac{c}{n}$, where c is the speed of the light in vacuum, n is the refraction index of the medium, and v is the speed of the charged particle. The gas mixture in the Cerenkov detector is C_4F_{10} (perflourobutane). Its refraction index is 1.00153. The threshold for the energy is written as $E > \gamma m$, with $\gamma = \frac{1}{\sqrt{1-\frac{1}{n^2}}} = 18.098$. Therefore, the threshold for electron energy is 9 MeV, while it is 2.5 GeV for pions. Since the pions don't emit Cerenkov light with energy below 2.5 GeV, this can separate electrons from pions up to a pion energy 2.5 GeV.

The Cerenkov light is collected by a system of mirrors, light-collection optics and photomultiplier tubes (PMTs), see Fig. 2.6. The PMTs lie in the shadows of the magnet coils. Since the azimuthal angle of the charged particle remains unchanged when going through the CLAS, the placement of the PMTs doesn't change the angular coverage. To preserve the electron polar angle information, the light-collection optics are designed to focus the light from Cerenkov radiation only in the ϕ direction. This focusing is achieved by hyperbolic and elliptical mirrors. The θ range of each sector is divided into 18 regions, as seen in Fig. 2.4, and each θ segment is subsequently divided into two modules about the symmetry plane, as seen in Fig. 2.6. This division results in a total of 12 identical sub-sectors around the ϕ direction for each θ segment, and a total of 216 light-collection modules.

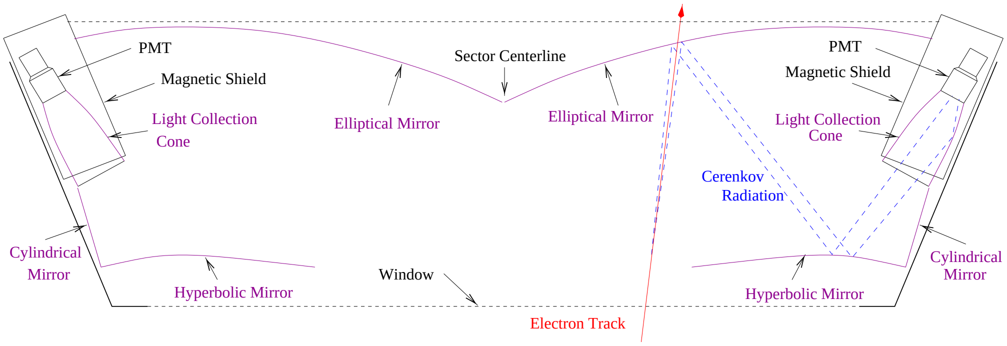

Figure 2.6. A schematic view of one Cerenkov segment. Also shown is how the Cerenkov light is collected by the light collection cone. PMT lies in the shadow of the magnet coils.

2.3.4 Time of Flight Counters

To determine the mass of a charged particle, TOF counters are used to provide high resolution timing measurements. The TOF counters cover a polar angle from 8^o to 142^o and nearly the entire azimuthal angle. Their relative positioning with respect to other detector subsystems is seen in Fig. 2.3 and Fig. 2.4. The TOF counters of one sector consist of 48 scintillator strips, as seen in Fig. 2.7. Each scintillator strip is uniformly 5.08 cm thick, and is positioned perpendicular to the beam direction. The width of a strip varies from 15 cm for the forward angles and 22 cm for the large angles, and the length is between 30 cm to 450 cm. Therefore, TOF counters cover a total surface area of 206 m^2. At each end of the scintillator strip, there are PMTs to read out the signal.

2.3.5 Electromagnetic Calorimeters

As we discussed in section 2.3.3, Cerenkov counters can separate the electrons from pions up to a pion energy 2.5 GeV. At 2.5 GeV, pions start emitting Cerenkov light, and therefore,

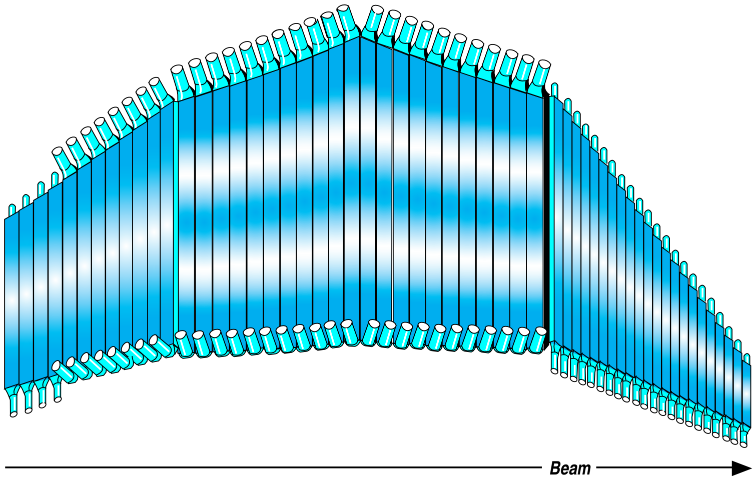

Figure 2.7. TOF counters in one sector, also shown are the scintillator strips with a PMT at each end. The width of a strip varies from 15 cm to 22 cm, and the length is between 30 cm to 450 cm.

pion electron separation fails by this method. Fortunately, at these higher energies, the electromagnetic calorimeters can be used to discriminate electrons and high energy pions. The EC can detect and trigger electrons at energies above 0.5 GeV and photons at energies above 0.2 GeV. In addition it can also detect neutrons and be used to reconstruct π^0 and η from the measurement of their two decay photons.

Like the Cerenkov counters, the EC covers 80% of azimuthal angle and a polar angle from 8^o to 45^o. Each sector contains one calorimeter unit which is made of 39 alternating layers of 10 mm thick scintillator strips and 2.2 mm lead sheets with a total thickness of 16 radiation lengths. A ratio 0.24 of lead to scintillator thickness is used, requiring 39 cm of scintillator and 8.4 cm of lead. With this ratio, around 30% of the energy in a shower is deposited in the scintillator.

In order to fit the hexagonal geometry of the CLAS forward sectors, each lead or scintillator layer is shaped like an equilateral triangle. For the purposes of readout, each scintillator layer is divided into 36 strips parallel to one edge of the triangle. Each three successive scintillator layers are rotated 120^o with the orientation of the strip, and labeled as U, V and W, as shown in Fig. 2.8. Therefore, each EC module consist of 13 U-planes, 13 V-planes, and 13 W-planes. These three orientations or views help to determine the location of the shower. To provide longitudinal sampling of the shower for improved electron and hadron separations, each EC module is subdivided into an inner (15 layers) and outer (24 layers) stack. For each stack, the strips in the same position from the same view are connected to one PMT through a fiber optic cables. Thus there are 36(strips)× 3(views)×2(stacks)=216 PMTs in each module.

The EC operates on the principle that the particle deposits energy in detector material. When the particle hits the EC, it deposits the energy in the scintillator material and produces the light which is collected by PMTs. There are two modes of depositing energy in the scintillator, ionization and radiation. Electrons release all of the energy through radiation and produce the showers of e^+e^- pairs, while heavier hadrons, such as pions, lose energy through minimum ionization. For minimum ionizing particles, such as pions, the energy released both in the inner stack and outer stack of the EC is only related with the thickness of the inner and outer stacks, and independent on the pion energy. This makes it possible to separator electrons from pions which can not be discriminated by the CC.

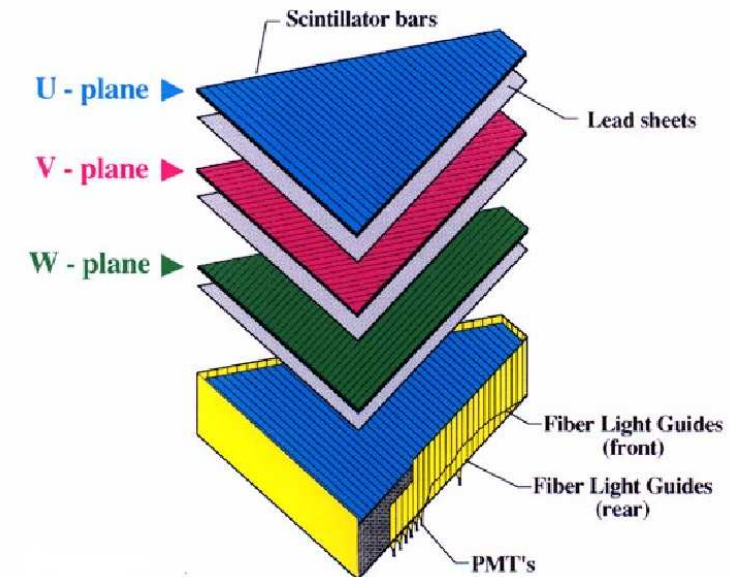

Figure 2.8. Exploded view of one of the six CLAS electromagnetic calorimeter modules.

2.3.6 Data Acquisition System and Trigger

There are two levels of trigger system in the CLAS, the Level-1 and Level-2 trigger. The Level-1 trigger is dead-timeless, processing all prompt PMT signals. The trigger signal for Level-1 trigger is the coincidence signal from the CC and EC (the TOF signal can be included). To reject backgrounds such as cosmic-rays which can set the Level-1 trigger, the Level-2 trigger is used to find the "likely tracks" in the drift chamber system. If no correlated tracks are found by the Level-2 trigger, the trigger supervisor send a fast-clear to the front-end electronics, and reset them.

During EG1b runs, only the Level-1 trigger was used. The trigger thresholds for EG1b experiment are summarized in Table 2.1. The Level-1 trigger required the matching CC and EC signals in coincidence. The thresholds were selected appropriately for each beam and torus setting. The trigger thresholds can be found at [36]. The more information on the CLAS trigger system is given in Ref.[37].

Table 2.1. EG1b Trigger Thresholds.

System	Threshold(in mV)	Threshold(in GeV)
Electromagnetic Calorimeter	150	0.6
Cerenkov Counters	20	< 1 photo-electron

If there is a trigger, the data signals from all the detector parts are digitized in 24 FASTBUS and VME crates and collected by the 24 VME Readout Controllers (ROC1 to ROC24) in these crates. The arrays of digitized values are translated into tables, buffered and then transfered through fast Ethernet lines to the online data acquisition computer (CLON10). CLON10 performs three primary processes, the event builder, event transport, and event recorder, see Fig. 2.9. The event builder puts together the data from various detector components and builds complete events. The completed event is prefixed by headers, which contains a run and event number, event type, and the trigger bits. The event builder transfers the completed events to shared memory on CLON10. Some events are sent to remote event transport, such as ET2 and ET3, for online monitoring. The event recorder read out all events from ET1 for permanent storage. The data are written in a single stream to RAID (Redundant Array of Inexpensive Disk) disks, then transferred to the remote tape SILO for permanent storage.

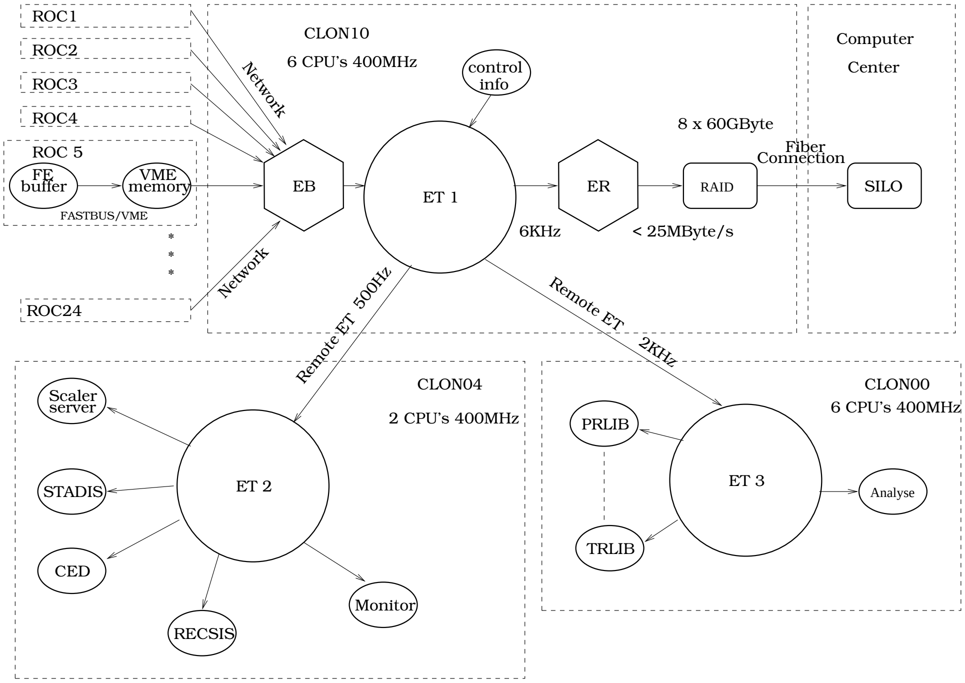

Figure 2.9. A schematic view of the CLAS data flow. Also shown ET1 shared memory in CLON10 computer, and remote shared memory (ET2, ET3) for online monitoring. The data are written in tape SILO for permanent storage.

2.4 Polarized Target

In EG1b experiment, the targets were longitudinally polarized ^{15}NH$_3$ and ^{15}ND$_3$. In addition to the polarized targets, ^{4}He, ^{12}C and frozen ^{15}N targets were also used to study the dilution due to the unpolarized material in the target. An ^{15}NH$_3$ or ^{15}ND$_3$ target was placed in 1 K liquid helium bath, and polarized using Dynamic Nuclear Polarization (DNP) technique. The polarization of the target was monitored using a Nuclear Magnetic Resonance (NMR) system. In this section, more details on the target system, target materials and DNP theory, are discussed.

2.4.1 The Target System

Typically targets are located in the center of CLAS. To minimize the effect of the CLAS toroid magnetic field, the polarized target system was not located in the center of the CLAS, but positioned 55 cm upstream of the center of the CLAS. This shift off of center also makes the acceptance larger due to the coverage of the coverage of the target magnet. The target system is shown in Fig. 2.10, which consist of the following subsystems,

- A superconducting magnet produces a 5 T magnetic field parallel to the beam direction. The field is uniformly good to 10^{-4} over a cylindrical volume of 20 mm in diameter and 20 mm long. This uniformity is necessary for DNP. The magnet is composed of a pair of Helmholtz coils, which are cooled to 4.2 K via a liquid helium reservoir located outside CLAS. Due to the coils, only the particles with scattering angle $0-50^o$ as well as $75-105^o$ are allowed to get in the CLAS.
- The 1 K refrigerator cools the target to 1 K.
- The target insert carries the four targets: the top one is ND_3, followed by carbon then NH_3, and finally an empty target, as shown in Fig. 2.11. The insert is moved up or down with a stepping motor, therefore, the target can be switched mechanically. Each target cell is 10 mm in length and 15 mm in diameter. The thickness of the cell walls is 0.2 mm. In addition, each cell is sealed using a 0.025 mm thick aluminum foil at entrance window, and 0.05 mm thick kapton foil at exit window. The insert also carries the NMR coils to monitor the polarization and the temperature sensors to monitor the temperature of the target materials.
- A microwave system provides the microwave field necessary to polarize the target material. The microwave frequency may be varied up to a bandwidth of 2 GHz. This allows to polarize the target into either negative or positive spin state without reversing the magnetic field.
- A NMR system. The NMR coils are surrounded the polarized target, and continuous wave NMR is used to monitor the NH_3 or ND_3 polarization.

Ref.[38] describes target system in more details.

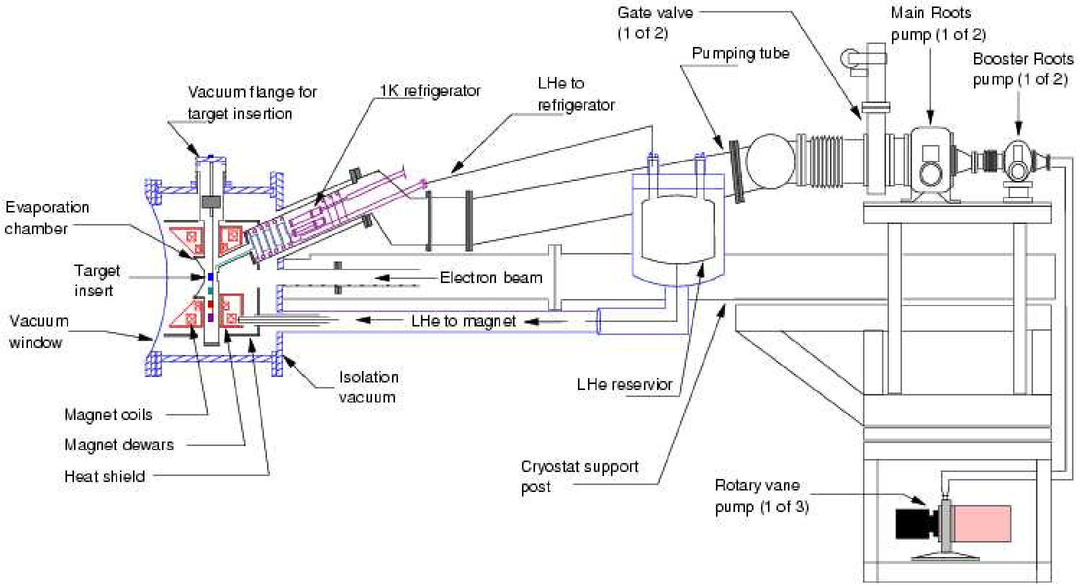

Figure 2.10. Cutaway view of EG1b polarized target system. The figure is from Ref.[38].

2.4.2 Polarized Target Materials

The polarized targets were frozen ammonia, $^{15}NH_3$ and $^{15}ND_3$. Ammonia was chosen because of its good resistance to depolarization by beam radiation. In addition ammonia has a high percentage of free nucleons, roughly 16.5% for $^{15}NH_3$ and 26.6% for $^{15}ND_3$. ^{15}N was chosen rather than usual ^{14}N ammonia because ^{15}N doesn't have any free neutron, whereas ^{14}N has one. All free nucleons can be polarized, while we only want the polarized nucleons in hydrogen or Deuterium. Therefore, ^{15}N ammonia could have a smaller correction and error than ^{14}N on the spin asymmetry measurement.

In summary, the performance goals of CLAS are summarized in Table 2.2.

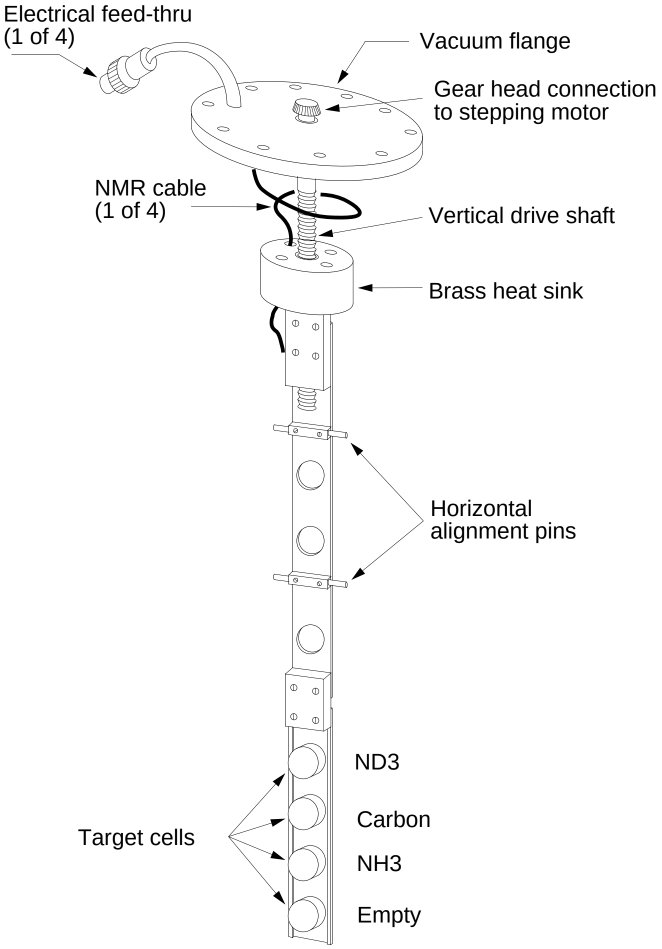

Figure 2.11. Schematic of target insert. The figure is from Ref.[38].

Table 2.2. Summary of the CLAS detector characteristics [37]

Capability	Quantity	Range
Coverage	charged particle angle	$8^o \leq \theta \leq 140^o$
	charged particle momentum	$p \geq 0.2$ GeV/c
	photon angle (4 sectors)	$8^o \leq \theta \leq 45^o$
	photon angle (2 sectors)	$8^o \leq \theta \leq 75^o$
	photon energy	$E_\gamma \geq 0.1$ GeV
Resolution	momentum ($\theta \lesssim 30^o$)	$\sigma_p/p \approx 0.5\%$
	momentum ($\theta \gtrsim 30^o$)	$\sigma_p/p \approx (1\text{-}2)\%$
	polar angle	$\sigma_\theta \approx 1$ mrad
	azimuthal angle	$\sigma_\phi \approx 4$ mrad
	time (charged particles)	$\sigma_t \approx (100\text{-}250)$ ps
	photon energy	$\sigma_E/E \approx 10\%/\sqrt{E}$
Particle ID	π/K separation	$p \leq 2$ GeV/c
	π/p separation	$p \leq 3.5$ GeV/c
	π^- misidentified as e^-	$\leq 10^{-3}$
Luminosity	electron beam	$L \approx 10^{34}$ nucleon $cm^{-2}s^{-1}$
	photon beam	$L \approx 5 \times 10^{31}$ nucleon $cm^{-2}s^{-1}$
Data acquisition	event rate	4 kHz
	data rate	25 MB/s
Polarized target	magnetic field	$B_{max} = 5$ T

CHAPTER 3

EVENT RECONSTRUCTION

3.1 overview

The data recorded during the experiment are mostly acquired from time-to-digital converters (TDCs) or analog-to-digital converters (ADCs). These TDCs and ADCs values, so-called “raw” data, can not directly be used for physics analysis. A CLAS reconstruction program converts TDCs and ADCs values into hits and tracks, and ultimately determines the energy and momentum of the particles. The process of reconstructing hits and tracks is called geometric reconstruction. To obtain proper measurements each detector element must be calibrated. Typically each detector component is calibrated separately, and the proper calibration constants obtained are stored in the database which is later used by data reconstruction program. Usually, both calibrating the detector and processing the data are done in several cycles to acquire a desired level of accuracy.

The final state particles of DVCS include an electron, a proton and a photon. Particle identifications in each event for the electron, proton and photon are crucial and require careful development. Although, particles are identified during the data processing, more stringent cuts are required to remove contamination from misidentified particles. Due to the alignment of the drift chamber position and small unknown shift of the torus magnetic field used in the reconstruction code, the electron momentum is always slightly shifted. To improve the accuracy, the electron momentum is studied resulting in momentum correction which are applied to the data. In addition, in this chapter, the proton energy loss correction, photon energy correction, and fiducial cuts are also discussed.

3.2 Track Reconstruction for Charged Particles

When a charged particle passes through the drift chamber, it ionizes the gas and produces the ions. The negative ions drift to the sense wires and and fire them. Each fired drift cell is called one "hit". To reconstruct the track of a charged particle, the adjacent hits are clustered in groups within each superlayer. In each cluster, there may be one or more track segments, therefore, a lookup table of road maps, which is generated by Monte Carlo procedure, is used to find the track segment which is consistent with a track crossing a superlayer. The identified track segments from each superlayers are linked together to form a track across the three regions within a sector. This also uses a look-up table. The track's initial parameters are estimated by comparing the track to the look-up table. Then, the track is fitted using the position of each hit, and is propagated through out of DC. This procedure is called hit-based track (HBT) fitting. The fit provides a preliminary momentum for the charged particle. Since the drift cell is comparatively small, the resolution of preliminary momentum is already 3% to 5%.

To further improve the tracking resolution, flight-time information is used to correct the track position. First, the particle's time of flight information is used to correct the measured drift times. The drift times are then converted to drift distances using a calibrated drift velocity. The final parameters of the track are acquired by fitting the corrected track positions of each drift cell. This procedure is called time based track (TBT) fitting.

The drift time is given by the following equation[29]:

$$t_{drift} = t_{start} + t_0 - t_{TDC} - t_{flight} - t_{prop} - t_{walk} \tag{3.1}$$

where,

- t_{start} is the event start time,
- t_0 is the fixed time delay for the wire,
- t_{TDC} is the raw time measured by the TDC,
- t_{flight} is the flight time of the particle from the reaction vertex to the wire,
- t_{prop} is the signal propagation time along the wire,

- t_{walk} is a time-walk correction made for short drift times due to different ionization for slow and fast particles.

Note that t_{TDC} is subtracted in the equation above because the TDCs are operated in common stop mode, where the start signal to TDCs is provided from the individual wire hits, while the stop is provided by a delayed version of the CLAS trigger[39]. All these parameters are acquired by DC calibrations.

Through a drift velocity function, the drift time determines the distance-of-closest-approach (DOCA) of the charged particle's trajectory to the sense wire. However, this distance can not predict which side of the wire the hit is on. This ambiguity is resolved within each superlayer by trying all combinations and selecting the most probable one. Once the sides of wire are decided, the final track is formed for each superlayer.

As described in the previous chapter, the target magnet is used to polarize the target during the experiment. The target magnet provides the longitudinal magnet field, therefore, when the charged particle fly from the the target to first Region of DC, the trajectory is bended in ϕ direction. Since the target magnet field decreases rapidly as distance increases, the effect is only limited in the space inside of the first Region of DC. Knowing the track information at first superlayer of DC and the target magnet field, the charged particle track is then traced to the reaction vertex to give initial direction (θ and ϕ).

3.3 Outer Detector Matching

Once the track of the charged particle is formed in DC, the track path is projected to the outer detector components, such as Cerenkov counters, Time-Of-Flight counters, and electromagnetic calorimeters. For a good track, each projected track must match a hit in each detector component. The matching requirements are listed for different detector components.

- Cerenkov counters

  As described in Chapter 2, the light-collection optics of Cerenkov counter system are placed in the shadows of magnet coils, therefore, Cerenkov counters do not provide azimuthal information of the reconstructed hit. For a good match, a polar angle different between projected hit and detected hit is less than 12^o.

- Time-Of-Flight counters

  $|z_p - z_h| < 30$cm is required for the matching of the projected track with the detected hit in TOF counters, where z_p is the z position of the projected hit and z_h is the z position of the detected hit on the TOF counter. Again no cut on azimuthal information is required.

- Electromagnetic calorimeter

  The three views of the electromagnetic calorimeter allow to reconstruct the hit position in the calorimeter. A good match to the calorimeter requires that the distance between the projected hit and detected hit should be less than 30 cm.

3.4 Start Time Reconstruction

In Eq. (3.1), the event start time, t_{start}, is used to calculate the drift time. The start time is not measured directly, but calculated from the electron's time of flight. The scattering electron is identified from negative tracks using only the signals from Electromagnetic Calorimeter and Cerenkov Counter. Once the electron is identified, the reaction start time can be traced back using the TOF signal and the flight path length (l) from target to TOF counter. The start time is given by following equation:

$$t_{start} = t_{tof} - \frac{l}{\beta c} \tag{3.2}$$

where t_{tof} is the time when the electron hits the TOF counter, β is the ratio of the electron speed to the light speed in the vacuum, and c is the speed of light in vacuum. Due to the comparatively high momentum and low rest mass for the electron, $\beta = 1$ is assumed. The resolution of the start time given with above equation is approximate 160 ps[40].

To further improve the accuracy of the start time, the information of RF structure of electron beam is used. Due to the RF structure of the accelerator, the beam is delivered in bunches referred to as the RF bucket. During experiment, the electron beam bucket is delivered to Hall-B every 2 ns. This RF time is know very precisely. The arrival time of the electron beam bucket is recorded. Ideally, the start time calculated with Eq. (3.2) should coincide with the arrival time of one of the electron buckets. While, due to the finite resolution, the reconstructed start time follows a Gaussian distribution with centroid around RF time. Since the width of the time resolution is much less than the time delay (2 ns) between two electron buckets, the RF time of the electron bucket initiating the event can be used to replace the reconstructed start time.

3.5 Neutral Particle Reconstruction

Compared to charged particles, the neutral particle is much easier to reconstruct. Neutral particles are detected by the electromagnetic calorimeter, scintillator counter, or both. The neutrals are identified as electromagnetic calorimeter hits that do not have matching DC tracks. The spatial location, deposited energy, and the time of the EC hit are enough to determine the four-momentum of the particle. Since both π^0 and η mesons decay into two photons, both of them can be reconstructed by detecting two photon hits. The invariant mass of two coincident photons can be used to identify π^0 or η. From the measured energy (E_γ) and the angle (θ_{12}) between two photons, the invariant mass ($M_{2\gamma}$) is given by[33]

$$M_{2\gamma} = 2E_{\gamma 1}E_{\gamma 2}(1 - cos\theta_{12}) \tag{3.3}$$

The resolution depends on the measured energy. The neutrons are distinguished from photons by EC timing (the flight from reaction vertex to EC). The neutron detection efficiency rises from zero at 0.4 GeV/c to a plateau of approximately 60% above 1.6 GeV/c[33].

3.6 Particle Identification

3.6.1 Electron Identification

During the EG1b run, the hardware trigger required coincident signals of the electromagnetic calorimeter and the Cerenkov counters to increase the likelihood that there was an electron candidate for each event. The CLAS reconstruction program rejects some of events using a more restrictive definition of an electron candidate. In the processed data, the electron candidates may be contaminated by negatively charged particles, such as high energy π^-, which can trigger both Cerenkov counters and calorimeter. In order to minimize the contamination from negative particles, additional cuts are utilized. This includes using the number of photoelectrons in Cerenkov counters, and the deposited energy in the calorimeter.

3.6.1.1 Cerenkov Cut

In CLAS, the Cerenkov counters are used to separate electrons from pions up to momentum of 2.5 GeV/c. However, pions with momentums above 2.5 GeV/c can produce Cerenkov light, and therefore, they are mis-identified as high energy electrons. To remove the pion contamination, a cut on the number of photoelectrons is used. The photoelectron distribution is shown in Fig. 3.1. The peak around 2 photoelectrons is due to detector acceptance of the Cerenkov light and high energy pions which emit the Cerenkov light. Detector acceptance is taken into account by fiducial cuts which will be discussed later in this chapter. The pion contamination is removed by requiring the number of photoelectrons greater than 2.5.

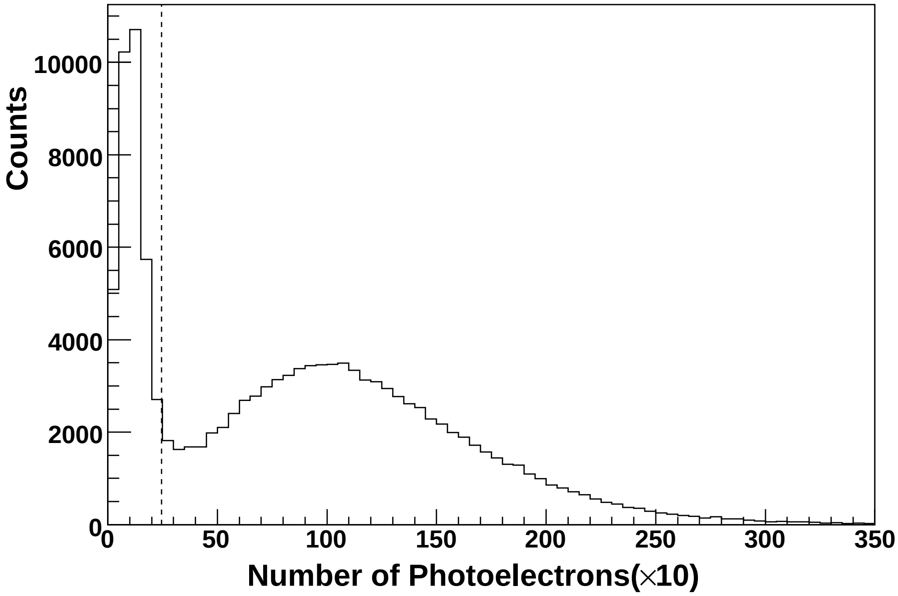

Figure 3.1. The number of photoelectrons detected in the Cerenkov counters for 5.625 GeV data. The dashed line indicates the applied cut, and electrons are selected by requiring the number of photoelectrons greater than 2.5. Events are from $ep \rightarrow epX$, requiring $Q^2 > 1$, $W > 2$.

3.6.1.2 Electromagnetic Calorimeter Cuts

Electrons and pions deposit energy in the calorimeter differently. Electrons interact in the calorimeter producing electromagnetic showers and release all of the energy, E_{tot}, which is proportional to their momentum, P. The constant $f_s = E_{tot}/P$ is the sampling fraction determined by the detector, and is around 0.27 in the case of CLAS. On the contrary, pions release the energy in the calorimeter by ionization and hadronic interactions, and only deposit part of their energy. For pions, the energy deposited in the inner and outer stacks of the calorimeter is independent on the pion energy and only depends on the detector thickness. Since the ratio of inner to outer stack thickness is 5:8, the ratio of the deposited energy in inner stack (E_{in}) to that in calorimeter (E_{tot}) is given by: $E_{in} : E_{tot} = 5 : 13$. The different interactions can be used to separate electrons from pions. In order to remove the pion contamination, the following cuts are applied, $E_{tot}/P > 0.2$ and $E_{in}/P > 0.08$, see Fig. 3.2.

3.6.2 Proton Identification

In this analysis, reaction $\vec{e}\vec{p} \rightarrow ep\gamma$ is studied, therefore, the proton is measured. During the standard event reconstruction, the proton is identified, however the proton identification can be improved.

The protons were identified with the charge, momentum, the track length from target to scintillator counters (SC) paddles, and the time-of-flight (TOF) from the target to SC paddles. The velocity of the proton can be calculated using the track length and the time of flight from the target to the scintillator. Then β can be calculated with the following equation[41]:

$$\beta = \frac{R}{c \cdot t^{TOF}} \tag{3.4}$$

where R is the track path length from the target to SC paddles and t^{TOF} is the time-of-flight after subtraction of event start time. On the other hand, β can also be calculated with equation[41]:

$$\beta_{calc} = \frac{p}{\sqrt{p^2 + m^2}} \tag{3.5}$$

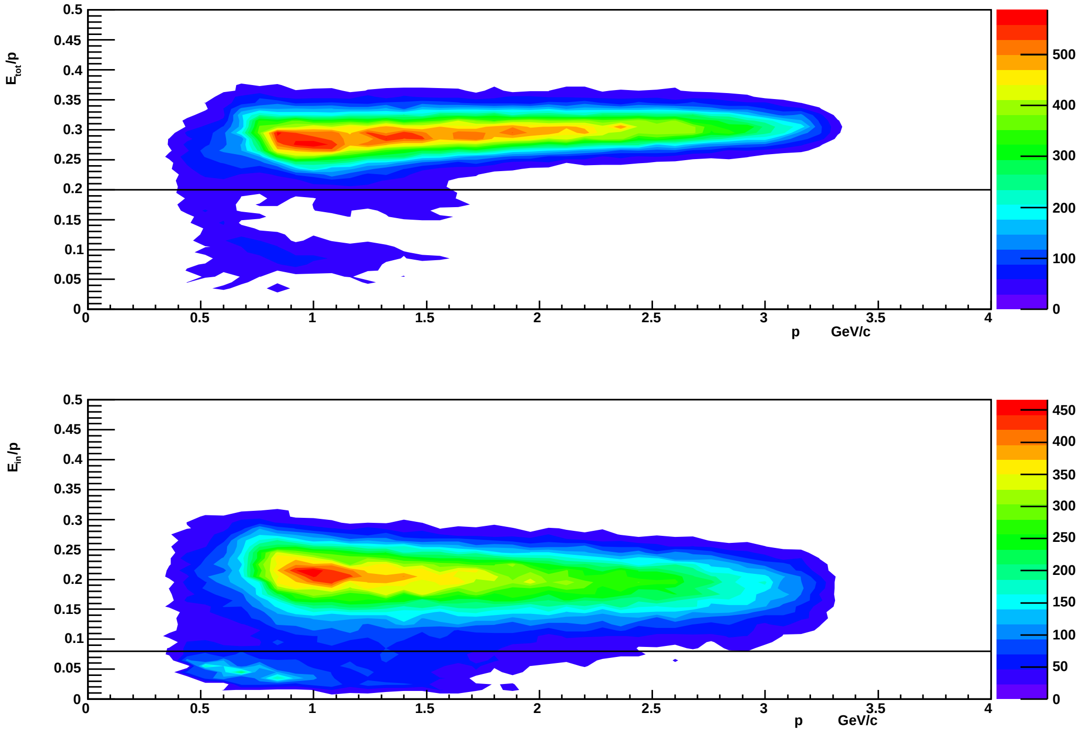

Figure 3.2. Electromagnetic calorimeter cuts. In the upper plot the straight line shows E_{tot}/p cut, and in the lower one the line shows E_{in}/p. Electrons are selected by requiring $E_{tot}/P > 0.2$ and $E_{in}/P > 0.08$. Event samples are from $ep \rightarrow epX$, requiring $Q^2 > 1$, $W > 2$.

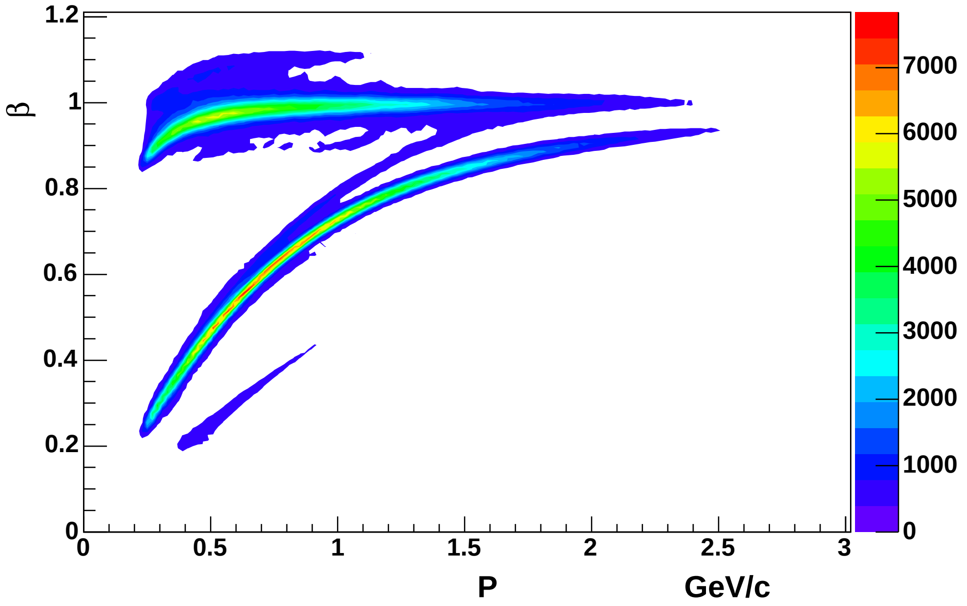

Figure 3.3. The dependence of β from Eq.(3.4)on the measured momentum for positively charged particles. Bands for pions, protons and deuterons are clearly visible.

where m is the rest mass of the charged particles(e.g., proton, pion, kaon, deuteron etc.), and p is the measured momentum.

Fig. 3.3 shows β versus the measured momentum (p) for positively charged particles. Due to the different rest masses, bands for pions, protons and deuterons are clearly visible. To isolate the proton band, the β from Eq.(3.4) is compared with β_{calc} from Eq.(3.5) in which m is set as the proton mass. The difference between β and β_{calc} is shown in Fig. 3.4. With the proton identification defined as $|\beta - \beta_{calc}| < 0.05$. The proton is well identified, as shown in Fig. 3.5.

3.6.3 Photon Identification

A neutral particle is identified with the electromagnetic calorimeter information. The neutrals are identified as EC hits that do not have matching DC tracks. The neutron and photon can be separated with time-of-flight from the target to the calorimeter. In Figure 3.6, the sharp peak around $\beta = 1$ corresponds to photons. A strict cut $\beta > 0.95$ is used to

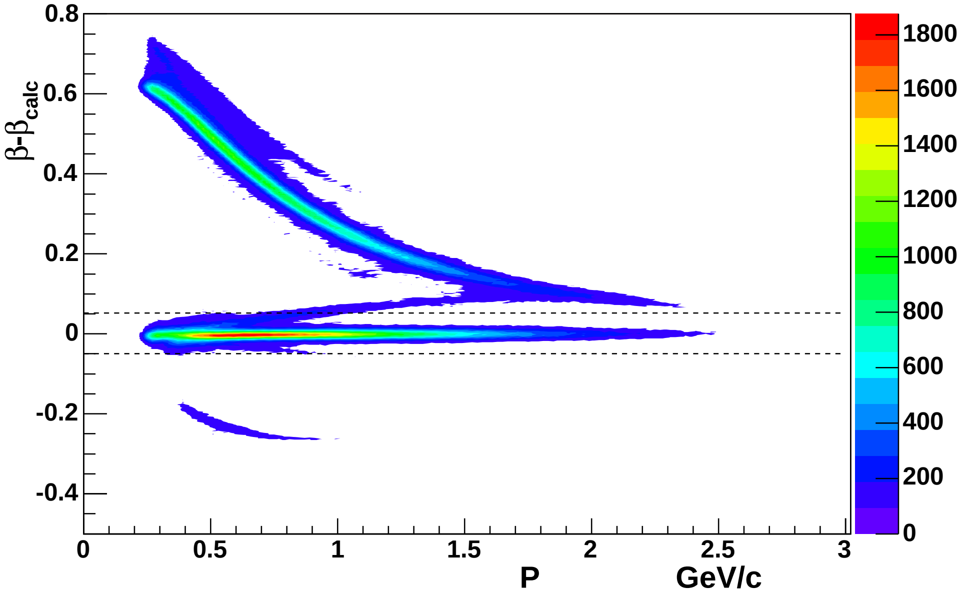

Figure 3.4. The distribution of $\beta - \beta_{calc}$ as a function of momentum for positively charged particles. β_{calc} is calculated with Eq.(3.5) assuming $m = 0.938\,(\mathrm{GeV/c^2})^2$. Three clearly visible bands are corresponding to pions, protons and deuterons. Protons are selected requiring $|\beta - \beta_{calc}| < 0.05$.

select photons for photon energy corrections and π^0 reconstructions. Here, it is worthwhile mentioning that the photon identification is not used to select the reaction $\vec{e}\vec{p} \rightarrow ep\gamma$. In this analysis, all neutrals are included, and the angular cut (see Chapter 5) can remove the events with neutrons.

3.7 Corrections

3.7.1 Electron Momentum Correction

The reconstructed electron momentum has systematic uncertainties, which can be seen from the slight shift of the elastic peak in the W distribution of inclusive electrons, as shown in Fig. 3.7. The peak is shifted to the left from the theoretical value 0.9382 GeV/c^2, and is also broader than what it should be expected from the CLAS resolution. This is a well known problem due to the misalignment of the drift chambers to normal positions,

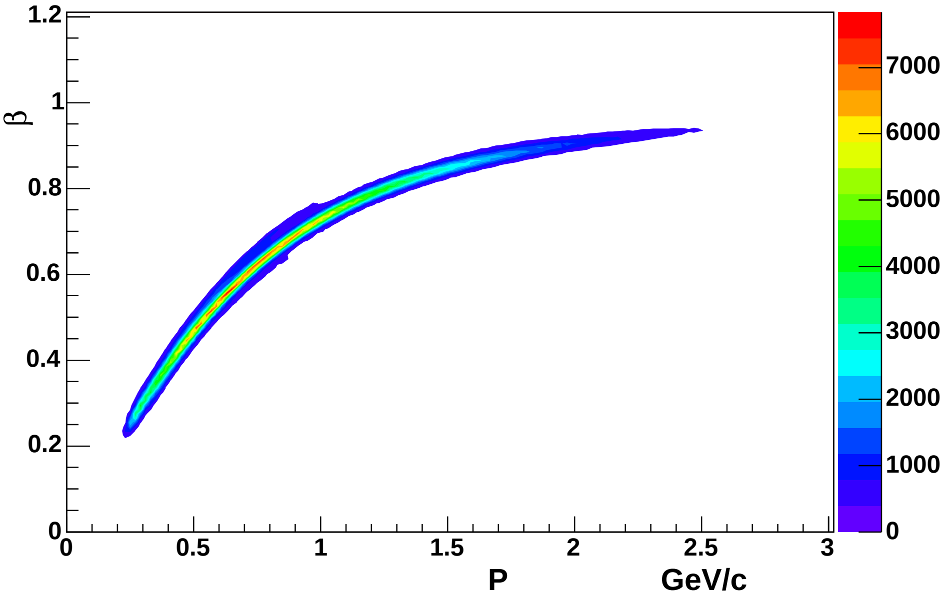

Figure 3.5. The dependence of β on momentum for positively charged particles after the proton cut.

incomplete knowledge of the shape and location of the torus coils, and incorrect information of drift chambers in reconstruction code. An electron momentum correction method was developed by A. Klimenko [42] for the E6 experiment and is also used for EG1b. This method corrects both the electron momenta and polar angles, assuming that the momentum deviations are due to systematic displacements of the drift chambers and magnetic field differences from the field map used in the reconstruction code. The effect of drift chamber displacements on the given reconstructed track is written as a change $\Delta\theta$ in the polar angle and a change Δp in the momentum:

$$\Delta\theta = (A + B\phi)\frac{cos\theta}{cos\phi} + (C + D\phi)sin\theta, \tag{3.6}$$

and

$$\frac{\Delta p}{p} = ((E + F\phi)\frac{cos\theta}{cos\phi} + (G + H\phi)sin\theta)\frac{p}{qB_{Torus}} \tag{3.7}$$

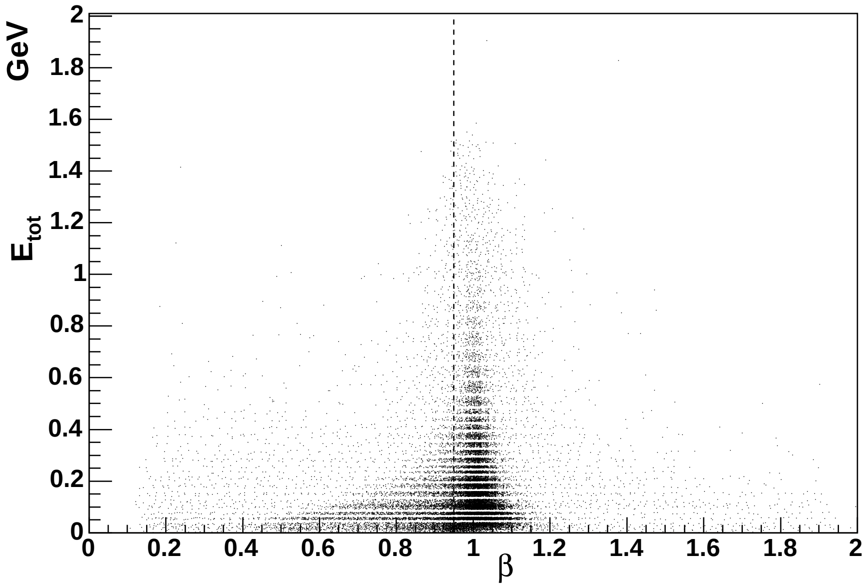

Figure 3.6. The total energy of a hit in EC for all of neutrals before (left) and after (right) photon ID

where q is the particle charge, p is the reconstructed momentum, θ is the reconstructed scattering polar angle, and ϕ is the reconstructed azimuthal angle which is untouched in this method. In Eq. (3.7), p/qB_{Torus} is proportional to the amount of curvature of the track, which determines the effect of a misalignment of the drift chambers. B_{Torus} is a function of θ: $B_{Torus} = 0.76\frac{I_{Torus}}{3375}\frac{sin^2 4\theta}{\theta}$ for $\theta < \frac{\pi}{8}$ and $B_{Torus} = 0.76\frac{I_{Torus}}{3375\theta}$ for $\theta > \frac{\pi}{8}$. The magnetic field deviation from the field map encoded in the reconstruction code is corrected by adding another function $f(\theta,\phi)$ to Eq. (3.7). The function $f(\theta,\phi)$ is parameterized as follows:

$$f = (Jcos\theta + Ksin\theta + Lsin2\theta) + (Mcos\theta + Nsin\theta + Osin2\theta)\phi \tag{3.8}$$

with another 6 parameters (J-O).

The 14 parameters (A-O) in above equations are determined based on sector by sector using the elastic scattering p(e,e'p'). The elastic events p(e,e'p') are selected by requiring $179^o < |\phi_e - \phi_p| < 181^o$, $|E(miss)| < 0.1$ GeV, $|P_z(miss)| < 0.1$ GeV/c, $|P_x(miss)| < 0.07$

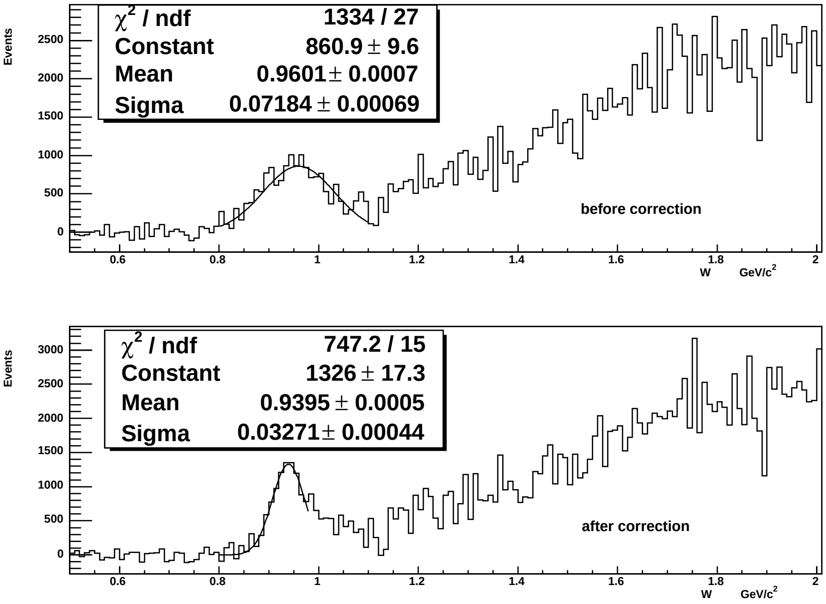

Figure 3.7. W elastic peak for inclusive electron scattering before (top) and after (bottom) the momentum correction. The data are 5.6 GeV inbending data. After applying the momentum correction, both the peak position and peak width are improved.

GeV/c, and $|P_y(miss)| < 0.07$ GeV/c (Fig. 3.8). Technical details about the fitting program is described in the CLAS note 2003-005[42].

After the 14 parameters are acquired, both electron polar angle and momentum can be corrected:

$$\begin{aligned} \theta &\rightarrow \theta + \Delta\theta, \\ p &\rightarrow p(1 + \frac{\Delta p}{p}). \end{aligned} \tag{3.9}$$

Fig. 3.7 show the W distribution for inclusive electron scattering after applying the electron momentum corrections. After corrections, both the centroid and the width of the peak are improved, and closer to theoretical values.

As discussed above, the 14 parameters for the electron momentum correction are determined from the elastic p(e,e'p') events, while in this analysis, the kinematics of DVCS events are a little bit different with those of elastic events. To verify if the above method is applicable in this analysis, the MM_X^2 of (ep) for both $ep \rightarrow ep\gamma$ and $ep \rightarrow ep\pi^0$ is studied.

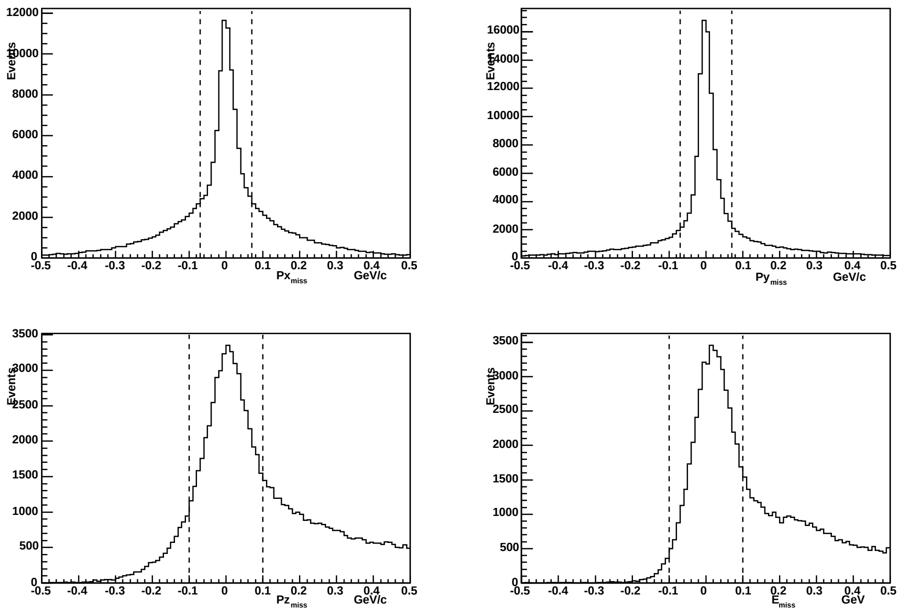

Figure 3.8. The missing four momenta distribution of events within $179^o < |\phi_e - \phi_p| < 181^o$. The dashed lines represent the cuts applied to select elastic events, which are used to determine the parameters (A-0).

As deep inelastic scattering (DIS), both $ep\gamma$ and $ep\pi^0$ are selected requiring $Q^2 > 1\,\mathrm{GeV}^2/\mathrm{c}^2$ and $W > 2$ GeV/c^2. For $ep\gamma$ selection, the events with only one electron, one proton and one photon are selected. Due to the calorimeter coverage (8^o to 45^o), one detected photon events do not mean the single photon production, because the second photon can escape the detection. Therefore, to clean photon production, an angular cut $\theta_{\gamma\gamma'} < 1^o$ is applied, where $\theta_{\gamma\gamma'}$ is the angle difference between the detected photon (γ) with the calorimeter and the calculated photon (γ') expected from ep. The π^0 can be reconstructed from two detected photons requiring invariant mass of two photons ($M_{\gamma\gamma}$) between 0.1 GeV/c^2 to 1.8 GeV/c^2. To clean π^0 production, the angular cut $\theta_{\pi^0 X} < 2^o$ is used, where $\theta_{\pi^0 X}$ is the angle difference between the reconstructed pion (π^0) and the calculated pion (X) expected from ep. Both inbending data and outbending data are tested. The plots in Fig. 3.9, Figure 3.10, Figure 3.11, and Figure 3.12 show that the electron momentum correction works well for deep inelastic scattering events.

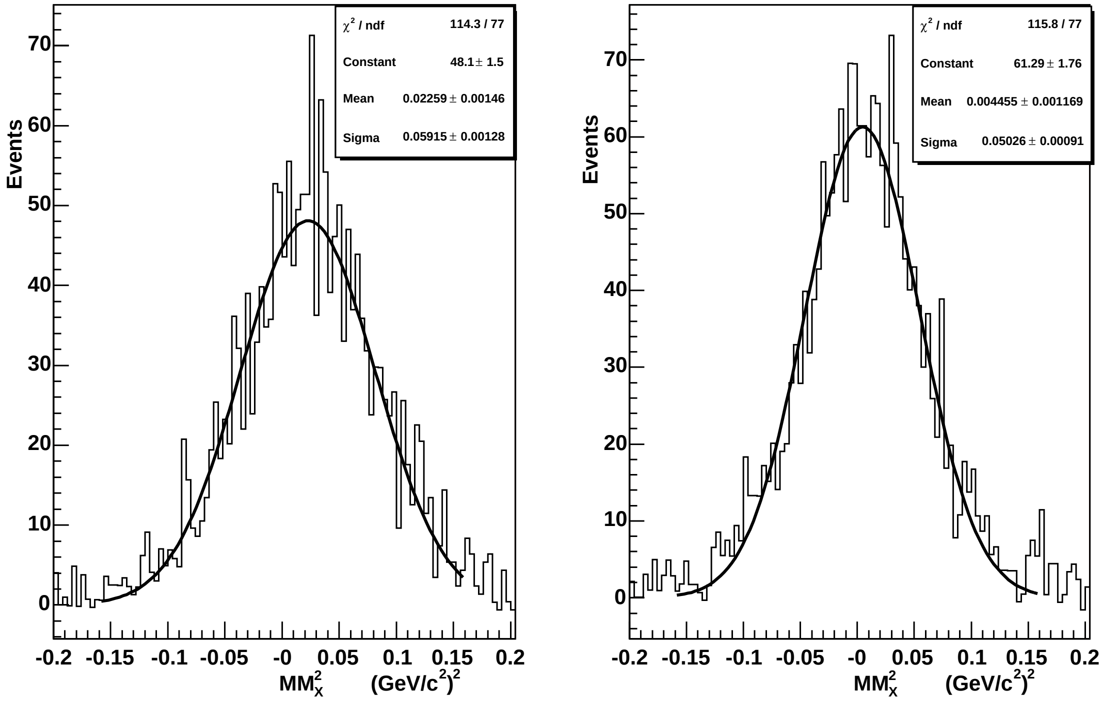

Figure 3.9. The MM_X^2 of (ep) for $ep \to ep\gamma$ before (left) and after(right) the electron momentum correction. Events are selected by requiring $W > 2$ GeV/c^2, $Q^2 > 1\,\mathrm{GeV}^2/\mathrm{c}^2$, and $\theta_{\gamma\gamma'} < 1^o$, where γ is the detected photon with calorimeter, and γ' is the calculated photon expected from $ep \to epX$. The data are from the inbending data set. The centroid and width of the MM_X^2 peak is improved as a result of electron momentum corrections.

3.7.2 Proton Energy Loss Correction

Due to the ionization losses, the low momentum protons lose some energy when they pass through the target and the CLAS detector. This can be seen in the plot of MM_X^2 versus the proton kinematic energy. In the upper panel of Figure 3.14, due to the proton energy loss, the centroid of MM_X^2 becomes negative as the proton kinetic energy T_p becomes smaller.

The proton energy loss correction function is derived from GEANT simulations which simulates the physics of energy loss due to material in the trajectory path. The generated DVCS events were used as an input for GEANT, and the protons were reconstructed with the CLAS reconstruction program. The relationship between the generated and reconstructed proton momenta are parameterized, as shown in Fig. 3.13, and the correction function is

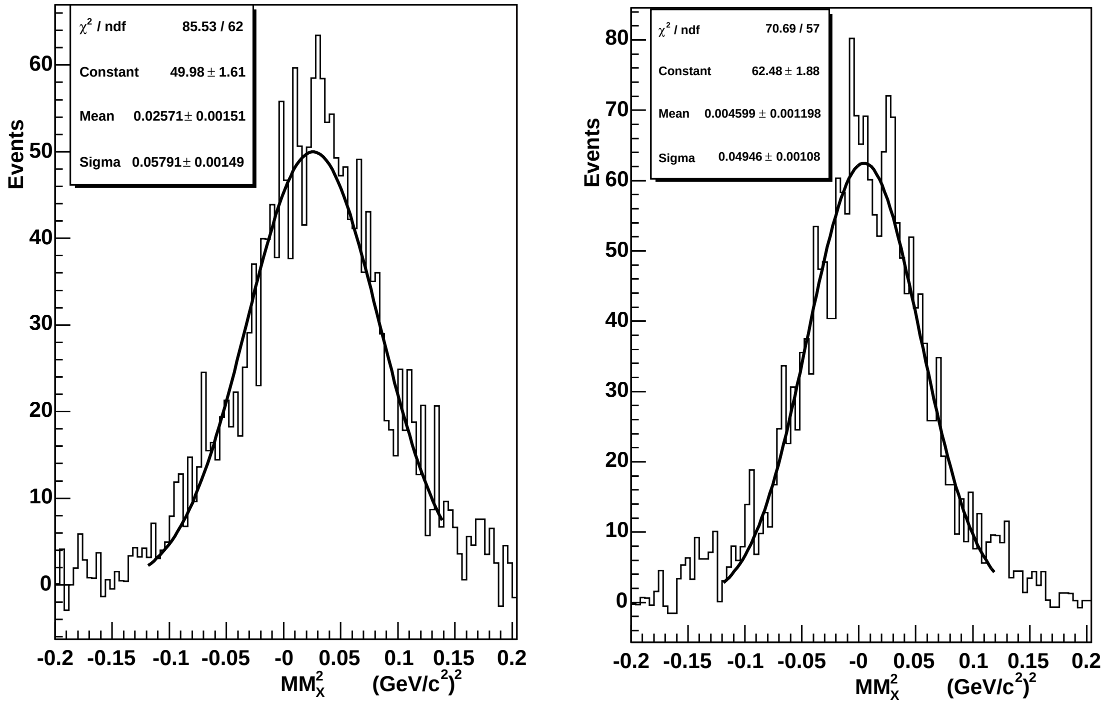

Figure 3.10. The MM_X^2 of (ep) for $ep \rightarrow ep\gamma$ before (left) and after(right) the electron momentum correction. The data are selected by requiring $W > 2$ GeV/c^2, $Q^2 > 1\,\mathrm{GeV}^2/\mathrm{c}^2$, and $\theta_{\gamma\gamma'} < 1^o$, where γ is the detected photon with calorimeter, and γ' is the calculated photon expected from $ep \rightarrow epX$. The data are from the outbending data set.The centroid and width of the MM_X^2 peak is improved as a result of electron momentum corrections.

given by,

$$P_p = P_m + P_m(5.1771 \times 10^{-2} - \frac{6.4041 \times 10^{-2}}{P_m} + \frac{2.2657 \times 10^{-2}}{P_m^2}) \tag{3.10}$$

where P_m is the measured momentum of the proton, and P_p is the corrected momentum of the proton in unit of GeV/c.

After applying the above energy loss correction function, the MM_X^2 is independent of the proton kinetic energy as seen in the lower panel of Figure 3.14.

3.7.3 Photon Energy Correction

In the CLAS reconstruction code, the photon energy is calculated with the following formula,

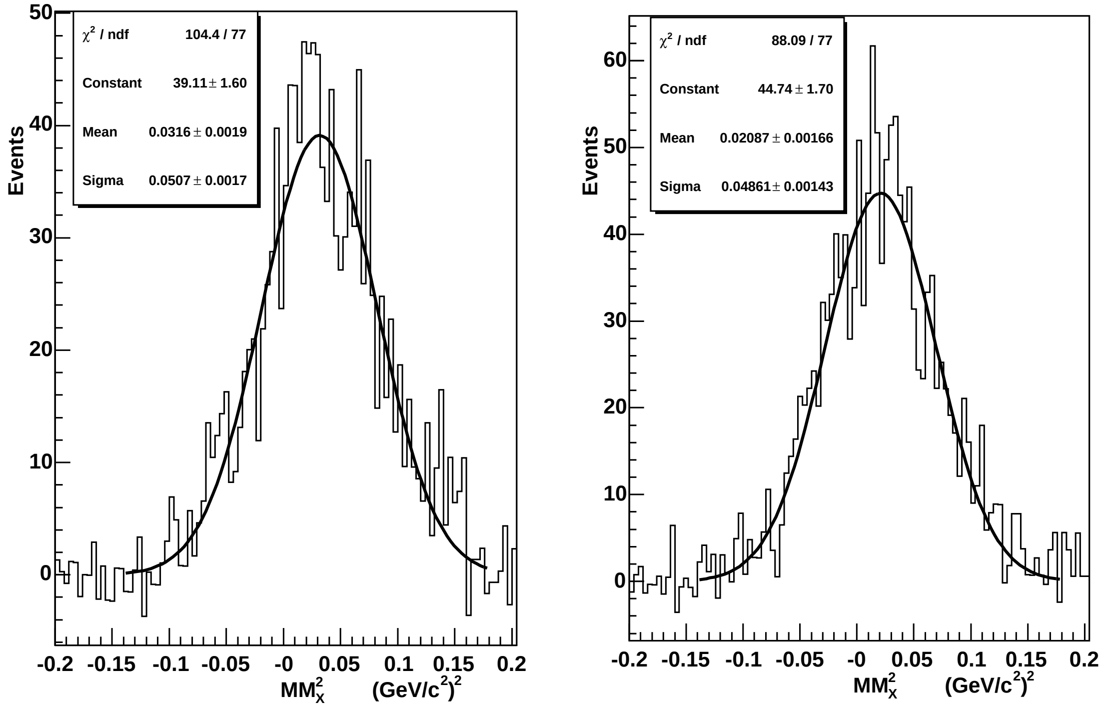

Figure 3.11. The MM_X^2 of (ep) for $ep \to ep\gamma\gamma$ before (left) and after(right) the electron momentum correction. The data are selected by requiring $W > 2$ GeV/c^2, $Q^2 > 1\,\mathrm{GeV}^2/\mathrm{c}^2$, $0.1\,\mathrm{GeV/c}^2 < M_{\gamma\gamma} < 0.18\,\mathrm{GeV/c}^2$ and $\theta_{\pi^0 X} < 2^o$, where the π^0 is reconstructed from two detected photons with calorimeter, and X is expected from ep. The data are from the inbending data set. The centroid and width of the MM_X^2 peak is improved as a result of electron momentum corrections.

$$E_\gamma = E_{ec}/f_s, \tag{3.11}$$

where E_{ec} is the total visible energy deposited in the scintillators, and f_s is the sampling fraction, which is the ratio of energy deposited in the active part of the calorimeter (scintillator) and the incident particle energy. The value $f_s = 0.273$ is typically used. It works well for photons with energy less than 1 GeV. But for high energy photons, especially those with energy greater than 2 GeV, it does not work well. The reconstructed energy of the high energy photon is over estimated. See Fig. 3.15.

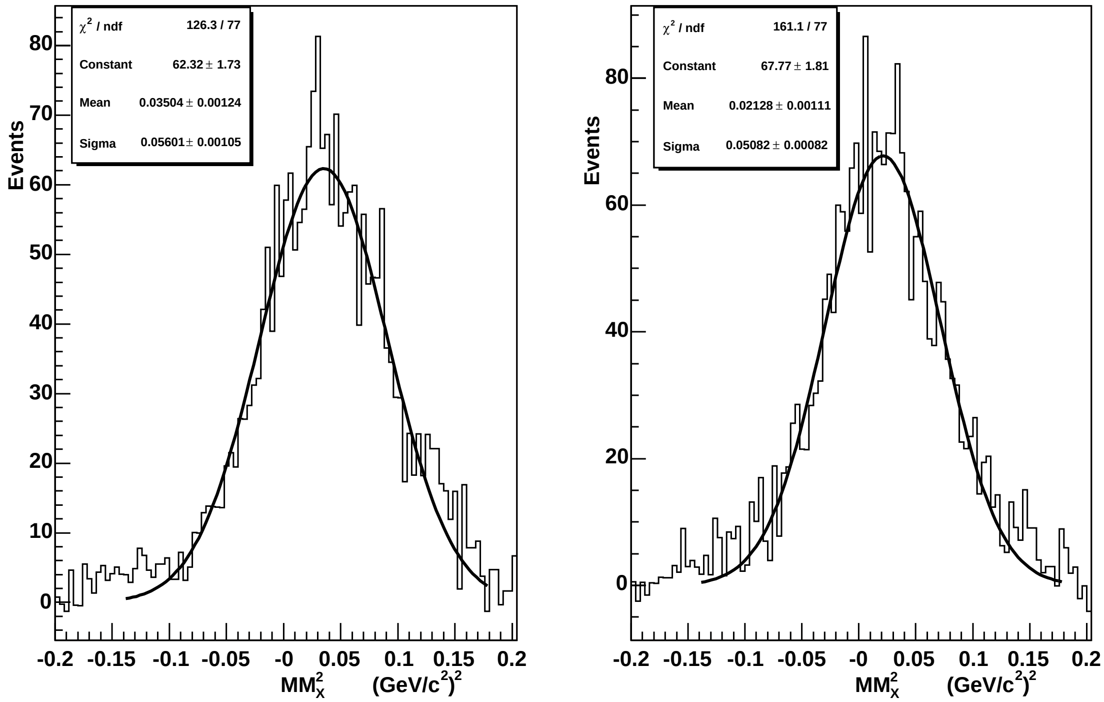

Figure 3.12. The MM^2_X of (ep) for $ep \rightarrow ep\gamma\gamma$ before (left) and after(right) the electron momentum correction. The data are selected by requiring $W > 2$ GeV/c^2, $Q^2 > 1\,\text{GeV}^2/\text{c}^2$, $0.05\,\text{GeV/c}^2 < M_{\gamma\gamma} < 0.18\,\text{GeV/c}^2$ and $\theta_{\pi^0 X} < 2^o$, where the π^0 is reconstructed from two detected photons with calorimeter, and X is the calculated π^0 expected from $ep \rightarrow epX$. The data are from the outbending data set. The centroid and width of the MM^2_X peak is improved as a result of electron momentum corrections.

To correct the photon energy, f_s is estimated using the reconstructed energy and reconstructed momentum of electrons, for which f_s depends also on scintillator quality and software reconstruction algorithms. The dependence of sampling fraction on the electron energy is shown in Fig. 3.16, and it is parameterized as the following function,

$$f_s = 0.3065 - 0.03356/E. \tag{3.12}$$

From Eq.(3.12), f_s as a function of E_{ec} can be concluded as follows,

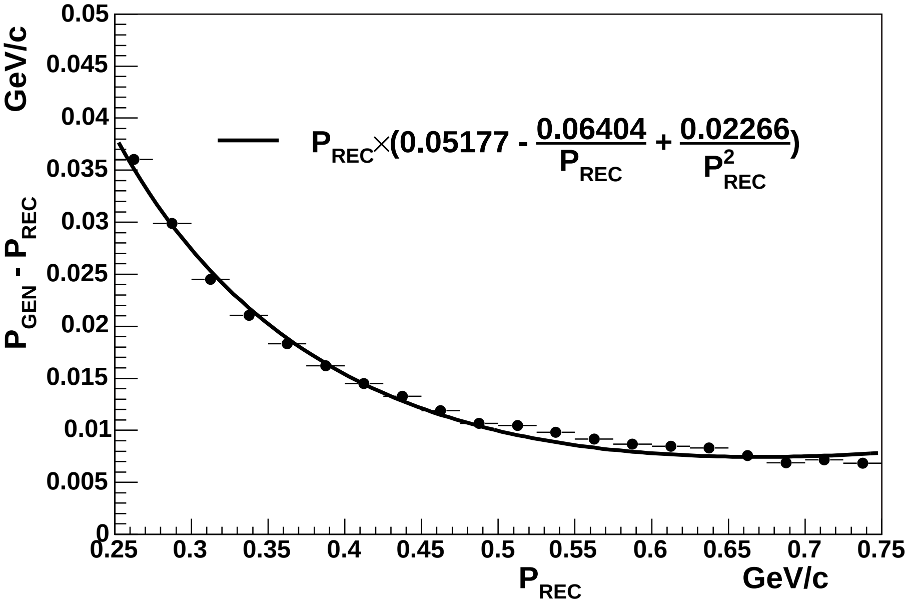

Figure 3.13. The proton momentum correction function (solid line) from GEANT simulations. The points are profiles of the difference between the generated proton momentum and the reconstructed proton momentum versus the reconstructed proton momentum.

$$\begin{aligned} f_s \cdot E_{ec} &= 0.3065 \cdot E_{ec} - 0.03356 \cdot E_{ec}/E, \\ f_s \cdot E_{ec} &= 0.3065 \cdot E_{ec} - 0.03356 \cdot f_s, \\ f_s \cdot (E_{ec} + 0.03356) &= 0.3065 \cdot E_{ec}, \\ f_s &= \frac{0.3065 E_{ec}}{E_{ec} + 0.03356}. \end{aligned} \tag{3.13}$$

When the energy of the photon is greater than 1 GeV, the energy is recalculated using the above new sampling fraction with Eq.(3.11). Fig. 3.17 shows the dependence of missing energy on photon energy for reaction $ep \to e'p'\gamma X$ after photon energy correction. Comparing with Fig. 3.15, the energy of high energy photon is greatly improved after f_s correction.

One may ask if the sampling fraction of the electron is different from that of the photon. GEANT studies show that the sampling fraction f_s is same for both photons and electrons with the exception of a few percent difference at low energies. See Fig. 3.18.

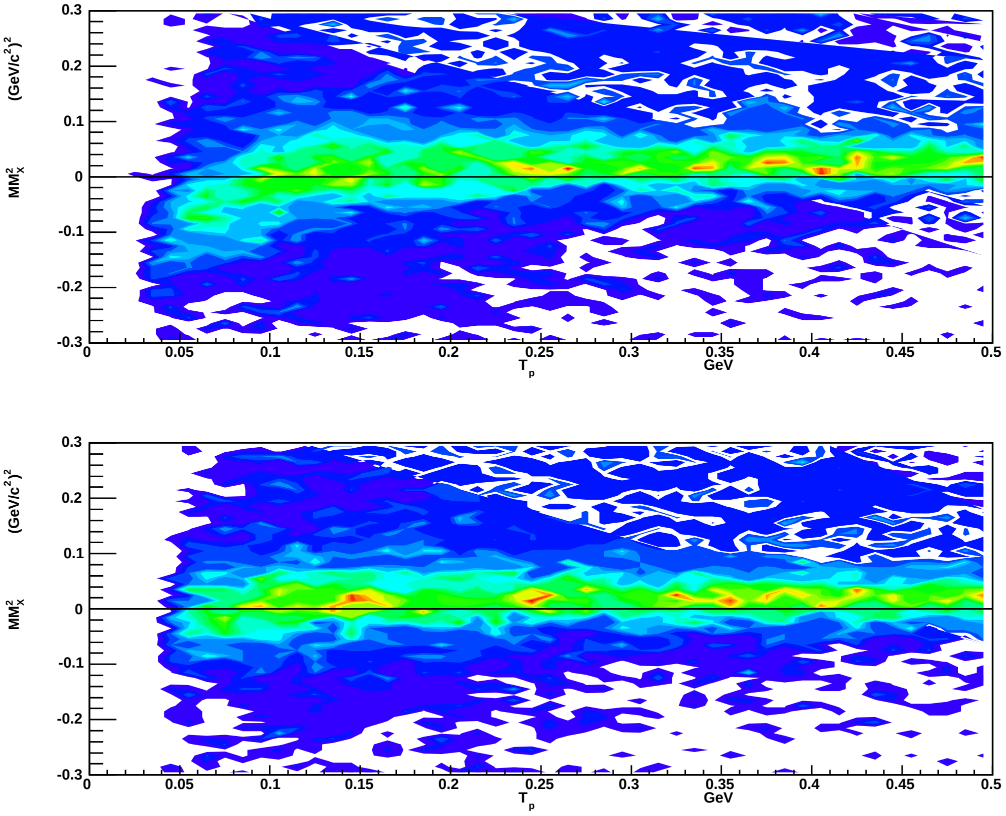

Figure 3.14. Missing mass squared of (*ep*) dependence with respect to the proton kinetic energy for the reaction $ep \to ep\gamma$. The upper (lower) panel is before (after) proton energy loss correction. Due to contribution from π^0 events, the centroid of MM_X^2 is above 0.

3.8 Fiducial Cuts

The CLAS detector has holes and regions where the acceptance efficiency is not 100%. The holes are mainly because of the torus coils, and some are due to the hardware problem, such as dead wires in drift chambers, broken PMTs in Time-Of-Flight counters. For electrons, the Cerenkov efficiency fluctuates very much at the edge of the detecter, which is pooly understand (see Fig. 3.19). To reduce the systematic uncertainties due to the inefficient regions, the events detected by inefficient part are excluded from the data. These cuts are called fiducial cuts. Therefore, fiducial cuts for electrons, protons, and photons are developed.

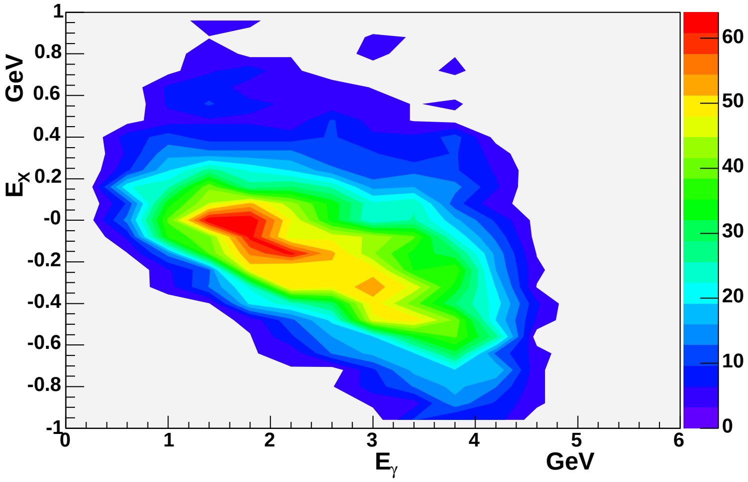

Figure 3.15. The missing energy (E_X) vs photon energy for reaction $ep \to e'p'\gamma X$. The average E_X goes to negative as the photon energy increases, for the energy of the high energy photon was over estimated in reconstruction codes.

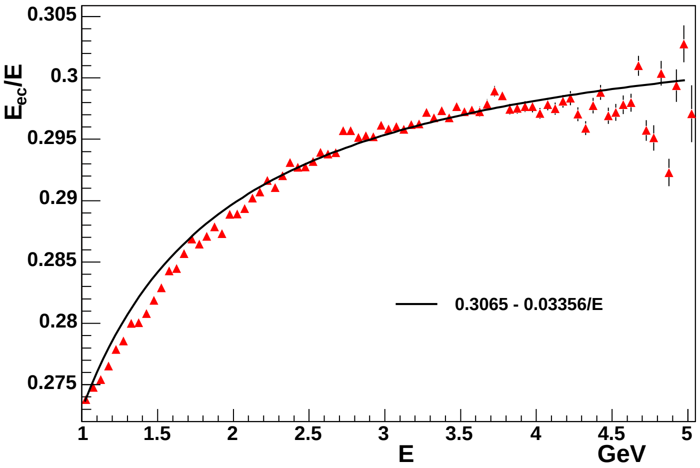

Figure 3.16. The dependence of sampling fraction f_s on the electron energy. E is the energy calculated using the momentum ($E = \sqrt{p^2 + m^2}$). E_{ec} is the total energy deposited in the scintillators.

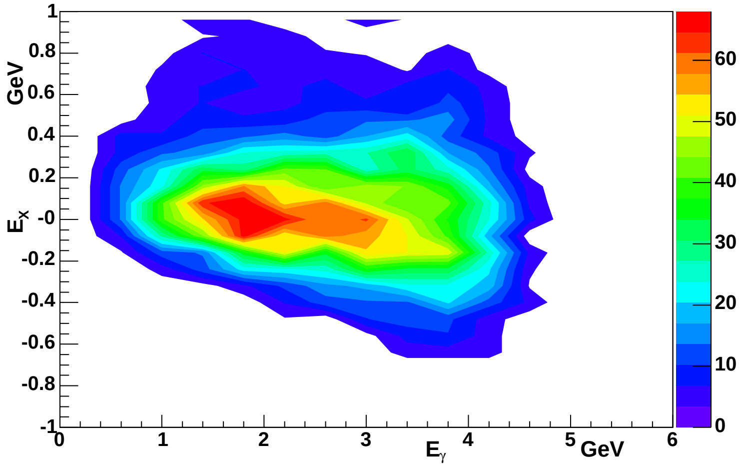

Figure 3.17. The missing energy vs photon energy for reaction $ep \to e'p'\gamma X$ after photon energy correction.

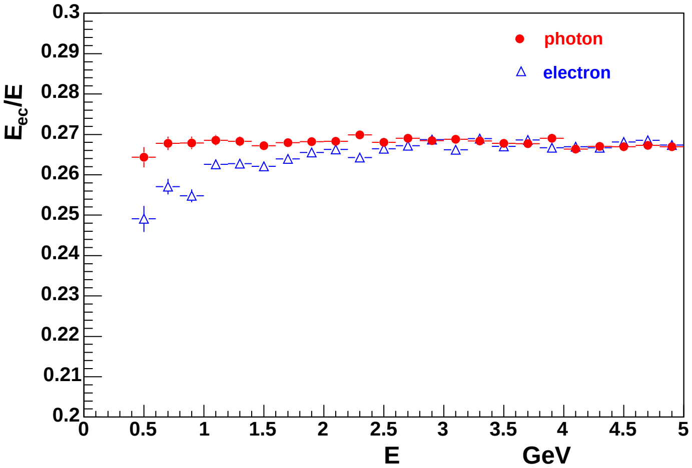

Figure 3.18. The GEANT studies on dependence of sampling fraction f_s on the energy for both electrons and photons.

Since the acceptance efficiency depends on the torus current, the fiducial cuts are studied for each data set with different torus current.

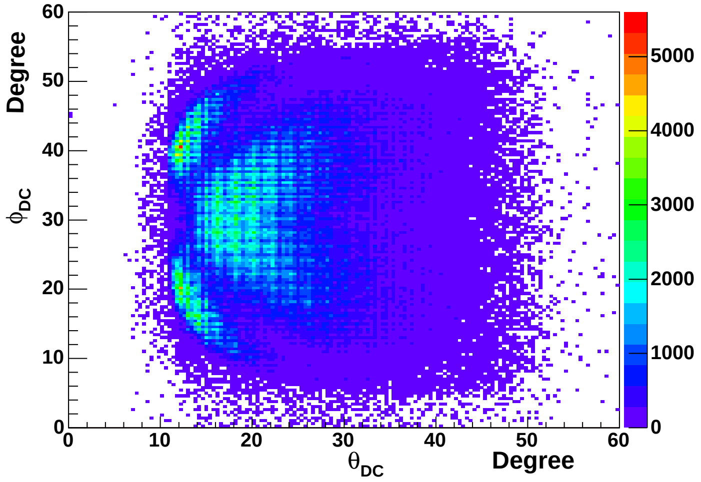

Figure 3.19. The number of photoelectrons vs ϕ_{DC} vs θ_{DC} for electrons with momentum between 1 and 3 GeV/c. The inefficient regions close to the edge are clearly visible. The data are 5.6 GeV inbending data.

3.8.1 Electron Fiducial Cut

The electron fiducial cut for EG1b data is developed by Volker Burkert and modified by Vipuli Dharmavardane[43, 44]. The cut is determined by evaluating the Cerenkov efficiency in the θ versus ϕ plane. For each bin of (θ,ϕ), the number of photoelectrons is a Poisson distribution, therefore, the inefficiency for each bin is calculated as:

$$\text{inefficiency} = \sum_{n=0}^{n<c} \frac{\mu^n e^{-\mu}}{n!} \tag{3.14}$$

where c is the threshold of Cerenkov counters by unit of number of photoelectrons, and μ is the expected average number of photoelectrons. In this analysis, 80% efficiency is acceptable. With known inefficiency, μ is determined for each data set. Then, the inefficiency function can be extracted.

For inbending electrons, the efficiency function of θ and ϕ has been studied[45]. The fiducial region is defined as the area with an efficiency greater than 80%. For outbending electrons, the efficiency function is not available. The inefficiency area is identified by the number distribution of photoelectrons on ϕ versus θ plane.

The general form of the fiducial cut for inbending electrons is as follows:

$$30^o - \Delta\phi < \phi_{sec} < 30^o + \Delta\phi \tag{3.15}$$

$$45^o > \theta_{DC} > \theta_{cut} \tag{3.16}$$

where ϕ_{sec} is the azimuthal angle at DC superlayer 1 in sector coordinates, i.e., ranging between 0 and 60^o. $\Delta\phi$ and θ_{cut} are given by

$$\Delta\phi = A(sin(\theta_{DC} - \theta_{cut}))^{expon} \tag{3.17}$$

$$expon = B(p_{scaled})^C \tag{3.18}$$

$$\theta_{cut} = D + \frac{E}{p_{scaled} + F} \tag{3.19}$$

where $p_{scaled} = p\frac{3375}{I}$, is the electron momentum normalized to the maximum torus current 3375 A. By the normalization, the torus current effect on the fiducial cut is removed. θ_{cut} is the minimum polar angle for accepted electrons, which depends on the electron momentum. The parameter D takes care of θ_{cut}. The parameter E is related to how much the electron is bended into the beam direction by the torus magnetic field. The parameter F controls how much θ_{cut} depends on the electron momentum. Parameters A, B, and C control the azimuthal angle range for accepted electrons. The parameters A through F are found empirically, and listed in the Table 3.1. Fig. 3.20 shows the example for applied electron fiducial cut. The angular distribution before and after the cut is shown in Fig. 3.21, and it is clear that the low efficient region is removed.

The outbending electrons have different inefficient regions with the inbending electrons, see Fig. 3.22. The center area of each sector is also low efficient region for outbending

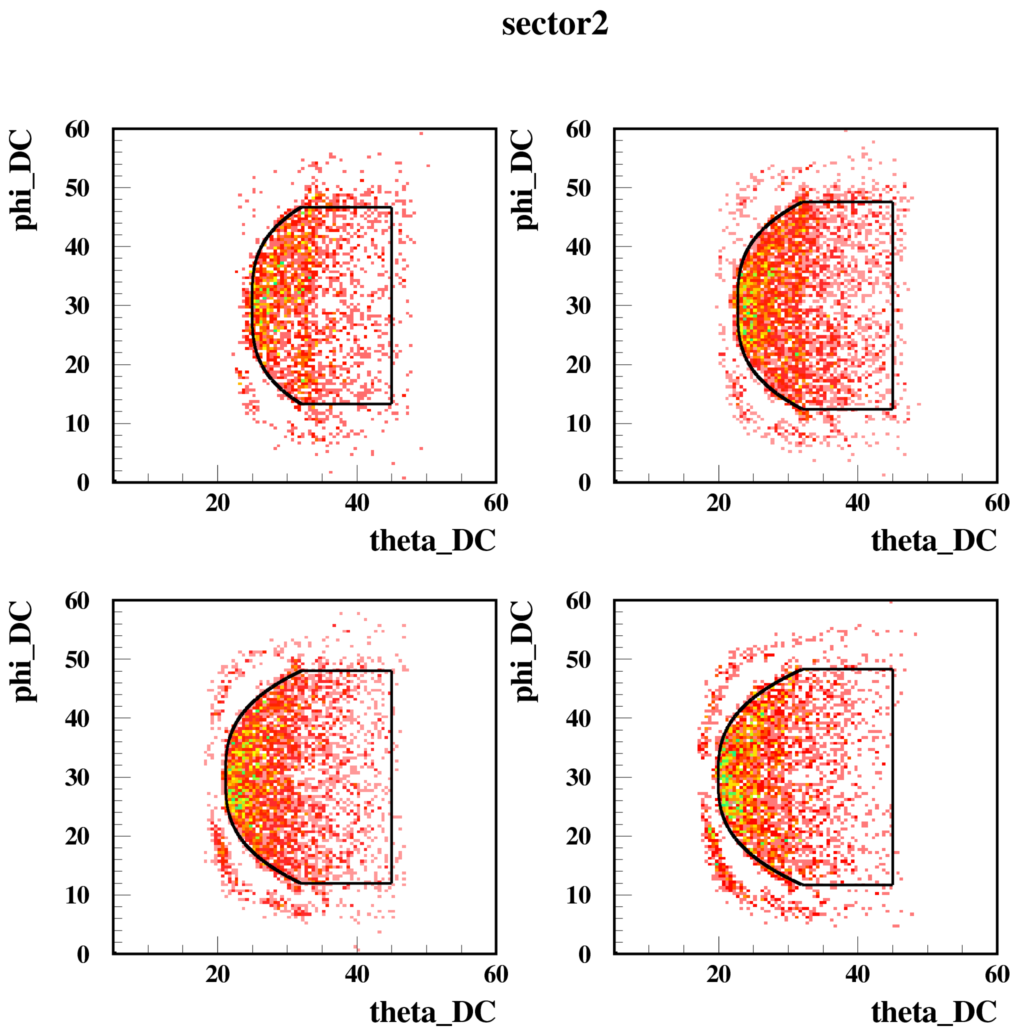

Figure 3.20. The number of photoelectrons distribution on ϕ vs θ plane for four momentum bins, and the electrons are detected by sector 2. The region inside black lines represent the fiducial area. The plots is a courtesy of V. Dharmavardane.

electrons, therefore, in addition to the edge of each sector, the center area is also excluded. The general forms of the fiducial cut for outbending electrons are as follows,

$$30^o - \Delta\phi < \phi_{sec} < 30^o + \Delta\phi, \tag{3.20}$$

$$\theta_{mas} > \theta_{DC} > \theta_{cut}, \tag{3.21}$$

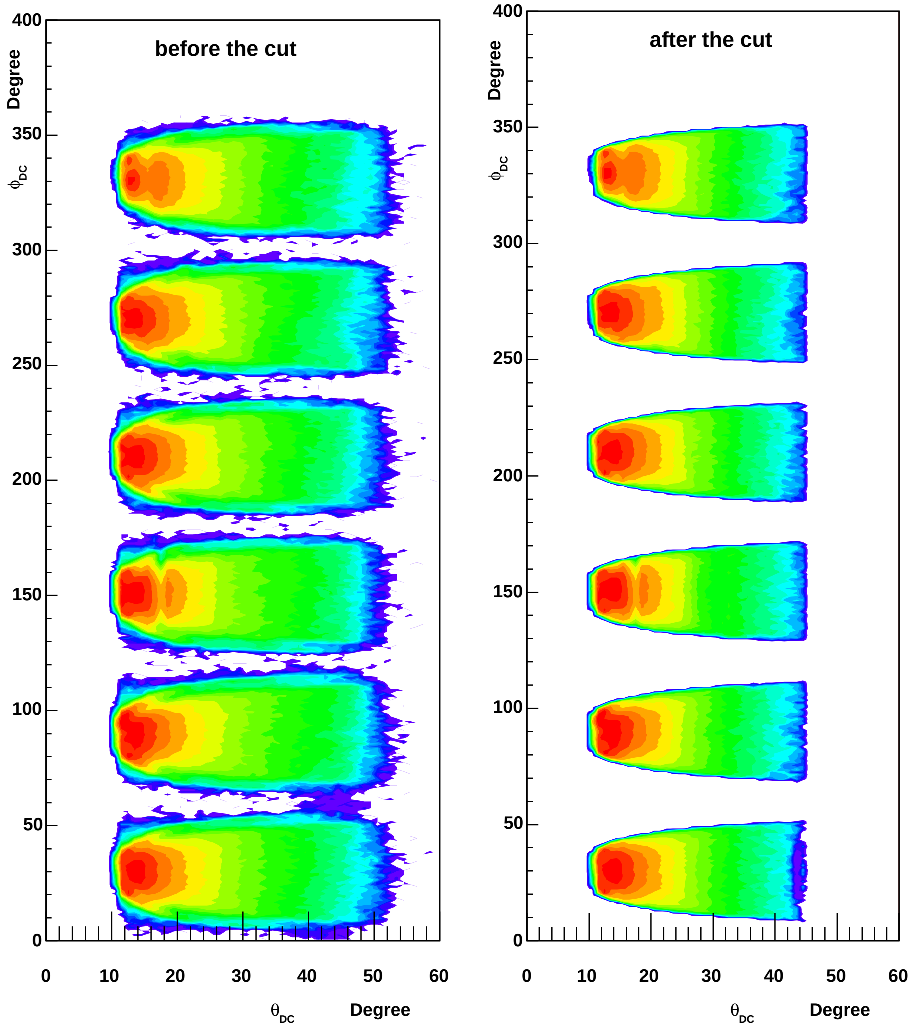

Figure 3.21. ϕ_{DC} vs θ_{DC} before and after the fiducial cut for inbending electrons. The low efficient region is removed by the cut.

Table 3.1. Parameters for the fiducial cut of inbending electrons.

Parameters	A	B	C	D	E	F
Values	25.0	0.15	0.25	9.0	16.72	0.075

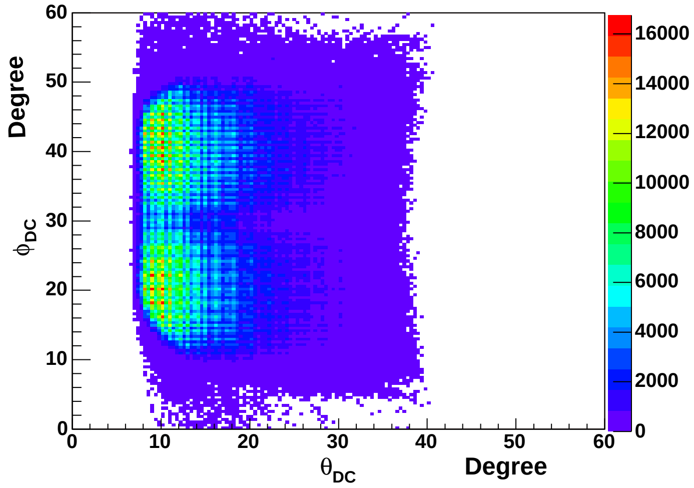

Figure 3.22. The same figure as Fig. 3.19 but for out bending electrons. The inefficient area around 30^o is clearly visible, which is not for inbending electrons.

where

$$\Delta\phi = A'(sin(\theta_{DC} - 6.5))^{expon}, \tag{3.22}$$

$$expon = B'(p_{scaled}/5)^{C'}, \tag{3.23}$$

$$\theta_{cut} = D' + E'(1 - p_{scaled}/5)^{F'}, \tag{3.24}$$

$$\theta_{max} = min(40, \theta_{norm}), \tag{3.25}$$

$$\theta_{norm} = 35[(p\frac{3375}{|I|} + 2.5)\frac{1}{5}]^{\frac{1}{3}} \text{and} p_{scaled} = p\frac{1500}{|I|}. \tag{3.26}$$

To remove the center area of each sector, the following cut is required,

$$\phi_{sec} > 30^o + \phi_{center} \text{ or } \phi_{sec} < 30^o - \phi_{center}, \tag{3.27}$$

and,

$$\phi_{center} = \frac{G'}{sin(\theta_{DC} + H')}. \tag{3.28}$$

Parameters A' through H' are also determined empirically. The values are listed in Table 3.2. Parameters G' and H' are related the sector, then not listed here. An example of the fiducial cuts for outbending electrons in 6 momentum bins is shown in Fig. 3.23

Table 3.2. Parameters for the fiducial cut of inbending electrons.

Parameters	A′	B′	C′	D′	E′	F′
Values	25.0	0.15	1/24	9.0	25.	24

3.8.2 Proton Fiducial Cut

The proton fiducial cut has a similar form as the electron fiducial cut, but it is less restrictive, because the Cerenkov counter is not used to detect protons. Therefore, the low efficient regions for protons are mainly at the edge of the detector and due to the hardware problem, such as broken wires in drift chambers, dead PMTs in Time-Of-Flight counters, etc. The general form for protons are similar to those of inbending electrons, except the θ_{cut} is

$$\theta_{cut} = D + E(1 - p_{scaled}/5)^F. \tag{3.29}$$

θ_{cut} is different because the torus magnet field has smaller effect on the proton. The parameters A through F are also found empirically, and they are listed in the Table 3.3.

As described in Chapter 2, the Helmholtz coils of the target magnet block the particles with polar angle between 45^o to 75^o. Therefore, additional cuts are used to remove protons which scatter off the coils,

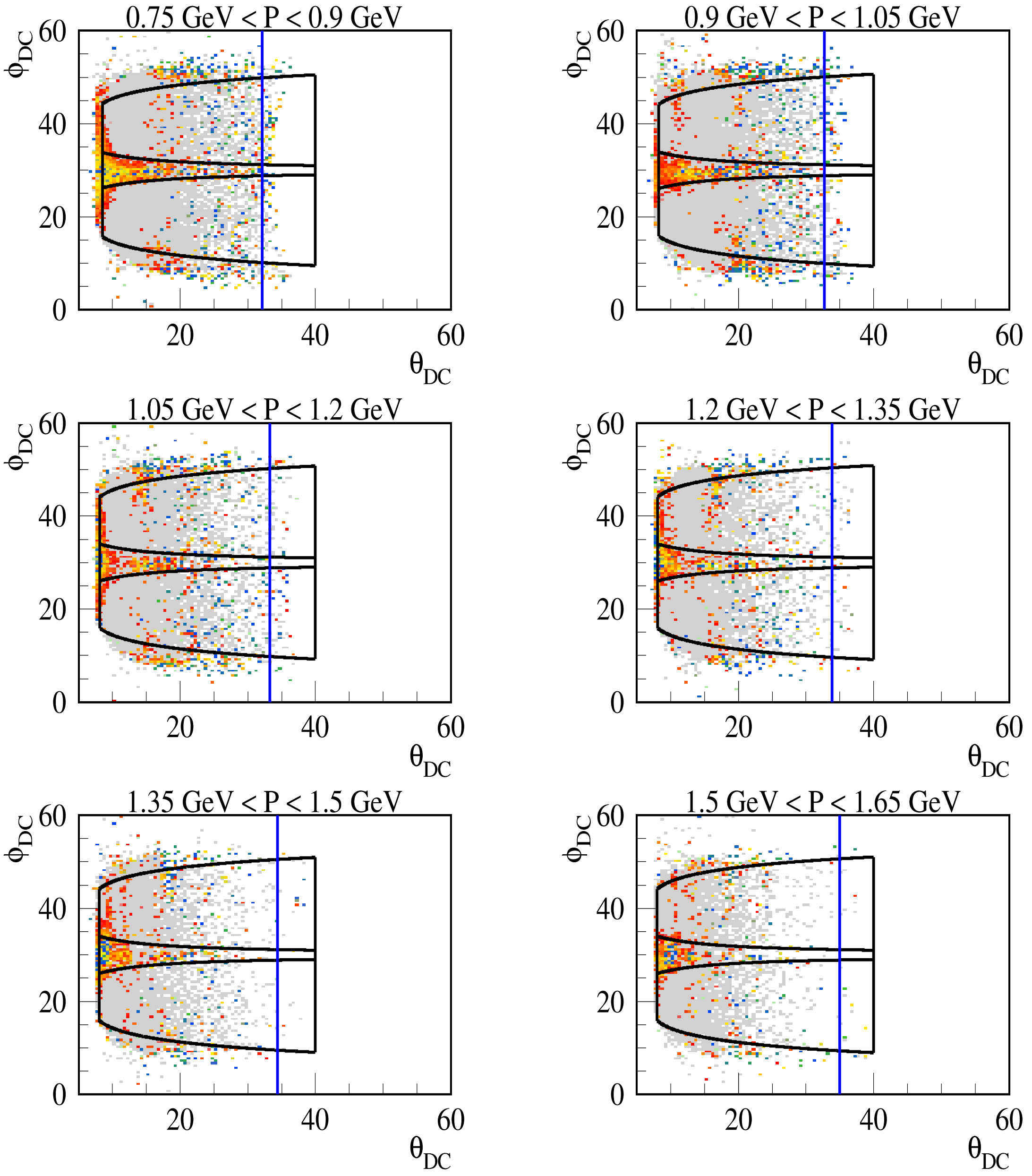

Figure 3.23. The number of photoelectrons distribution on ϕ vs θ plane for outbending electrons in six momentum bins. The gray shaded region represents the area with efficiency greater than 80%. The blue line denotes the maximum polar angle for accepted electrons, and black line denotes the boundary of the appplied cut. The plots is a courtesy of V. Dharmavardane.

Table 3.3. Parameters for the proton fiducial cuts.

Parameters	A	B	C	D	E	F
inbending	28.5	0.15	1/24	9.0	25.0	24.0
outbending	28.5	0.15	0.33	10.0	25.0	24.0

$$\theta_{DC} < 39.5 - \frac{0.223}{p_{scaled} - 0.424} + 15.5 p_{scaled} - 6.1 p_{scaled}^2 \text{forinbendingdata}, \tag{3.30}$$

$$\theta_{DC} < 34.5 - \frac{0.223}{p_{scaled} - 0.424} + 15.5 p_{scaled} - 6.1 p_{scaled}^2 \text{foroutbendingdata}, \tag{3.31}$$

The cut depends on the proton momentum which can be understood as follows. When the charged particles pass through the axial field of the target magnet, they are bended into the beam direction, in other words, the polar angle θ decreases. The magnet field has different effect on charged particles with different momenta, and so magnet field cuts depend on the particle momentum.

The low efficient regions close to the edge of the detector in the θ vs ϕ plane have been removed. However, some additional low efficient regions exist, which are related to hardware problems, such as broken wires in drift chambers, and bad scintillator paddles. These are nearly independent on ϕ, and therefore are studied in θ vs p plane based on sector by sector. The cuts are shown in Fig. 3.24. Fig. 3.25 shows the angular distribution before and after the cut, and it is clear that the low efficient region is removed.

3.8.3 Photon Fiducial Cut

Since the photon trajectory is a straight line, the photon fiducial cut is much easier to define. The photon fiducial region definition is described as follows.

When a photon hit location is close to the calorimeter edges, the shower could leak outside. In this case, the photon energy can not be fully reconstructed. To exclude the calorimeter edge, a safe region is defined which excludes the region that presents low photon rates. Fig. 3.26 shows the fiducial region for photons ($ep \to e'p'\gamma$). $ep \to e'p'\gamma$ events are selected requiring $\theta_{\gamma X} < 1^o$, and $|E_\gamma - E_X| < 0.2\sqrt{E}_\gamma$, where X is expected from the

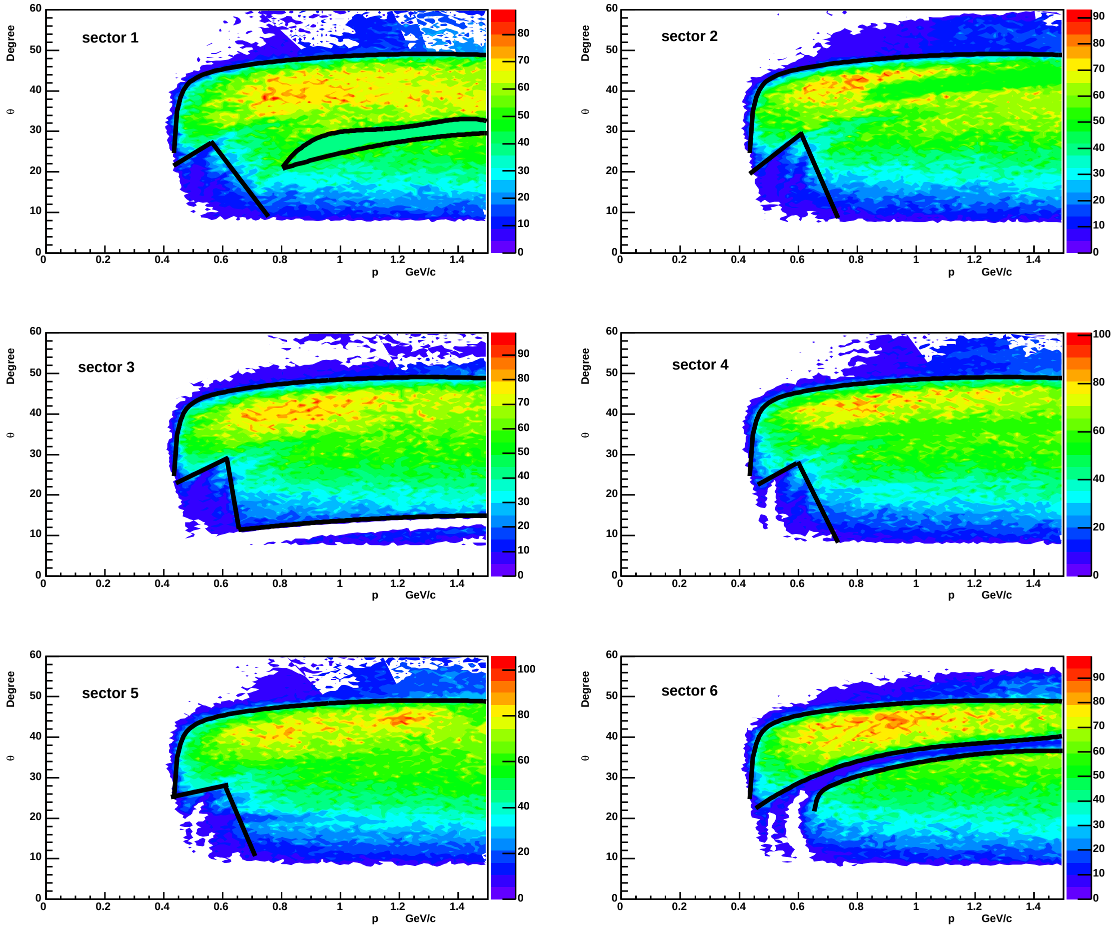

Figure 3.24. θ_{DC} vs p for protons in six sectors. The proton momentum p is scaled to maximum torus current 3375 A by a factor $\frac{3375}{I}$. The black lines show the cuts applied to remove the efficient region.

scattering electron and recoiled proton. With above requirements, photons with energy not fully reconstructed are excluded.

In summary, the event reconstruction procedure was described. The events are triggered by the coincidence of Cerenkov counters and electromagnetic calorimeter signals, which corresponds to one electron ensuring that each event has at least one electron candidate. The start time was reconstructed using the electron's flight time information and beam RF structure. Once the start time was reconstructed, the charged particles were identified using

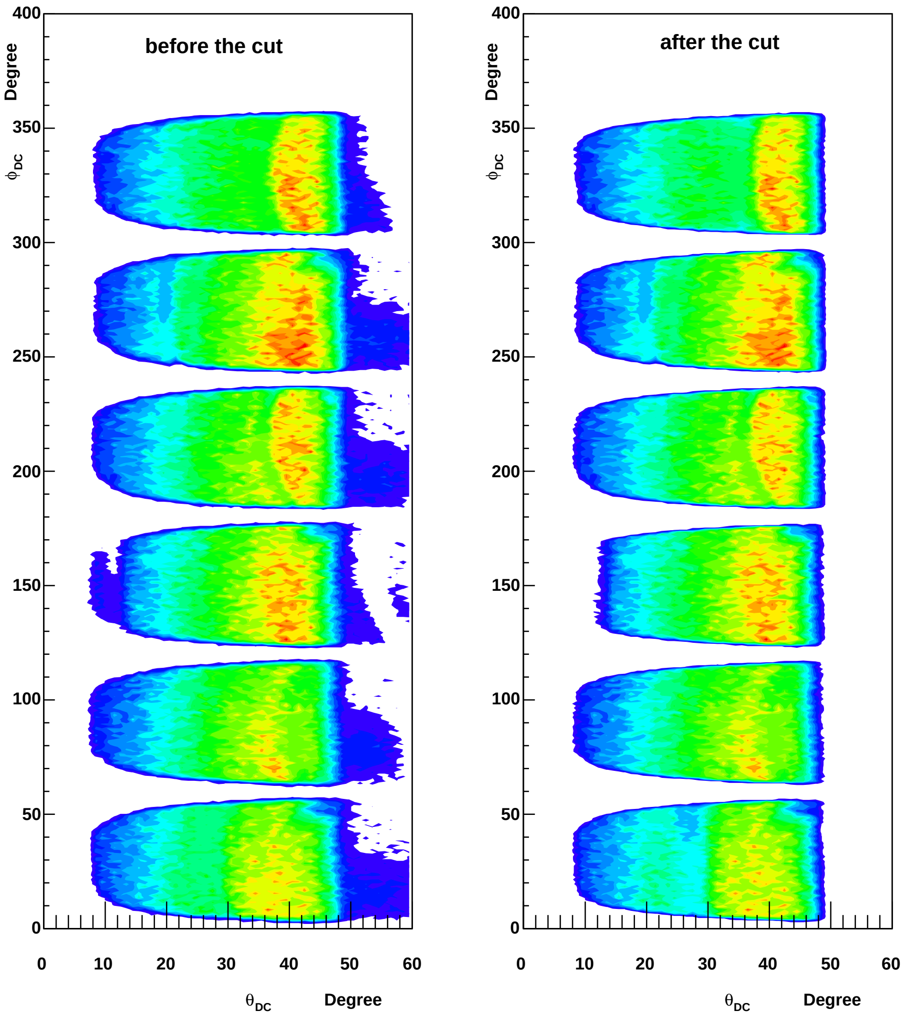

Figure 3.25. ϕ_{DC} vs θ_{DC} before and after the fiducial cut for outbending protons. The low efficient region is removed by the cut.

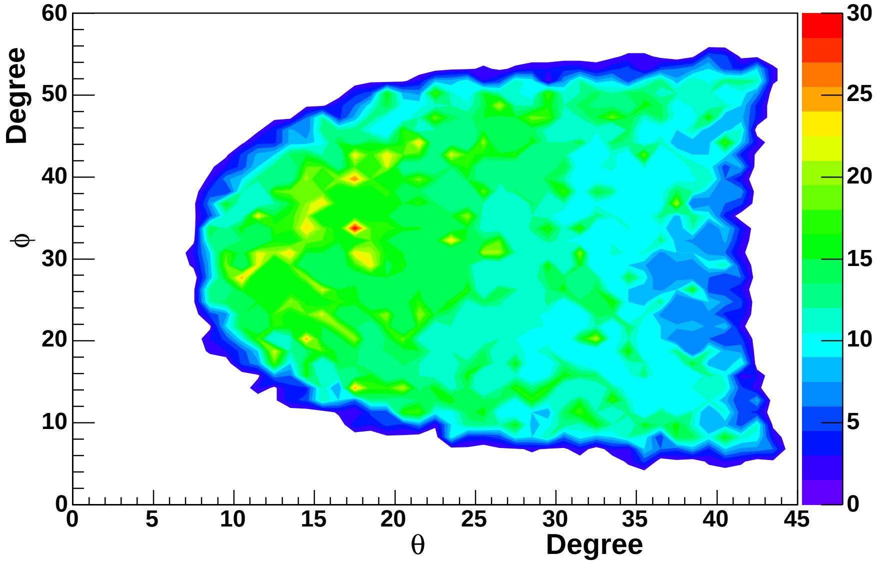

Figure 3.26. Fiducial region for photons.

time of flight. Neutral particles were identified with electromagnetic calorimeter information. After all particles were identified, the electron momentum correction, the proton energy loss correction, and photon energy correction were applied to each event. To decrease the systematic errors due to low efficient region of CLAS detector, only the events in the fiducial region were selected. The remaining events were used in the physics analysis described in later chapters.

CHAPTER 4

CLAS DATA

4.1 Overview

This analysis is based on the data acquired from EG1b run period. These were taken from Sep. 2000 to Apr. 2001. During the run, longitudinally polarized electrons were directed onto a longitudinally polarized solid $^{15}NH_3$, with the beam energies: 1.6 GeV, 2.6 GeV, 4.2 GeV, and 5.7 GeV. The polarization of the electron beam (P_e) was around 70% as measured via a Moller polarimeter. The target[46] polarization was monitored with a NMR system, and the proton polarization ranged from 60% to 80%. In addition to the polarized targets, ^4He,^{12}C and frozen ^{15}N targets were also used to study the dilution due to the unpolarized material in the target.

EG1b experiment was proposed to measure the spin structure of the neutron, and this analysis is a by-product. Therefore, 5.7 GeV electron beam data are utilized. The 5.7 GeV data consists of smaller data sets with different torus current and slightly different beam energies: 5.764 GeV, 5.735 GeV, and 5.627 GeV. In particular, the data information used in this analysis are listed in Table 4.1. Usually, when the torus current is positive, the electron is bended into the beam direction, therefore the recorded data are called inbending data, and when the torus current is negative, on the contrary, the electron is bended away the beam direction, therefore, the recorded data are called outbending data.

During the data taking of the experiment, the detector failed and the DAQ system could crash. To avoid these kinds of data, data quality is checked based on run by run. The target polarization is measured by a NMR system and recorded during the run, however, it is not highly reliable. An alternative measurement is to calculate the product $P_e * P_t$ from the elastic scattering asymmetry, then extract the target polarization (P_t) using the known beam polarization (P_e).

In this chapter, the run selections, the data quality check, and the target polarization calculation are described.

4.2 Quality Check and Run Selection

The terminology "deeply virtual" means high virtulity ($Q^2 > 1\,\mathrm{GeV}^2/\mathrm{c}^2$) and high hadronic mass ($W > 2$ GeV/c^2) to avoid the resonant nucleon states. To satisfy the above requirements, only the data with 5.7 GeV beam energy are used. The summary of data used in this work is shown in Table 4.1.

Table 4.1. Data Summary

Beam Energy	Torus Current	Target	Target Polarity(P_t)
5.628 GeV	2250 A	NH_3	$P_t > 0$
	2250 A	NH_3	$P_t < 0$
	2250 A	^{12}C	
5.736 GeV	2250 A	NH_3	$P_t > 0$
	2250 A	NH_3	$P_t < 0$
	2250 A	^{12}C	
5.736 GeV	-2250 A	NH_3	$P_t > 0$
	-2250 A	NH_3	$P_t < 0$
	-2250 A	^{12}C	
5.764 GeV	-2250 A	NH_3	$P_t > 0$
	-2250 A	NH_3	$P_t < 0$
	-2250 A	^{12}C	

Based on run by run, the data quality is checked to exclude the runs where some part of the CLAS detector was not properly operated. Using bad data runs would result in wrong normalization. Data quality is performed by checking the inclusive electron rates for each sector. When CLAS works normally, the inclusive electron rate is a constant for each run. While, if failure occurs, such as hardware problem on sector 5 of electromagnetic calorimeter, the electron rate for sector 5 would be less than normal. Fig. 4.1 show the inclusive electron rates for 5.6 GeV data.

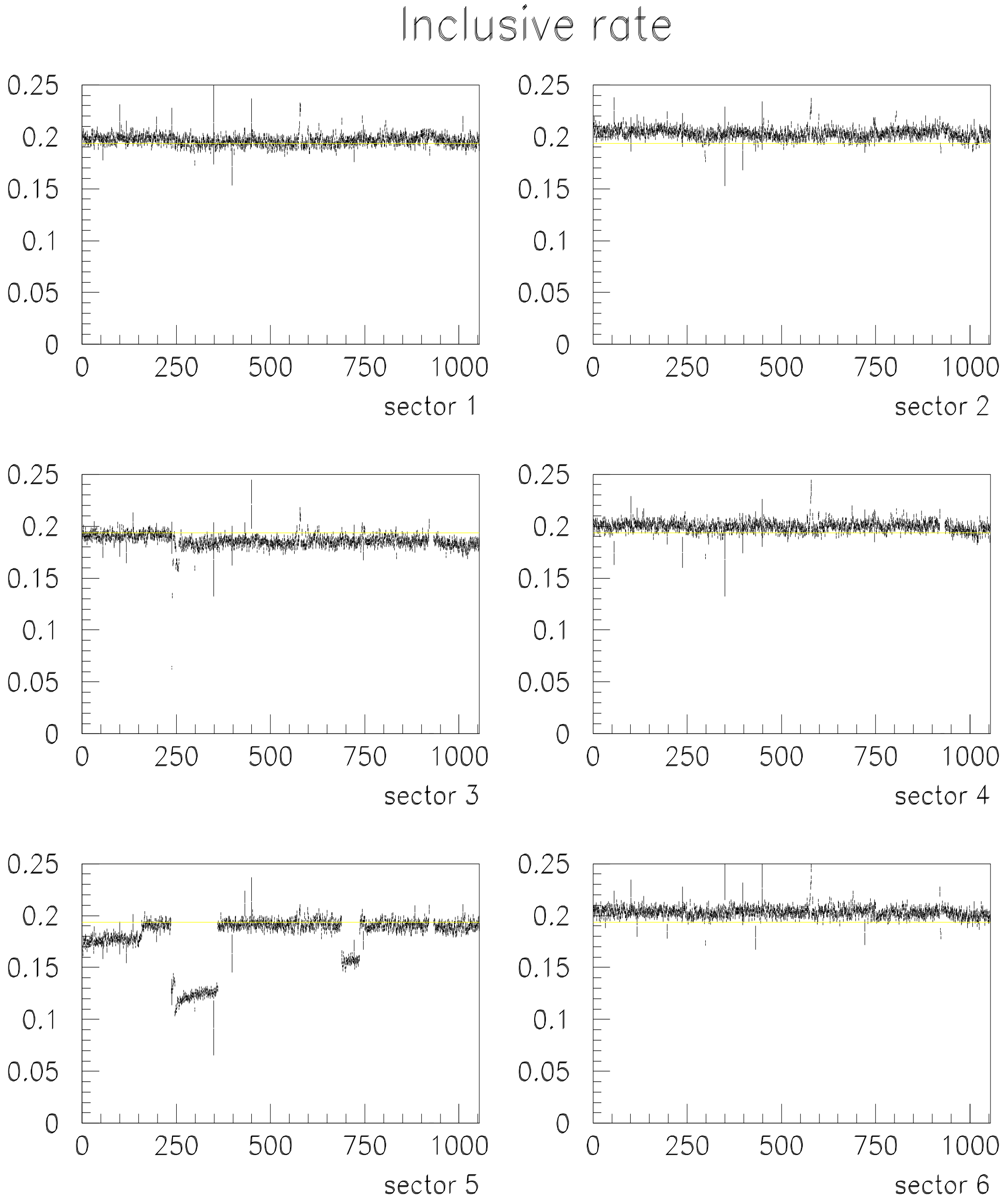

Figure 4.1. The inclusive electron rate as function of the run number for six sectors[47]. In sector 5, some runs show the large deviation from the other runs, therefore, these runs are rejected.

4.3 Target Polarization

To obtain the target spin asymmetry it is necessary to know the target polarization. During data taking, target polarization was measured using the well known NMR system[46]. The NMR coils are positioned outside the target container, therefore, NMR measurement is mostly the polarization of the outer region of the target material. Since the electron beam can depolarize the target material, the polarization of the inner region is always smaller than outer region. In addition, the NMR technique requires the value of the thermal equilibrium resonance peak, introducing additional uncertainties due to the small thermal equilibrium signal peak (proton polarization less than 1%) and to possible non linearites of the NMR system[48]. Fig. 4.2 shows the difference between the target polarization measured with NMR and the calculated polarization. Therefore, this method is unreliable. For this reason, an alternative way is used to extract the target polarization[49, 50]. The known asymmetry for elastic scattering off protons can be used to extract the product of beam and target polarization. The determination of the electron beam polarization is performed via a Moller polarimeter with a very small systematic error. So after $P_e * P_t$ is extracted, P_t can be calculated quickly.

The asymmetry of elastic scattering p(e,e')p can be calculated theoretically.

$$A_{theo} = \frac{2\frac{Q^2}{4M^2}\frac{G_M}{G_E}(\frac{M}{E} + \frac{G_M}{G_E}(\frac{Q^2}{4M^2}\frac{M}{E} + (1 + \frac{Q^2}{4M^2})tan^2(\frac{\theta_e}{2})))}{1 + \frac{Q^2}{4M^2}(\frac{G_E}{G_M})^2\frac{1}{\epsilon}} \tag{4.1}$$

where M is the rest mass of the proton, E is the beam energy, ϵ is

$$\epsilon = (1 + 2(1 + \frac{Q^2}{4M^2})tan^2(\frac{\theta_e}{2}))^{-1} \tag{4.2}$$

and G_E and G_M are the electric and magnetic form factors of the proton, which are given by[51],

$$G_E(Q^2) = \frac{1}{1 + 0.62Q + 0.68Q^2 + 2.80Q^3 + 0.83Q^4}, \tag{4.3}$$

$$G_M(Q^2) = \frac{\mu_p}{1 + 0.35Q + 2.44Q^2 + 0.50Q^3 + 1.04Q^4 + 0.34Q^5}. \tag{4.4}$$

The asymmetry of elastic scattering for a fixed proton polarization ($\Uparrow$) is calculated from

$$A_{meas} = \frac{\frac{N^{\uparrow\Uparrow}}{Q^{\uparrow\Uparrow}} - \frac{N^{\downarrow\Uparrow}}{Q^{\downarrow\Uparrow}}}{\frac{N^{\uparrow\Uparrow}}{Q^{\uparrow\Uparrow}} + \frac{N^{\downarrow\Uparrow}}{Q^{\downarrow\Uparrow}}} \tag{4.5}$$

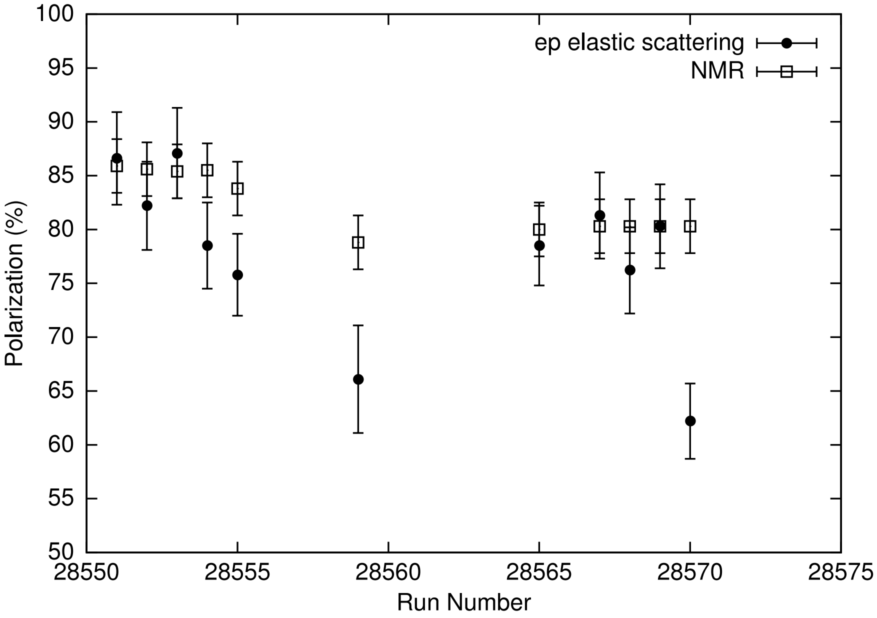

Figure 4.2. Comparison of the proton target polarization measured with NMR and elastic scattering techniques[46]. Clear deviations are shown for some runs. Data are from EG1a which is different with those used in this analysis.

where $N^{\uparrow\Uparrow}$ for example is the number of events with positively polarized beam and positively polarized target, and $Q^{\uparrow\Uparrow}$ for example represent the total luminosity in this configuration.

A_{meas} is related to the physical asymmetry A_{theo} by

$$A_{meas} = P_e * P_t * A_{theo} \tag{4.6}$$

So, the product P_eP_t is immediately determined provided that A_{theo} is known quantity:

$$P_bP_t = \frac{A_{meas}}{A_{theo}} \tag{4.7}$$

Both the inclusive channel p(e,e') and the exclusive channel p(e,e'p') of elastic scattering can be used to extract the asymmetry. The inclusive channel requires that one electron is detected and the corresponding invariant mass is around the rest mass of proton. The advantage of this method is high statistics, while inclusive channels include many events from the nitrogen, therefore, this method is not used in this analysis. In the exclusive channel, the background from the nitrogen can be minimized, and most of events are electrons scattering off the free proton. The exclusive channel requires that both one electron and one proton are detected and their 3-momenta satisfy the elastic relation. The exclusive channel p(e,e'p') of elastic scattering is selected by requiring:

- $|Px(miss)| < 0.07$ GeV/c,
- $|Py(miss)| < 0.07$ GeV/c,
- $|Pz(miss)| < 0.1$ GeV/c,
- $|E(miss)| < 0.1$ GeV,
- $0.85\,\mathrm{GeV/c^2} < W < 1.0\,\mathrm{GeV/c^2}$,
- $178^o < |\phi_e - \phi_p| < 182^o$ (see Fig. 4.3).

Since the target is ammonia, the elastic asymmetry is given by:

$$A_{meas} = \frac{N^{\uparrow\Uparrow} - N^{\downarrow\Uparrow}}{N^{\uparrow\Uparrow} + N^{\downarrow\Uparrow} - background}. \tag{4.8}$$

The product P_e and P_t is extracted for each Q^2 bin, as shown in Fig. 4.4.

In this analysis, $P_e{*}P_t$ values are used from what Peter Bosted extracted for EG1b[52, 53], and they are listed in the table 4.2. The beam polarization $P_e = 0.71 \pm 0.03$ is used to extract the proton target polarization.

The sign of the target polarization is written in the database manually by the experiment operator. During the run, the sign of target polarization is changed several times, it may happen that the operator does not put the right sign. Combining runs which have the wrong target polarization sign would dilute the target spin asymmetry and hence end up with the wrong result. To check for this, the sign of target polarization is checked and compared with the value recorded in the database. The uncorrected electron inclusive asymmetry integrated

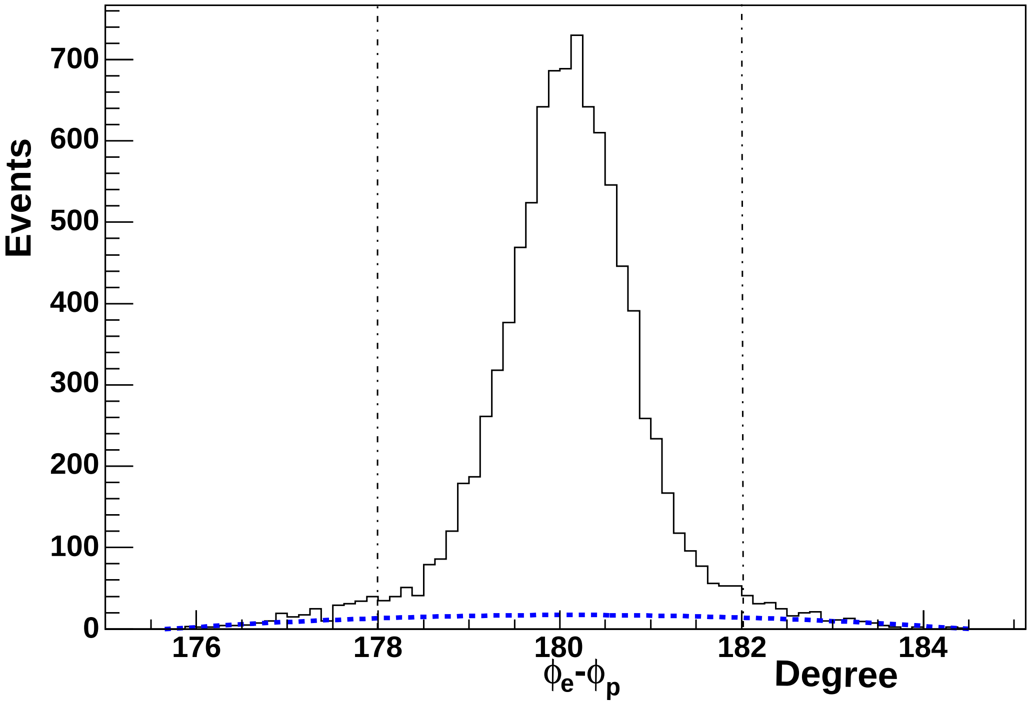

Figure 4.3. The distribution of the azimuthal angle difference between the electron and the proton. Events are selected from elastic region. The blue curve represents the background from the nitrogen, and the dashed lines denote the applied cuts.

in Q^2 and W based on run by run is used to check the target polarization, and the asymmetry is defined as

$$A_u = \frac{N^{\uparrow} - N^{\downarrow}}{N^{\uparrow} + N^{\downarrow}}, \tag{4.9}$$

where $N^{\uparrow}$, for example, is the number of electrons with electron spin parallel to the beam direction.

When the target polarity flips, the sign of the asymmetry is changed. Usually the target polarity is fixed for more than 10 runs, therefore, the asymmetry as function of the run number should be a step function, as shown in Fig. 4.5. The target polarity from the database is compared with the asymmetry sign based on run by run. If there is disagreement, the target polarity from the database would be corrected.

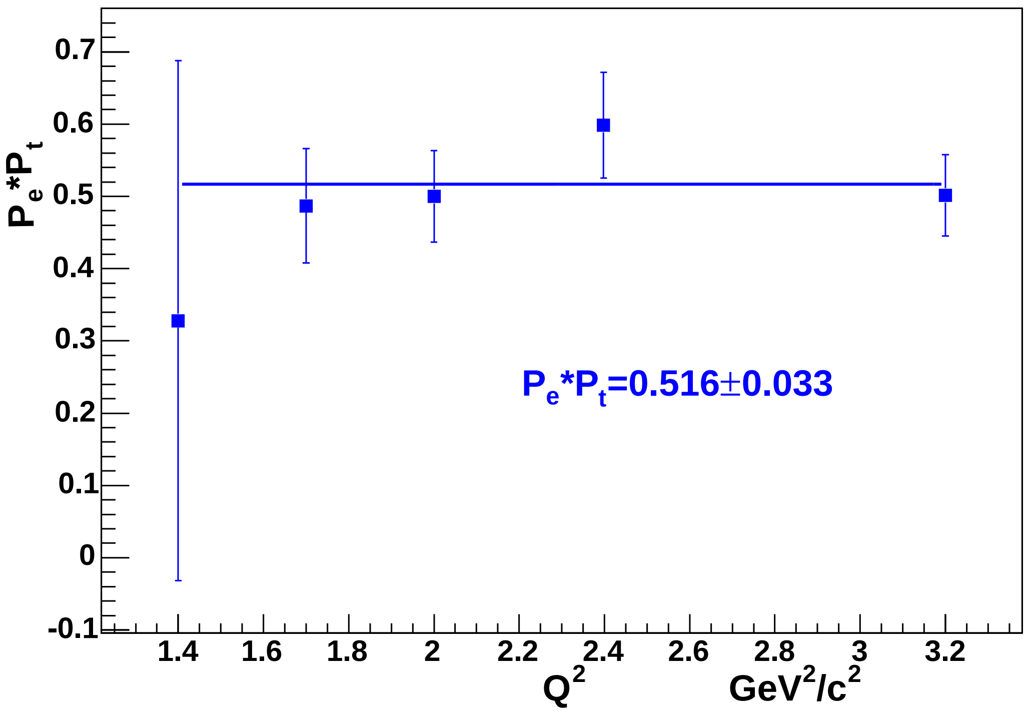

Figure 4.4. The $P_e * P_t$ as a function of Q^2 extracted from ep elastic scattering. The data are from 5.7 GeV inbending data set, and the target is positively polarized.

In summary, general features and data quality are introduced. To reject data that are affected by detector malfunctions, the data quality is checked based on run by run study. Since the target polarization measured using a NMR system is not reliable, the target polarization is extracted from elastic electron scattering.

Table 4.2. Beam and target polarization

data set	target polarity	$P_e * P_t$	P_e	P_t
5.628 inbending	+	0.453 ± 0.026	0.71 ± 0.03	0.638 ± 0.0455
	-	0.575 ± 0.025	0.71 ± 0.03	0.810 ± 0.0501
5.736 inbending	+	0.499 ± 0.022	0.71 ± 0.03	0.703 ± 0.0471
	-	0.481 ± 0.024	0.71 ± 0.03	0.677 ± 0.0465
5.736 outbending	+	0.505 ± 0.029	0.71 ± 0.03	0.711 ± 0.0507
	-	0.535 ± 0.026	0.71 ± 0.03	0.754 ± 0.0485
5.764 outbending	+	0.447 ± 0.025	0.71 ± 0.03	0.630 ± 0.0441
	-	0.470 ± 0.021	0.71 ± 0.03	0.662 ± 0.0407

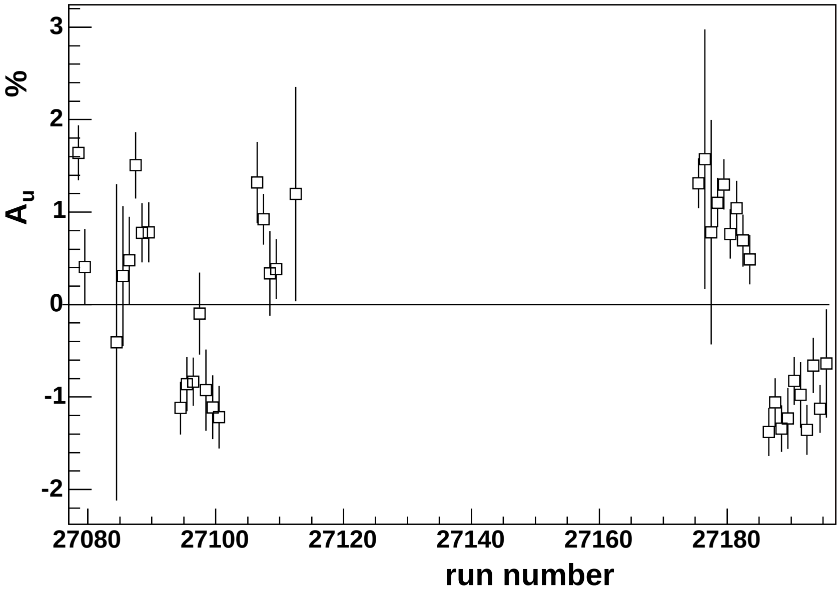

Figure 4.5. The uncorrected inclusive asymmetry vs the run number for 5.7 GeV inbending data. The sign of the asymmetry is changed as the target polarity flips. The runs between 27115 to 27170 correspond to runs with a ND_3 target, which are not used in this analysis.

CHAPTER 5

SINGLE PHOTON ELECTROPRODUCTION

5.1 Overview

The final state of Deeply Virtual Compton Scattering (DVCS) is $ep \rightarrow ep\gamma$, where every particle in the final state is detected in CLAS. The electromagnetic calorimeter acceptance coverage is from 8^o to 45^o and therefore photons can not be detected for scattering angles less than 8^o. Fig. 5.1 shows the distribution of the scattering angle of photons from Monte Carlo simulation. One can see that photons for most DVCS events can not be detected. So it is natural to select $ep \rightarrow epX$ as DVCS candidates where no photons are detected. This method is used in both DVCS analysis of E1c and E1d. In EG1b, Helmholtz coils are used for the polarized target. The Helmholtz coils blocked the protons with polar angles from 48^o to 80^o. This affects significantly DVCS acceptance, see Fig. 5.2. Considering the target is $^{15}NH_3$, in epX events, single photon events from hydrogen are small in numbers compared to the background from nitrogen, see Fig. 5.3. It is therefore not possible to use the same method as that used in DVCS analysis of E1c and E1d. For this reason, only final states with scattered electron, recoiled proton and one detected photon are considered, $e\vec{p} \rightarrow ep\gamma$.

In this chapter, single photon electroproduction will be identified and the target spin asymmetry calculated. In addition, the CLAS detector acceptance affects the normalization of events from different target helicities, the acceptance correction function will be developed and applied based on event by event.

5.2 DVCS Events Selection

The DVCS events are selected requiring that exactly one positive, one negative, and one neutral track are found for a given trigger, and that these track correspond to an electron, a

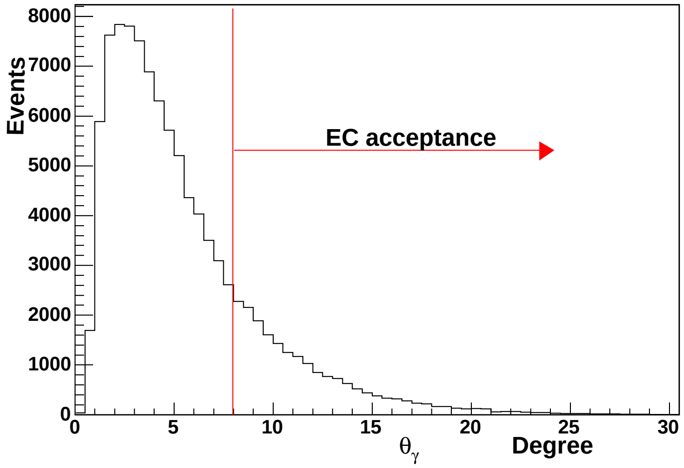

Figure 5.1. DVCS MC photon scattering angle relative to beam direction.

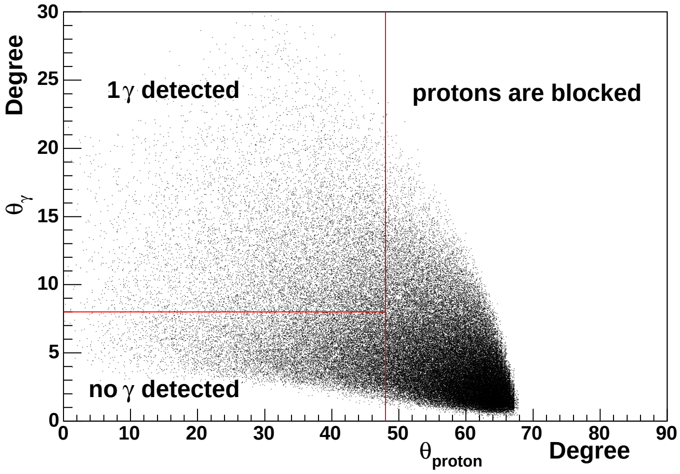

Figure 5.2. Polar angle of the photon vs polar angle of the proton for MC DVCS events.

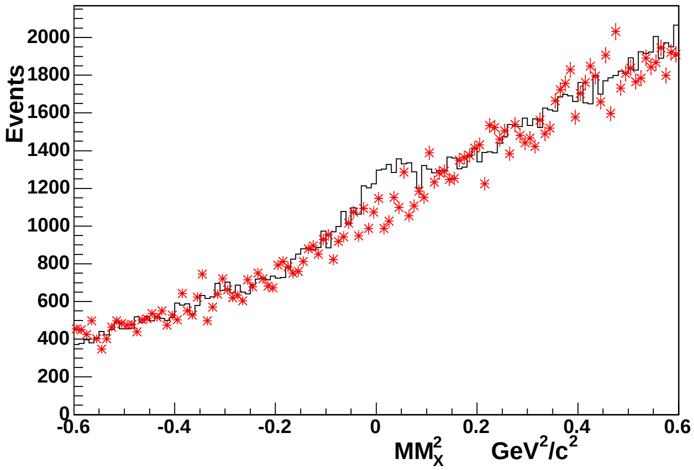

Figure 5.3. MM_X^2 of ep for reaction $ep \to epX$. The black line represent the data from $^{15}NH_3$, red points represent the data from ^{12}C which simulate the background from ^{15}N. They are normalized to each other using the negative tail of the MM_X^2. $W > 2$, $Q^2 > 1$, $-t < 0.6$.

proton and a photon, respectively. Here, all neutrals are assumed to be photons, including neutrons. Further cuts will reject those events where the neutral is not a photon.

In order to select deep inelastic processes and forward production, the following requirements are imposed on the kinematics: $Q^2 > 1\,\mathrm{GeV^2/c^2}$, $W > 2\,\mathrm{GeV/c^2}$, and $-t < 0.6\,\mathrm{GeV^2/c^2}$, where $-Q^2$ is the four momentum squared of the virtual photon, W denotes the photon-proton invariant mass, and $-t$ represents the square of the four-momentum transfer to the target.

With above kinematic cuts, MM_X^2 distribution of ep is given in Fig. 5.3 for both $^{15}NH_3$ and ^{12}C data. ^{12}C data are used to simulate the background from the unpolarized ^{15}N. Fig. 5.3 clearly shows that the $ep\gamma$ events from the target $^{15}NH_3$ are dominated by those from the unpolarized nitrogen. In addition, it may happen that one of the π^0 decay photons escapes detection. Therefore, there is still contamination from π^0 and large background from nitrogens. In order to suppress the nitrogen background and remove the π^0 contamination, the observed detected photon is compared with the one (γ') expected from the detected electron and proton assuming scattering of the electron from a free proton ($\gamma' = e + p - e' - p'$). First the energy is compared, Fig. 5.4 shows the energy difference between γ and γ'. The

DVCS events are selected with a cut on $E_{\gamma'} - E_\gamma < 0.3\sqrt{E_\gamma}$. Besides the energy difference, the angle difference $\theta_{\gamma\gamma'}$ between the detected photon and expected photon is further used to remove the remaining π^0 contamination, see Fig. 5.5.

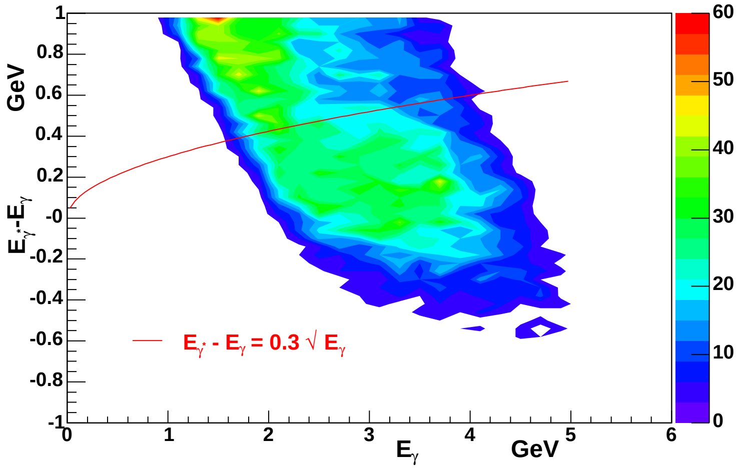

Figure 5.4. The energy difference between calculated photon γ' and detected photon γ. DVCS events are selected with a cut on $E_{\gamma'} - E_\gamma < 0.3\sqrt{E_\gamma}$. $Q^2 > 1$, $W > 2$, and $-t < 0.6$.

Fig. 5.6 shows the missing mass square of ep for reaction $ep \longrightarrow ep\gamma$ after above cuts. To further improve the separation, the data are selected requiring $-0.12\,(\mathrm{GeV/c^2})^2 < MM_X^2 < 0.12\,(\mathrm{GeV/c^2})^2$. After all above selections, not only the π^0 contamination, but also background from ^{15}N are largely suppressed.

In summary, the $\vec{e}\vec{p} \longrightarrow ep\gamma$ events are selected from one detected photon events with following cuts,

- $W > 2$ GeV/c^2
- $Q^2 > 1\,\mathrm{GeV^2/c^2}$
- $-t < 0.6\,\mathrm{GeV^2/c^2}$
- $E_{\gamma'} - E_\gamma < 0.3\sqrt{E_\gamma}\,\mathrm{GeV}$
- $\theta_{\gamma\gamma'} < 2^o$

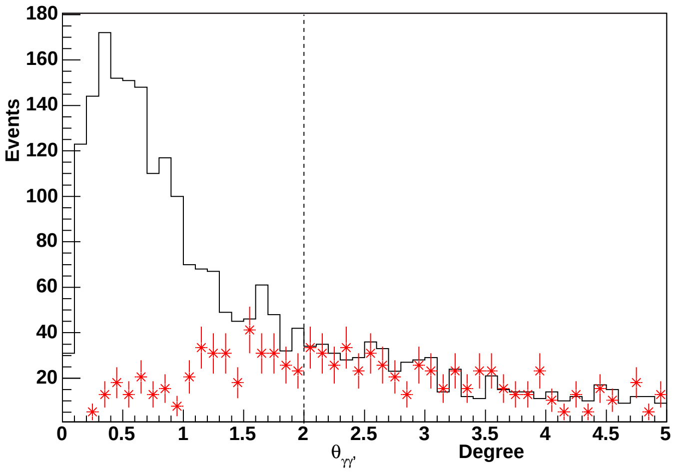

Figure 5.5. The angle difference between detected photon γ and calculated photon γ'. DVCS events are selected requiring $\theta_{\gamma\gamma'} < 2^o$. The black line is from NH$_3$ target, and red stars are from ^{12}C target, normalized to the corresponding NH_3 spectra. $Q^2 > 1$, $W > 2$, $-t < 0.6$, and $E_{\gamma'} - E_\gamma < 0.3\sqrt{E_\gamma}$.

- $-0.12\,(\mathrm{GeV/c^2})^2 < MM_X^2 < 0.12\,(\mathrm{GeV/c^2})^2$ (4 σ width)

As discussed above, a neutral particle is required to select DVCS events. To verify that all events with neutrons are removed, the plot of the deposited energy versus β for photons from the final sample is shown in Fig. 5.7. A clear peak around $\beta = 1$ is visible. This shows that all the neutrals are likely photons.

Since the angular cut ($\theta_{\gamma\gamma'} < 2^o$) and energy difference cut ($E_\gamma - E_{\gamma'} < 0.3\sqrt{E_\gamma}$) can remove photons which hit the edge of the calorimeter where energy can not be fully reconstructed, the photon fiducial cut is not applied for DVCS events. The hit position in the calorimeter is studied for photons from DVCS events (see Fig. 5.8), and it shows that the final samples exclude photons which hit the edge of the calorimeter. Therefore, it is not necessary to apply the photon fiducial cut.

5.3 Dilution Factor

The dilution factor is defined as the ratio between the hydrogen and the full NH$_3$ contribution to the cross section:

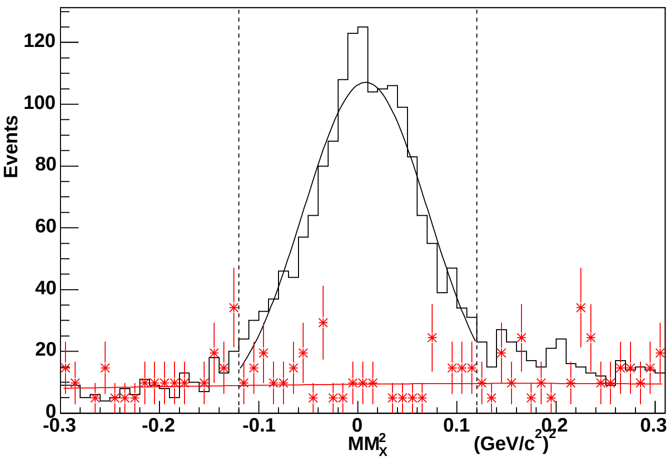

Figure 5.6. Missing mass square of ep for reaction $e\vec{p} \rightarrow ep\gamma$. The black line is from NH_3 target, and red stars are from ^{12}C target, normalized to the corresponding NH_3 spectra. Data are selected requiring MM_X^2 between -0.12 and $0.12\,(\mathrm{GeV/c^2})^2$. $Q^2 > 1$, $W > 2$, $-t < 0.6$, $E_{\gamma'} - E_\gamma < 0.3\sqrt{E_\gamma}$, and $\theta_{\gamma\gamma'} < 2^o$

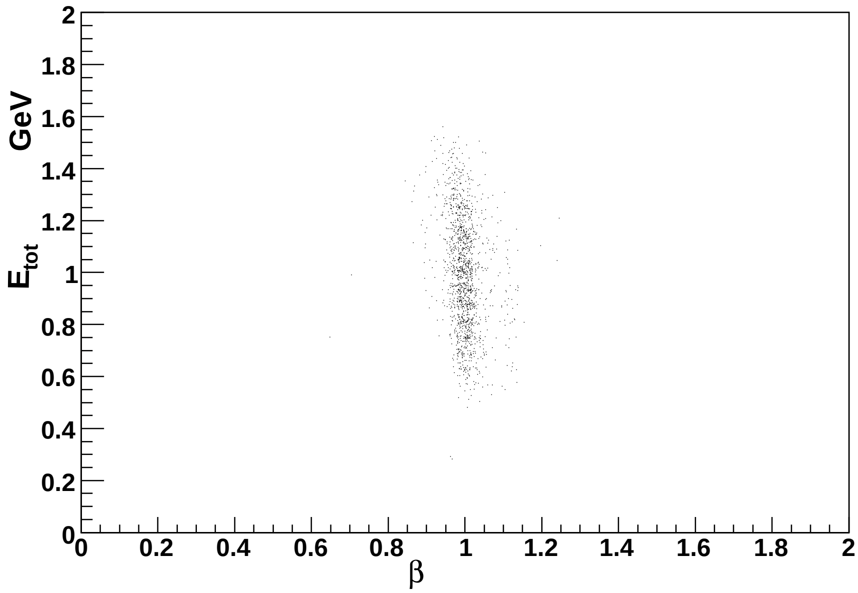

Figure 5.7. Total energy deposited in scintillators (E_{tot}) vs β for photons from DVCS events.

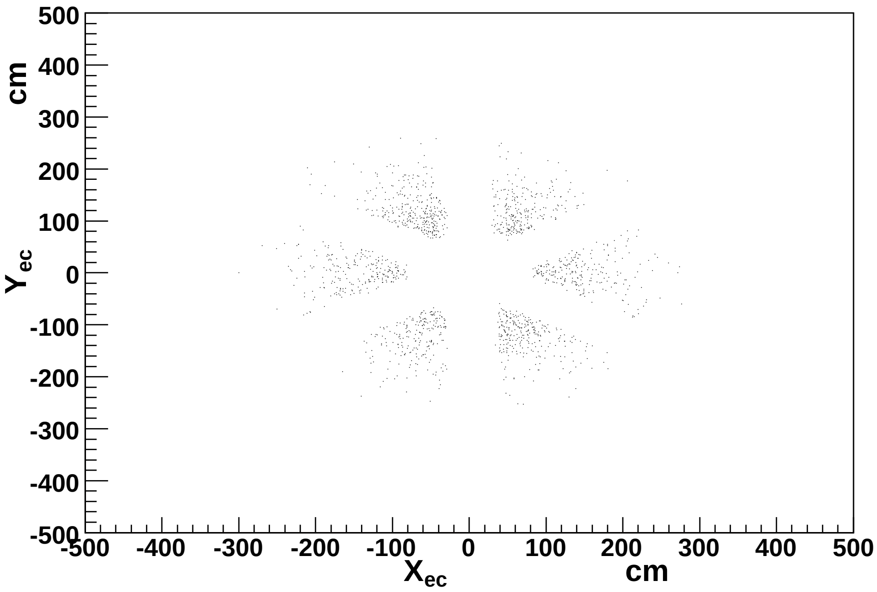

Figure 5.8. Y vs X for the photon hits in the electromagnetic calorimeter. No photons show up at the edge of the calorimeter.

$$f = \frac{3\sigma_{\mathrm{H}}}{\sigma_{\mathrm{NH_3}}} = 1 - \frac{\sigma_{\mathrm{N}}}{\sigma_{\mathrm{NH_3}}} \tag{5.1}$$

The ^{15}N nucleus is almost unpolarized and therefore it does not produce any sizable effect on the numerator of the target spin asymmetry calculation, see Eq.(5.8). However it gives a significant contribution to the denominator of the asymmetry calculation that, as a consequence, is "diluted" by the nitrogen.

To estimate the dilution factor, it was necessary to evaluate the pure nitrogen contribution to the studied reaction. During EG1b, the data on a carbon target were taken to simulate the ^{15}N contribution. The carbon data were normalized to NH_3 data by comparing the negative tails of the missing mass square plots (see Fig. 5.9). The normalization constant $c = 2.575 \pm 0.020$ was measured.

Following the procedure introduced above, the numbers of $ep\gamma$ events from $^{15}NH_3$ and ^{12}C for each ϕ bin are evaluated and used to calculate the dilution factor with Eq.(5.1):

$$f(\phi) = 1 - \frac{c \cdot N_C(\phi)}{N_{NH_3}(\phi)} \tag{5.2}$$

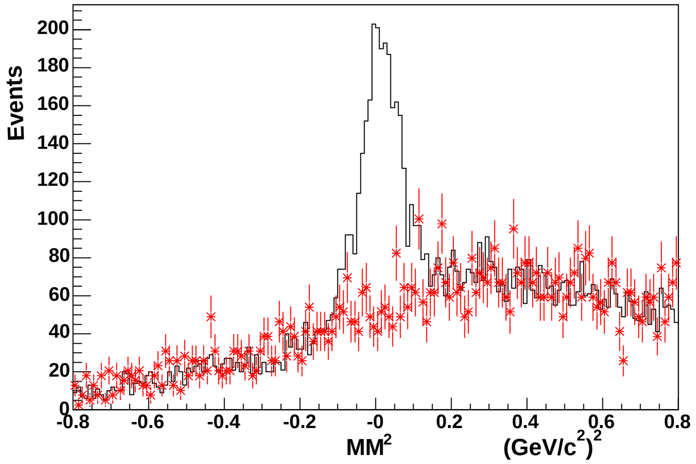

Figure 5.9. Missing Mass Squared distribution of (ep) for reaction $ep \rightarrow ep\gamma$, $Q^2 > 1$, $W > 2$, $E_{\gamma'} - E_\gamma < 0.3\sqrt{E_\gamma}$. Black line denotes ^{15}NH$_3$ target, and red cross denotes ^{12}C target. The carbon data were normalized to the ^{15}NH$_3$ with negative tail of MM_X^2, and the normalization constant c is 2.575 ± 0.020.

where N_C is the number of events from ^{12}C, and $\mathrm{N}_{\mathrm{NH}_3}$ is the number of events from ^{15}NH$_3$. The target spin asymmetry was extracted as a function of ϕ and therefore the dilution factor was evaluated for different ϕ bins. Fig. 5.10 shows the dilution factor for different ϕ, and there is no dependence on ϕ. Therefore, a single dilution factor $f = 0.901 \pm 0.035$ based on the integrated-ϕ was calculated and used in the final analysis.

5.4 Acceptance calculation

The target spin asymmetry is defined in Eq.(5.8). we can see that the target spin asymmetry is the combination of $N^{\Uparrow}$ and $N^{\Downarrow}$. $N^{\Uparrow(\Downarrow)}$ is the detected number from the positively (negatively) polarized target for each ϕ bin. Since the CLAS acceptance does not depend on the target helicity, one may expect that the acceptance cancels out in both numerator and denominator. However, this is true only if the target spin asymmetry is measured for fixed values of Q^2, t, x_B, θ, and ϕ. In this case, the acceptance is constant for different target helicities and cancels out for each bin. While in Eq.(5.8), $N^{\Uparrow(\Downarrow)}$ is integrated over the Q^2, t, x_B, and θ, therefore, the target spin asymmetry is

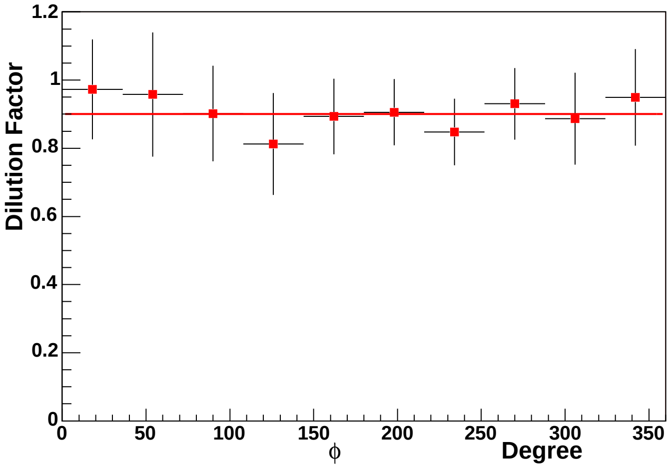

Figure 5.10. The dilution factor as a function of ϕ for reaction $\vec{e}\vec{p} \to ep\gamma$. The solid line represents the average dilution factor $f = 0.901 \pm 0.035$.

$$A_{UL}(\phi) = \frac{\int \sigma_t(Q^2, t, x_B, \theta, \phi)\eta(Q^2, t, x_B, \theta)dQ^2dtdx_Bd\theta}{\int \sigma_0(Q^2, t, x_B, \theta, \phi)\eta(Q^2, t, x_B, \theta)dQ^2dtdx_Bd\theta} \tag{5.3}$$

$$\sigma_t = \sigma^{\Uparrow} - \sigma^{\Downarrow} \tag{5.4}$$

$$\sigma_0 = \sigma^{\Uparrow} + \sigma^{\Downarrow} \tag{5.5}$$

where $\sigma^{\Uparrow}(\Downarrow)$ is the differential cross section for the positively (negatively) polarized target. Since the cross sections can differ, the effect of the acceptance must be taken into account.

The acceptance of CLAS is usually evaluated using MC methods. For complete simulations, MC events should be generated in small bins of (Q^2,t,x_B,θ,ϕ). The total number of MC events required would be on the order of $N_{Q^2} \times N_t \times N_x \times N_\theta \times N_\phi \times N_{events-per-bin}$. For small bins, i.e. large N's, the generation of this large volume of MC events would be a very daunting task. An alternative method is to calculate the acceptance analytically. A method based on fiducial cuts and uniform fiducial regions has been developed and successfully utilized. (see references [54, 55, 56].)

The main idea is as follows: the acceptance within the fiducial regions is calculated, and an event ($ep \to ep\gamma$) identified by the quantities Q^2, t, x_B, θ, ϕ in the center of momentum system has the corresponding quantities in the lab system: electron momentum and polar angle, p_e, θ_e; proton momentum and polar angle, p_p, θ_p; the difference between the electron and proton azimuthal angles, $\Phi_1 \equiv \phi_e - \phi_p$; photon energy and polar angle, E_γ, θ_γ; and the difference between the electron and photon azimuthal angles, $\Phi_2 \equiv \phi_e - \phi_\gamma$. The electron azimuthal angle ϕ_e is on the contrary a free variable. For produced physics events, particles (electrons, protons, photons) can have any azimuthal angle ϕ with the same probability, while for observed events, particles can only show up with 100% acceptance in fiducial area (>80% if a loose fiducial cut is applied). Due to the six sectors in CLAS, it is clear that the particle azimuthal coverage is not 2π. Therefore, the acceptance is the combined azimuthal coverage of three particles divided by 2π. This idea can be expressed in a mathimatical way:

$$\begin{aligned}
&N(Q^2, t, x_B, \theta, \phi) \propto \int \sigma(Q^2, t, x_B, \theta, \phi)\eta(p_e, \theta_e, \phi_e, p_p, \theta_p, \phi_p, E_\gamma, \theta_\gamma, \phi_\gamma)d\phi_e \\
&= \int \sigma(p_e, \theta_e, p_p, \theta_p, E_\gamma, \theta_\gamma, \Phi_1, \Phi_2)\eta(p_e, \theta_e, \phi_e, p_p, \theta_p, \phi_e - \Phi_1, E_\gamma, \theta_\gamma, \phi_e - \Phi_2)d\phi_e \\
&= \sigma(p_e, \theta_e, p_p, \theta_p, E_\gamma, \theta_\gamma, \Phi_1, \Phi_2) \int \eta(p_e, \theta_e, \phi_e, p_p, \theta_p, \phi_e - \Phi_1, E_\gamma, \theta_\gamma, \phi_e - \Phi_2)d\phi_e \\
&= \sigma(Q^2, t, x_B, \theta, \phi) \int \eta(p_e, \theta_e, \phi_e, p_p, \theta_p, \phi_e - \Phi_1, E_\gamma, \theta_\gamma, \phi_e - \Phi_2)d\phi_e \qquad (5.6)
\end{aligned}$$

The last integral is the acceptance function for $ep \rightarrow e'p'\gamma$, which is also the correction factor we are looking for:

$$\begin{aligned}
&\eta_{tot}(Q^2, t, x_B, \theta, \phi) = \eta(p_e, \theta_e, p_p, \theta_p, E_\gamma, \theta_\gamma, \Phi_1, \Phi_2) \\
&= \int \eta(p_e, \theta_e, \phi_e, p_p, \theta_p, \phi_e - \Phi_1, E_\gamma, \theta_\gamma, \phi_e - \Phi_2)d\phi_e \\
&= \int \eta_e(p_e, \theta_e, \phi_e)\eta_p(p_p, \theta_p, \phi_e - \Phi_1)\eta_\gamma(E_\gamma, \theta_\gamma, \phi_e - \Phi_2)d\phi_e \qquad (5.7)
\end{aligned}$$

Therefore, acceptance is corrected by applying the function $\frac{1}{\eta_{tot}}$ event by event.

In Eq.(5.7), η_e, η_p, and η_γ are acceptance functions for the electron, the proton, and the photon, respectively. They are step functions, which are unity inside the fiducial area and zero outside.

To verify the correctness of the analytic procedure, the calculation are compared with Monte Carlo for fixed values of ($Q^2 = 2.0GeV^2/c^2$, $-t = 0.5GeV^2/c^2$, $x_B = 0.3$, $\theta = 21^o$), the results of MC comparison are shown in Fig. 5.11.

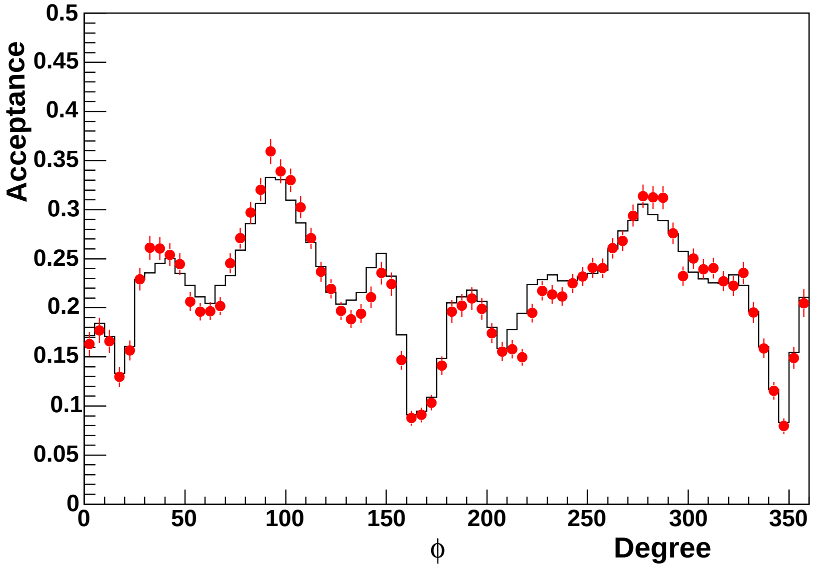

Figure 5.11. Comparison between the results of the analytical calculation (solid line) and the Monte Carlo (red points). Events are generated with fixed values $Q^2 = 2.0\,\mathrm{GeV}^2/\mathrm{c}^2$, $-t = 0.5\,\mathrm{GeV}^2/\mathrm{c}^2$, $x_B = 0.3$, and $\theta = 21^o$. Since the fiducial cut is loose (requiring acceptance greater than 80%), the analytical calculation is scaled by factor 0.712, so that the comparison agrees well.

5.5 Target Spin Asymmetry

The target spin asymmetry is defined in the following equation:

$$A_{UL}(\phi) = \frac{\frac{N^{\Uparrow}(\phi)}{Q^{\Uparrow}} - \frac{N^{\Downarrow}(\phi)}{Q^{\Downarrow}}}{f(P_t^{\Downarrow}\frac{N^{\Uparrow}(\phi)}{Q^{\Uparrow}} + P_t^{\Uparrow}\frac{N^{\Downarrow}(\phi)}{Q^{\Downarrow}})} \tag{5.8}$$

In Eq.(5.8), U denotes the unpolarized beam, L denotes the longitudinally polarized target, $N^{\Uparrow}$ is the extracted number of $ep\gamma$ events with proton spin anti-parallel to the electron beam direction (positive helicity), $N^{\Downarrow}$ is the extracted number of $ep\gamma$ events with proton spin parallel to the electron beam direction (negative helicity), f is the dilution factor, which was introduced in Section 5.3, $Q^{\Uparrow(\Downarrow)}$ is accumulated charge at positive(negative) target helicity, $P_t^{\Uparrow(\Downarrow)}$ means the target polarization for runs with positive(negative) target helicity.

Following the above procedures, both $N^{\Uparrow}$ and $N^{\Downarrow}$ are extracted within 10 ϕ bins for each data set (see Appendix A).

The target spin asymmetry as a function of azimuthal angle ϕ is calculated using Eq.(5.8) for each data set (see Appendix B). Two inbending data sets have only slightly different beam energies, therefore, the target spin asymmetry from inbending data sets is combined together safely using Eq.(5.9) and Eq.(5.10)(see Fig. 5.12). For the same reason, the target spin asymmetry can also be combined together directly using Eq.(5.9) and Eq.(5.10) (see Fig. 5.13). The asymmetries have been corrected for acceptance effects, and should be independent of the acceptance. In addition, the difference in kinematics for inbending and outbending data are much smaller than the bin sizes, and the asymmetry does not vary rapidly with Q^2, x_B, t. So, combining two asymmetries from inbending and outbending data is fine as long as the bin average is calculated correctly. Finally, two sets of data are combined together using Eq.(5.9) and Eq.(5.10), and Fig. 5.14 shows the target spin asymmetry as a function of azimuthal angle ϕ from the combined data sets. In Fig. 5.14, the target spin asymmetry is fitted with function $F = p_0 sin\phi + p_1 sin2\phi$, with $p_0 = 0.240 \pm 0.042$ and $p_1 = -0.087 \pm 0.045$. The errors are only statistical. Fig. 5.15 shows the kinematic coverage for all of the DVCS events.

$$A_{UL}(\phi) = A_1(\phi)\frac{N_1(\phi)}{N_1(\phi)+N_2(\phi)} + A_2(\phi)\frac{N_2(\phi)}{N_1(\phi)+N_2(\phi)}, \tag{5.9}$$

and final statistical error for each ϕ bin is given by

$$\epsilon(\phi) = \sqrt{\epsilon_1^2(\phi)[\frac{N_1(\phi)}{N_1(\phi)+N_2(\phi)}]^2 + \epsilon_2^2(\phi)[\frac{N_2(\phi)}{N_1(\phi)+N_2(\phi)}]^2}, \tag{5.10}$$

where $A_{1(2)}$, $\epsilon_{1(2)}$, $N_{1(2)}$ are the target spin asymmetry, statistical error, and the event number from inbending (outbending) data set, respectively.

5.6 π^0 contamination

Due to the finite spatial resolution of the electromagnetic calorimeter, high energy π^0 events can be misidentified as single photons. High energy π^0 decay into two photons which both hit the calorimeter at nearly the same position and are often mistakenly reconstructed as a single high energy photon. At the same time, the above cuts can not remove all

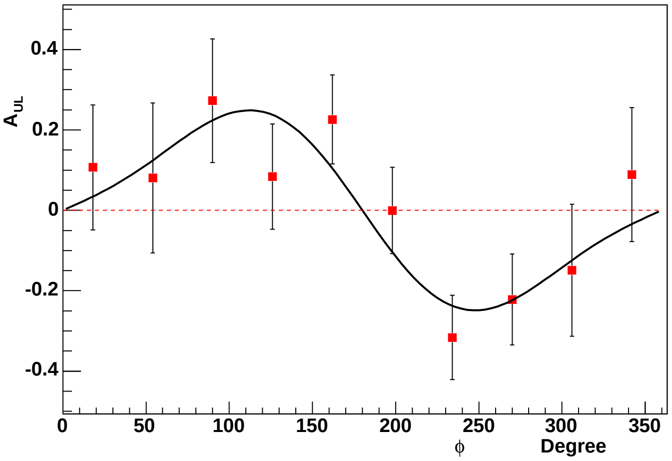

Figure 5.12. The target spin asymmetry A_{UL} for single photon observed events as a function of the azimuthal angle ϕ from inbending data. Points are fitted with function $F = p_0 sin\phi + p_1 sin2\phi$, and $p_0 = 0.224 \pm 0.062$, $p_1 = -0.060 \pm 0.062$. $< Q^2 >= 1.85$, $< -t >= 0.27$, and $< x_B >= 0.28$.

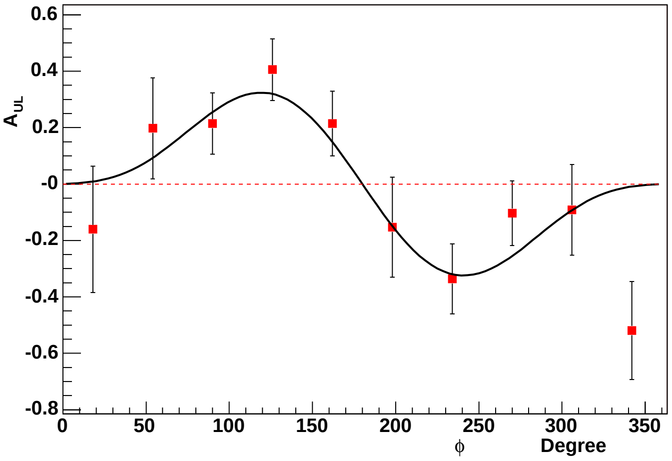

Figure 5.13. The target spin asymmetry for single photon observed events from outbending data. Points are fitted with function $F = p_0 sin\phi + p_1 sin2\phi$, and $p_0 = 0.255 \pm 0.058$, $p_1 = -0.119 \pm 0.065$. $< Q^2 >= 1.87$, $< -t >= 0.31$, and $< x_B >= 0.29$.

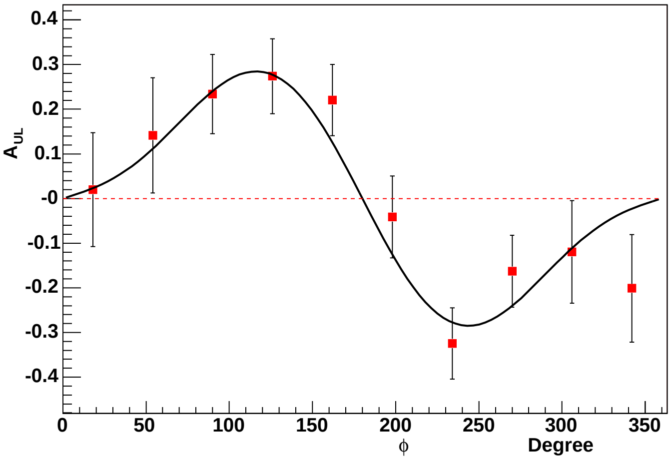

Figure 5.14. The target spin asymmetry for single photon observed events from all of data. Points are fitted with function $F = p_0 sin\phi + p_1 sin2\phi$, and $p_0 = 0.240 \pm 0.042$, $p_1 = -0.087 \pm 0.045$. $< Q^2 >= 1.82$, $< -t >= 0.28$, and $< x_B >= 0.28$.

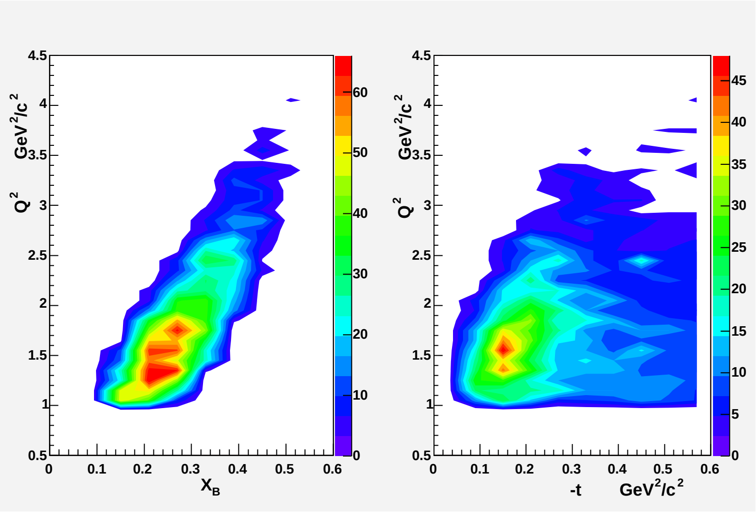

Figure 5.15. Kinematic coverage for all of single photon observed events

of the π^0 events if one of the decay photons escapes detection and carries small part of energy. Consequently, the current event sample is contaminated by such π^0 events. Fig. 5.16 gives the missing mass square of ep after nitrogen background subtraction. Due to the π^0 contamination, the centroid of MM_X^2 spectrum is above 0.

This contamination will be estimated using Monte Carlo(MC) simulations. To correct the π^0 contaminations for DVCS, the target spin asymmetry for π^0 will also be measured using events with a clearly defined single π^0 in the final states, as described in the next chapter.

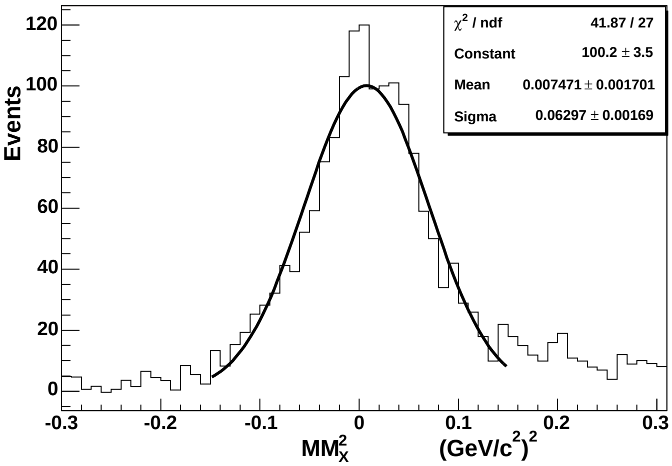

Figure 5.16. Missing mass square of ep for reaction $e\vec{p} \to ep\gamma$ with the nitrogen background subtraction. The nitrogen background is shown in Fig. 5.6 as red stars.

In summary, the single photon electroproduction is identified, and the target spin asymmetry as a function of ϕ is measured. Due to the NH_3 target, a few events from unpolarized nitrogen are in the final events sample, therefore, the dilution factor is calculated and taken into account in the asymmetry. Since the electromagnetic calorimeter has a finite spatial resolution, the final events sample is contaminated by π^0 events. The fraction of the π^0 background will be studied using MC simulations in the Chapter 7.

CHAPTER 6

EXCLUSIVE π^0 ELECTROPRODUCTION

6.1 Overview

Due to the resolution of the electromagnetic calorimeter and asymmetric π^0 decays where one photon escapes detection, there are π^0 events left among the single photon observed events. Therefore, the target spin asymmetry for the single photon observed events need to be corrected for this contamination. It is necessary to extract the target spin asymmetry of π^0 in the same kinematic area ($-t < 0.6\,\mathrm{GeV/c}$, $W > 2$ GeV/c^2, $Q^2 > 1\,\mathrm{GeV}^2/\mathrm{c}^2$). Meanwhile, the π^0 event samples are studied using Monte Carlo simulation to estimate the fraction of π^0 in observed single photon events.

6.2 π^0 Selection

The π^0 event candidates are selected with the requirements that exactly one positive, one negative and two neutral tracks are found for a given trigger, and the particle identifications for these tracks correspond to an electron, a proton and two photons respectively. However, the two detected photons are not always from π^0 decay. In order to remove this kind of event where two photons are not from π^0 decay, the invariant mass of the two photon system is studied, (Fig. 6.1), and π^0 are selected with a cut on invariant mass of two photons from 0.05 GeV/c^2 to 0.18 GeV/c^2. In Fig. 6.1, there is a second peak around 0.075 GeV/c^2 which also corresponds the π^0 events. The shift from the π^0 mass (0.135 GeV/c^2) is because the photon's energy is not fully reconstructed. To verify that they are really π^0 events, a MC simulation is performed. In Fig. 6.2 and Fig. 6.3, MC results show the similar π^0 distributions, therefore, verifying that the second data peak corresponds π^0 events.

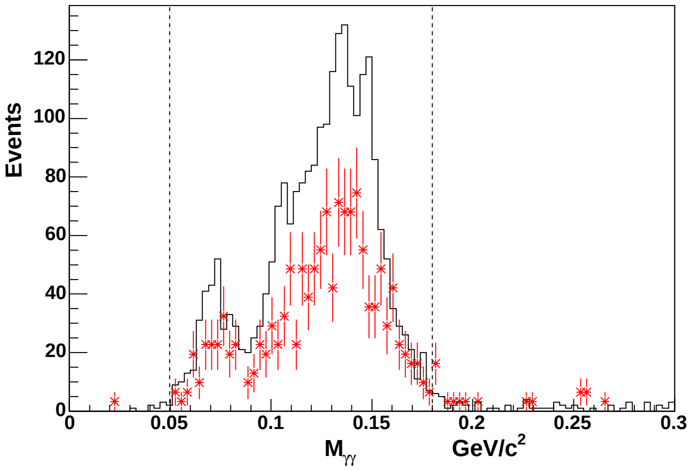

Figure 6.1. Invariant mass of the two photon system. π^0 are selected with cut on invariant mass of two photons from 0.05 GeV/c^2 to 0.18 GeV/c^2. Black line corresponds to NH_3 target, while red stars correspond to C target, normalized to the corresponding NH_3 spectra.

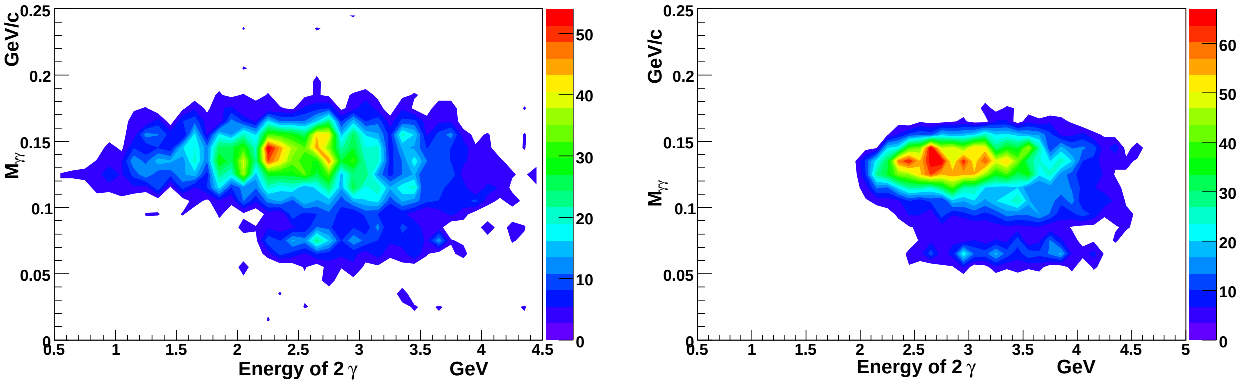

Figure 6.2. Invariant mass of two photons vs the energy of two photons for $ep \rightarrow ep\gamma\gamma$ ($W > 2$, $Q^2 > 1$) for the data (left plot) and MC simulations (right plot). The MC simulation also gives a second peak around $M_{\gamma\gamma}$=0.06 GeV/c^2.

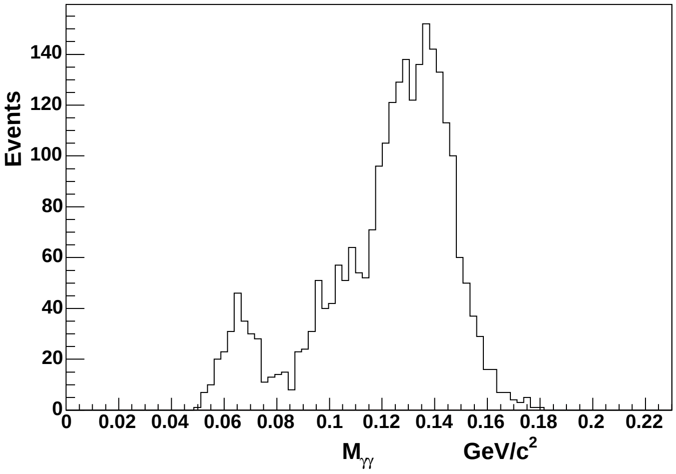

Figure 6.3. Invariant mass of two photons for $ep \to ep\gamma\gamma$ ($W > 2$, $Q^2 > 1$) for MC simulations. The second π^0 peak around 0.06 GeV/c^2 shows up as in the data.

Since the target is NH_3, the final states $ep\pi^0$ are not only from polarized hydrogen, but also from unpolarized nitrogen. Actually, most of events are from nitrogen. In order to suppress the events from nitrogen, the detected π^0 kinematics ($P_{\pi^0} = k_1 + k_2$) and calculated π^0 kinematics ($P_{\pi^0} = q + P_p - P'_p$) are compared, where k_1 and k_2 are four-momenta of the two real photons, and q, P_p and P'_p are the four-momenta of the virtual photon, the target proton and the recoiled proton. Due to the Fermi motion of protons in nitrogen, the detected π^0 kinematics is very different from the calculated π^0 kinematics for most nitrogen events (see Fig. 6.4). Considering the electromagnetic calorimeter resolution, the π^0 events are selected with a missing energy cut on $E_X < 0.3\sqrt{E_{\pi^0}}\,GeV$ for $ep\gamma\gamma X$ events. Besides the missing energy, the angle difference between the detected π^0 ($\gamma\gamma$) and calculated π^0 ($ep \to epX$) is also used to remove not only the events from the unpolarized nitrogen, but also radiative events. The π^0 events are selected with a cut on $\theta_{\pi^0 X} < 2.5^o$, Fig. 6.5.

The final cut is on the missing mass square of (ep) for reaction $ep \to ep\gamma\gamma$, Fig. 6.6. Fig. 6.7 shows the spectrum of the missing mass square of (ep) for reaction $ep \to ep\gamma\gamma$ after nitrogen background subtraction.

In summary, the $e\vec{p} \to ep\pi^0$ are selected from two detected photon events with the following cuts,

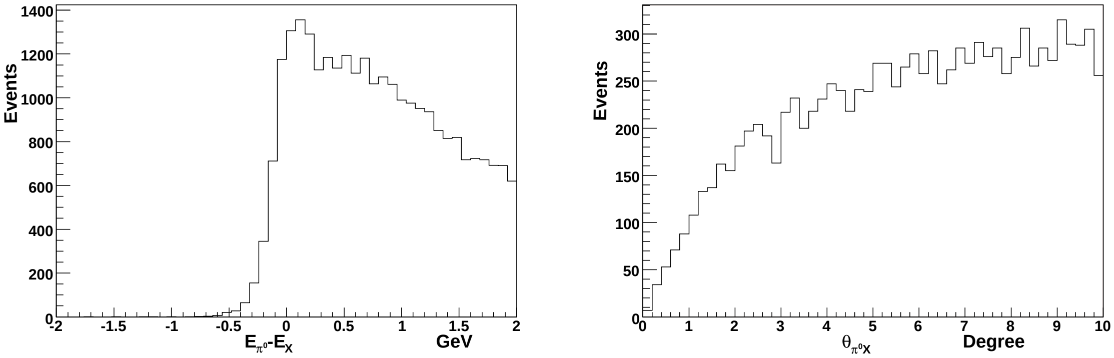

Figure 6.4. The energy difference (left plot) and the angle (right plot) between the detected π^0 and the calculated π^0(X). The events are $ep \rightarrow ep\pi^0$ from the carbon data which simulates the nitrogen background. The π^0 is reconstructed with two detected photons, while X is expected with the recoiled proton and the scattering electron.

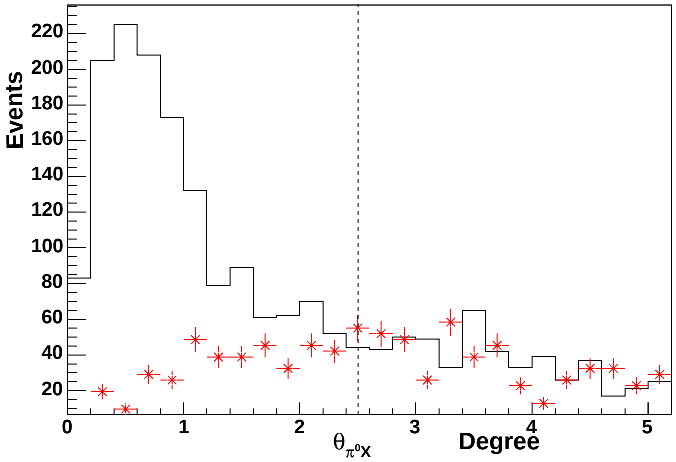

Figure 6.5. The angle difference between detected π^0 ($\gamma\gamma$) and calculated π^0 ($ep \rightarrow epX$) after cuts $W > 2$, $Q^2 > 1$, $0.05 < M_{\gamma\gamma} < 0.18$, $|MM_X^2| < 0.2$, and missing energy $E_X(ep\gamma\gamma X)$ $< 0.3\sqrt{E_{\pi^0}}$, and the π^0 are selected with cut on $\theta_{\pi^0 X} < 2.5^o$. Black line corresponds to NH_3 target, while red stars correspond to C target, normalized to the corresponding NH_3 spectra.

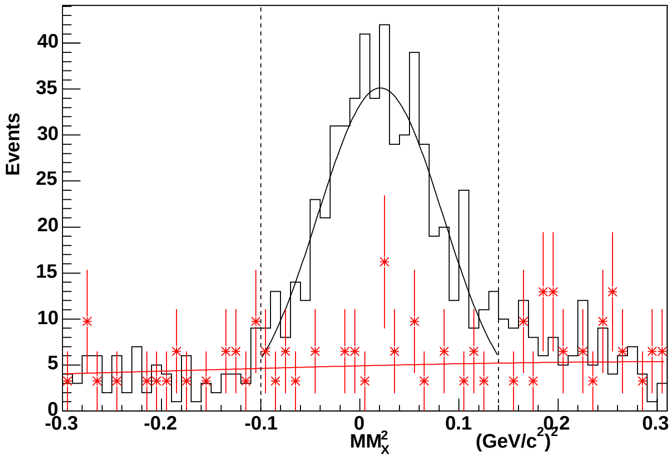

Figure 6.6. Missing mass square of (ep) for reaction $ep \to ep\gamma\gamma$ after cuts $W > 2$, $Q^2 > 1$, $0.05 < M_{\gamma\gamma} < 0.18$, missing energy $E_X(ep\gamma\gamma X) < 0.3\sqrt{E_{\pi^0}}$, and $\theta_{\pi^0 X} < 2.5^o$, and the π^0 are selected with cut on $-0.1 < MM^2_X < 0.14$. Black line corresponds to NH_3 target, while red stars correspond to C target, normalized to the negative tail of NH_3 spectra.

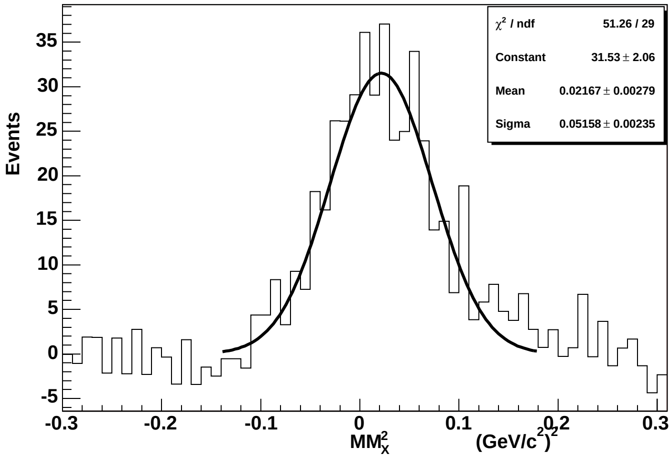

Figure 6.7. Missing mass square of (ep) for reaction $ep \to ep\gamma\gamma$ after nitrogen background subtraction. The nitrogen background is shown in Fig. 6.6 as red stars.

- $W > 2$ GeV/c^2
- $Q^2 > 1\,\mathrm{GeV}^2/\mathrm{c}^2$
- $0.05\,\mathrm{GeV/c}^2 < M_{\gamma\gamma} < 0.18\,\mathrm{GeV/c}^2$
- $E_X(ep\gamma\gamma X) < 0.3\sqrt{E_{\pi^0}}$ GeV
- $\theta_{\pi^0 X} < 2.5^o$
- $-0.1\,(\mathrm{GeV/c}^2)^2 < MM_X^2 < 0.14\,(\mathrm{GeV/c}^2)^2$
- $-t < 0.6\,\mathrm{GeV}^2/\mathrm{c}^2$

All of the above plots give the spectra of C target, which is normalized to NH$_3$ target with the negative tail of MM_X^2, see Fig. 6.8. The normalization constant is $c = 3.241 \pm 0.021$.

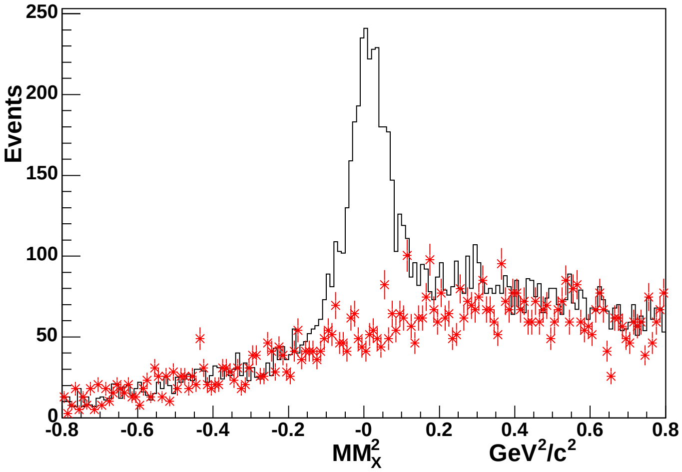

Figure 6.8. Missing mass square of (ep) for reaction $ep \to ep\gamma\gamma$ after cuts $W > 2$, $Q^2 > 1$, and missing energy $E_X(ep\gamma\gamma X) < 0.3\sqrt{E_\pi^0}$. Black line corresponds to the NH$_3$ data, while red stars correspond to the C data, normalized to NH$_3$ spectra with negative tail of MM_X^2. The normalization constant $c = 3.241 \pm 0.021$.

6.3 Dilution Factor

It is necessary to evaluate the dilution factor which will be used in the asymmetry calculation. The final dilution factor was obtained selecting $ep\gamma\gamma$ channel with the technique introduced in the last section and evaluating the ratio (Eq.(5.1)) as a function of ϕ. Fig. 6.9 shows that there is no ϕ dependence for the dilution factor. The final result is $f = 0.782 \pm 0.036$.

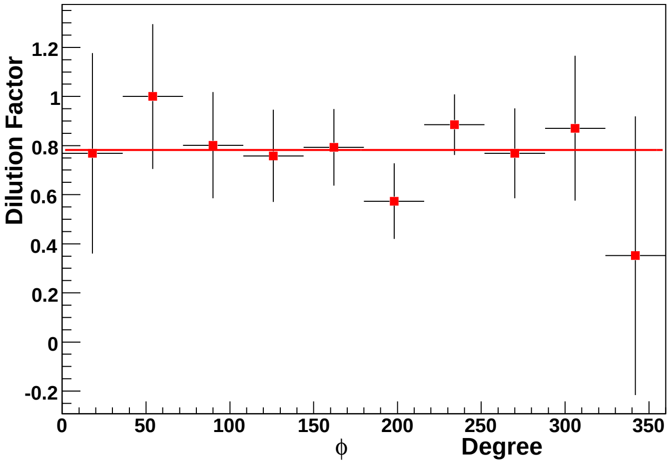

Figure 6.9. The dilution factor as a function of ϕ.

6.4 Asymmetry

Following the procedure introduced above in this section, the number of π^0 events for each ϕ bin and different target helicities are evaluated (see Appendix C) and used to calculate the target spin asymmetry with Eq.(5.8). The target spin asymmetry (A_{UL}) is calculated for each ϕ bin. Fig. 6.10 shows the target spin asymmetry in the reaction $e\vec{p} \rightarrow ep\pi^0$ for inbending data. Data are integrated in the range of Q^2 from 1 GeV^2/c^2 to 4 GeV^2/c^2 and in the range of $-t$ up to 0.6 GeV^2/c^2. Points are fitted to the function $F = p_0 sin\phi + p_1 sin2\phi$, $p_0 = 0.137 \pm 0.089$, and $p_1 = -0.317 \pm 0.087$.

Fig. 6.11 shows the target spin asymmetry of π^0 for the outbending data set. The asymmetries from the inbending data and outbending data agree well within their uncertainties and they can be combined together. The target spin asymmetry from the combined π^0 data set is shown in Fig. 6.12. The target spin asymmetry will be used to correct the asymmetry of single photon events for the π^0 contribution. Note that the asymmetry for π^0 production has a dominant $sin2\phi$ dependence while the asymmetry for the photon production has a dominant $sin\phi$ dependence. This indicates that the π^0 contamination in the single photon observed events is small.

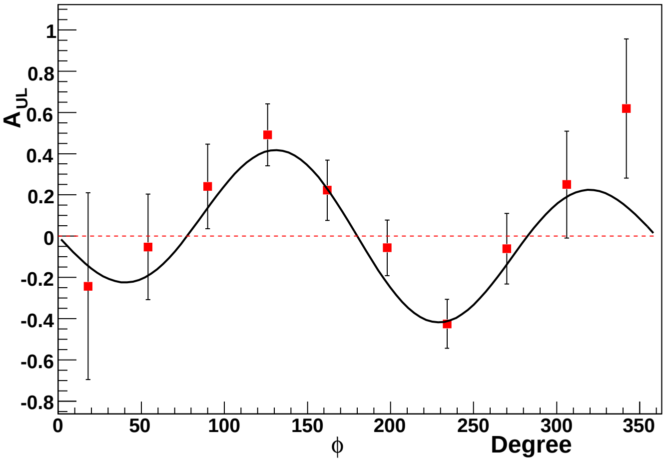

Figure 6.10. The target spin asymmetry in the reaction $e\vec{p} \rightarrow ep\pi^0$ from inbending data set. Points are fitted with function $F = p_0 sin\phi + p_1 sin2\phi$, and $p_0 = 0.137 \pm 0.089$, and $p_1 = -0.317 \pm 0.087$. $< Q^2 >= 1.68$, $< -t >= 0.35$, and $< x_B >= 0.28$.

In summary, the target spin asymmetry is measured in order to correct the asymmetry for DVCS due to the π^0 contamination. The exclusive π^0 is identified by two detected photons. For the deep inelastic scattering of π^0 production, π^0 events are dominated by those from the unpolarized nitrogen. To suppress the large background from the unpolarized nitrogen, an angular and energy difference cuts are developed. The identified π^0 sample and the asymmetry will be used in the next two chapters to obtain the final DVCS asymmetry results.

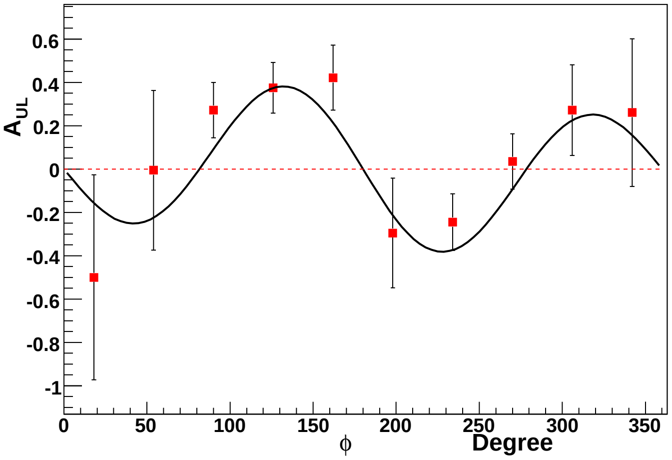

Figure 6.11. The target spin asymmetry in the reaction $e\vec{p} \rightarrow ep\pi^0$ from outbending data set. Points are fitted with function $F = p_0 sin\phi + p_1 sin2\phi$, and $p_0 = 0.092 \pm 0.072$, and $p_1 = -0.315 \pm 0.085$. $< Q^2 >= 1.58$, $< -t >= 0.37$, and $< x_B >= 0.28$.

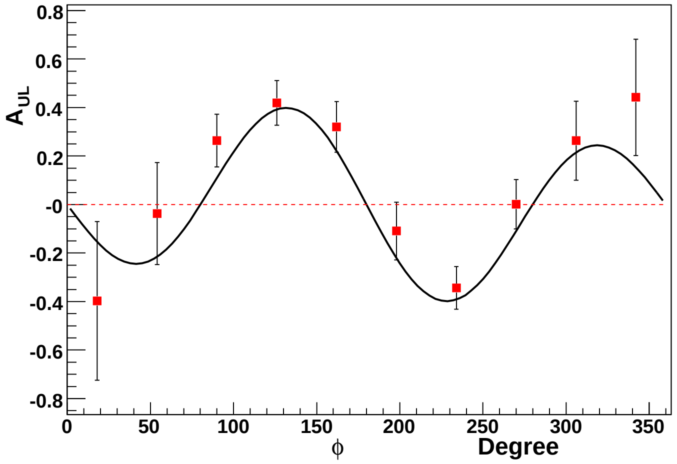

Figure 6.12. Target Spin Asymmetry in the reaction $e\vec{p} \rightarrow ep\pi^0$ from all of the data. Points are fitted with function $F = p_0 sin\phi + p_1 sin2\phi$, and $p_0 = 0.109 \pm 0.056$, and $p_1 = -0.319 \pm 0.061$. $< Q^2 >= 1.64$, $< -t >= 0.36$, and $< x_B >= 0.28$.

CHAPTER 7

MONTE CARLO SIMULATION

7.1 Overview

As pointed out in Chapter 5, due to spatial resolution of the calorimeter, the final DVCS/BH events may be contaminated by π^0 events. To estimate the π^0 contamination in the final single-photon events, a Monte Carlo (MC) simulation was performed. The main idea is to generate both DVCS and π^0 physics events, then pass them through a detector simulation program of CLAS spectrometer. The simulation output is then processed the same as the data obtained with CLAS. After normalizing the MC data to the real data, the number of π^0 events mis-identified as DVCS events can be extracted.

7.2 Event Generator

A Monte-Carlo DVCS generator based on the procedure developed by V. Korotkov[57] was developed by H. Avakian for CLAS to simulate photon electroproductions and the π^0s. As described in Chapter 1, the five-fold cross section for photon electroproductions can be parameterized in terms of GPDs and well known form factors. The DVCS event generator uses the GPD models from Ref[18]. The bag model calculations[58] show a weak dependence of the distributions on the skewedness parameter ξ, therefore, in the simplest way, V. Korotkov assumes that GPDs are independent on the skewedness parameter ξ. In this case, only $u-$ and $d-$quark GPDs are non-zero, the GPDs (H, $\widetilde{H}$, E, and $\widetilde{E}$) are parameterized in the following equations.

$$\begin{aligned} H^u(x,\xi,\Delta^2) &= u(x)\ F_1^u(\Delta^2)\,/\,2\ , \\ H^d(x,\xi,\Delta^2) &= d(x)\ F_1^d(\Delta^2)\ , \end{aligned} \tag{7.1}$$

where $u(x)$ and $d(x)$ are the quark density distributions and $F_1^{u(d)}(\Delta^2)$ is the elastic Dirac form factors defined through the proton and neutron electromagnetic form factors:

$$F_1^u = 2F_1^p + F_1^n,\ \ F_1^d = F_1^p + 2F_1^n. \tag{7.2}$$

$$\begin{aligned} \widetilde{H}^u(x,\xi,\Delta^2) &= \Delta u_v(x)\ g_A^u(\Delta^2)/g_A^u(0)\ , \\ \widetilde{H}^d(x,\xi,\Delta^2) &= \Delta d_v(x)\ g_A^d(\Delta^2)/g_A^d(0)\ . \end{aligned} \tag{7.3}$$

Here $\Delta u_v(x)$ and $\Delta d_v(x)$ are the quark helicity distributions, and $g_A^{u(d)}(\Delta^2)$ are axial vector form factors defined through the nucleon isoscalar axial form factors:

$$g_A^u = \frac{1}{2}g_A + \frac{1}{2}g_A^0,\ \ g_A^d = -\frac{1}{2}g_A + \frac{1}{2}g_A^0,\ \text{and}\ g_A^0 = \frac{3}{5}g_A. \tag{7.4}$$

$$\begin{aligned} E^u(x,\xi,\Delta^2) &= u(x)\ F_2^u(\Delta^2)\,/\,2\ , \\ E^d(x,\xi,\Delta^2) &= d(x)\ F_2^d(\Delta^2)\ , \end{aligned} \tag{7.5}$$

where $F_2^{u(d)}$ is the elastic Pauli form factor defined in the same way as $F_1^{u(d)}$ in Eq. (7.2).

$$\widetilde{E}^u(x,\xi,\Delta^2) = -\widetilde{E}^d(x,\xi,\Delta^2) = \frac{1}{2}\ \widetilde{E}_{\pi-pole}(x,\xi,\Delta^2)\ , \tag{7.6}$$

$$\widetilde{E}_{\pi-pole}(x,\xi,\Delta^2) = \theta\left(-\xi \le x \le \xi\right)\ h_A(\Delta^2)\ \frac{1}{\xi}\ \Phi\left(\frac{x}{\xi}\right)\ , \tag{7.7}$$

where $\Phi(z) = 3/4(1-z^2)$ is the pion distribution amplitude, $h_A(\Delta^2) = \frac{4M^2 g_A}{m_\pi^2 - \Delta^2}$, and $\theta(x)$ is the usual step function.

The main background for DVCS events is from π^0 production, and the cross section used in MC is discussed in Ref.[59]. Neglecting QCD logarithmic evolution of generalized parton distributions, a simple approach based on a fit to the results of the exact formula [60] is used for π^0simulation:

$$\frac{d\sigma}{dt}(\gamma_L\ p \to \pi^0\ p) = \frac{d\sigma}{dt}(x,Q^2)\bigg|_{t=\mathrm{t_{min}}} \times e^{B(t-t_{min})}, \tag{7.8}$$

where:

$$\left.\frac{d\,\sigma}{d\,t}(x,Q^2)\right|_{t=\mathrm{t_{min}}} = \frac{\alpha_S{}^2(Q^2)\cdot \mathrm{PF}(x,Q^2)\cdot \mathrm{UF}(x)}{Q^2(Q^2+M^2)^2}. \tag{7.9}$$

where, $\alpha_S(Q^2)$ is the one-loop QCD coupling constant ($\Lambda_{QCD} = 0.3$ GeV). In this equation, $\mathrm{PF}(x,Q^2)$ is given by:

$$\mathrm{PF}(x,Q^2) = \frac{Q^4\ (1-x)}{\left(-Q^2 - 0.881721\,x + Q^2\,x\right)^2}. \tag{7.10}$$

$\mathrm{UF}(x)$ is the part of the cross-section which is independent of Q^2.

A simple approximation is used for $\mathrm{UF}(x)$:

$$\mathrm{UF}(x) = (\Delta u(x,Q^2) - \Delta d(x,Q^2))^2.$$

A total of 200,000 DVCS and 200,000 π^0 events were generated with longitudinally polarized proton target with the following kinematic requirements: $x = 0.1 \sim 0.65$, $-t = 0 \sim 0.6$, $Q^2 = 1 \sim 6$, $E_{beam} = 5.725$. It should be noted that these are the only physics Monte-Carlo events as no additional background channels are simulated. The kinematic dependences (Q^2, $-t$, x_B, ϕ) of the DVCS and π^0 cross sections are shown in Fig. 7.1 and Fig. 7.2.

7.3 Detector Simulation

GSIM is the GEANT based simulation program of the CLAS spectrometer. The generated events (four-vectors of particles) are passed through GSIM. With GSIM, particles are traced through detectors and hits are generated, then a simulated data file is produced. The simulated data represent the data that one would obtain with a perfectly working detector.

The target of EG1b was polarized using a super-conducting Helmholtz magnet. This magnet blocks the protons with large scattering angle between 50^o and 80^o, and it substantially affects the acceptance of DVCS events. Besides this, the Helmholtz magnetic field deflects charged particles. Therefore, to take the polarized target into account, GSIM for EG1b is different from the standard GSIM for CLAS. The EG1b target magnet geometry was implemented in the GSIM code by C. Smith[61]. To simulate the Helmholtz magnet field, a field map was used. This field map was the same as that used in the reconstruction

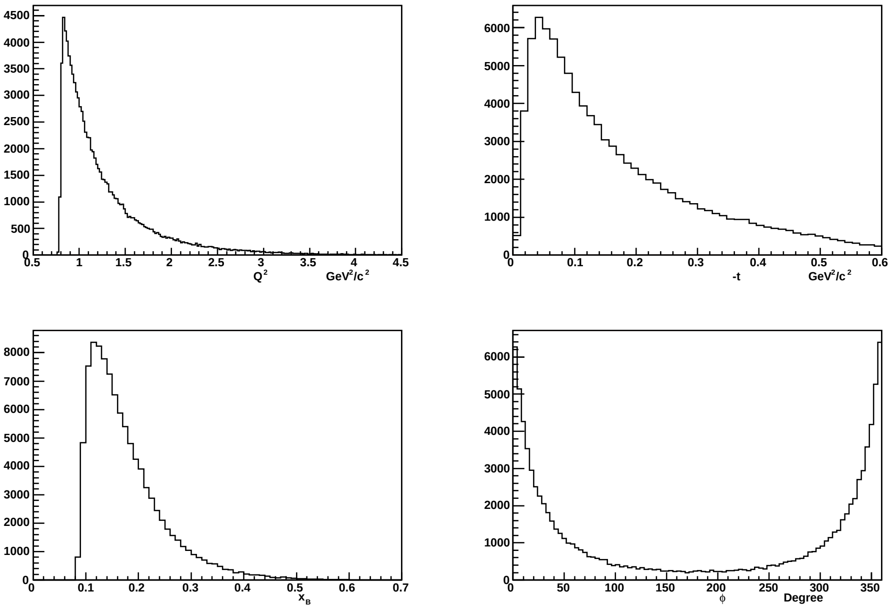

Figure 7.1. Kinematic dependences of the DVCS model.

program. Since there are two data sets for EG1b with different torus currents (2250 A and -2250 A), the generated events are passed through GSIM twice with different torus currents, 2250 A and -2250 A. A CLAS schematic of a GSIM event is shown in Fig. 7.3.

The output file from GSIM is produced with perfect timing resolution for each detector. After the event is processed with GSIM, it is then processed through the GSIM Post Processor (GPP) which smears the TOF times and the drift chamber DOCA, by adding a pseudo-random time from a Gaussian distribution to each detector. GPP also simulates "dead" detector elements, such as dead wires in the drift chambers, and bad TOF scintillator paddles.

After GPP processing, the simulated data were processed like the real data using the CLAS reconstruction program "user_ana". It is important to note that these cooked data are then analyzed with the same procedure as the real data. In summary, a flowchart shown in Fig. 7.4 describes the process of performing MC simulations.

Among CLAS experiments, EG1 is the first experiment to use the polarized target, and this analysis is also the first one to perform MC simulations for CLAS with polarized

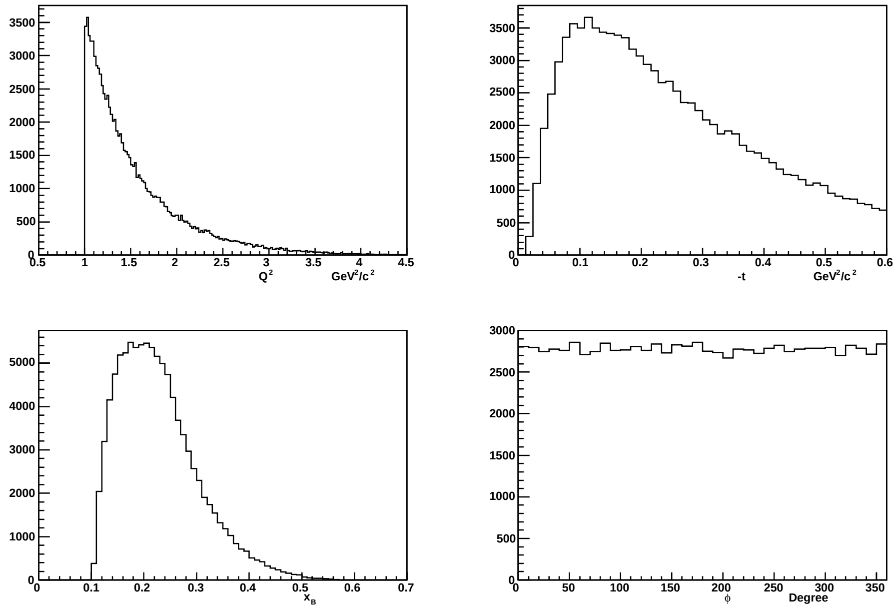

Figure 7.2. Kinematic dependences of the π^0 model.

target magnet. Given this, it was worthwhile to check the target magnet geometry and field for correctness. Fig. 7.5 shows the polar angle distributions for generated protons and reconstructed protons and for protons from EG1b data. Due to the target magnet, the acceptance decreases largely to zero for protons with polar angle greater than 48^o for both MC and data, which shows that the target magnet geometry is correct. The target magnet field is approximately axial and parallel to the beam direction, therefore, the trajectory of the charged particle was deflected azimuthally when the charged particle flies from the target to the DC superlayer 1. The ϕ shift $(\phi_{DC} - \phi_{vertex})$ is clearly visible in Fig. 7.6 for both electrons and protons. The shifts in ϕ are extracted for both data and MC simulations, and they agree well with each other. It was concluded that the target magnet field is correctly simulated. The kinematics of the generated particle and reconstructed particle are compared in Fig. 7.7, Fig. 7.8, and Fig. 7.9 which show that both electrons and protons are well reconstructed.

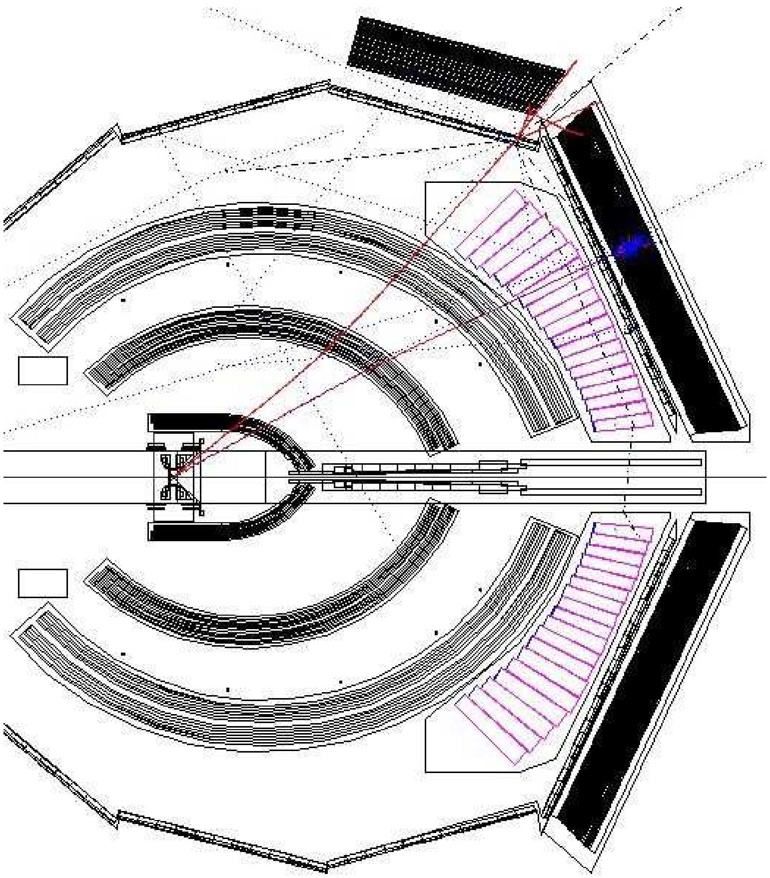

Figure 7.3. The schematic view of a GSIM event in CLAS. From inside to outside, the target, the target magnet, DC, CC, TOF, and EC are simulated. Two red curves are trajectories of the electron and proton, respectively. Due to the positive torus current (I=2250 A), the electron trajectory is bended toward the beam direction, the proton trajectory, in contrast, is bended away the beam direction.

7.4 π^0 contamination

With help of MC simulations, the overall acceptance for one photon detected π^0 production ($\eta_{\pi^0(\gamma)}$), two photons detected π^0 production ($\eta_{\pi^0(\gamma\gamma)}$), and one photon detected DVCS/BH (η_{DVCS}) can be calculated. Here, both one photon detected π^0 events and DVCS events are selected with the same procedure as the data (see Chapter 5). The two photons detected π^0 events are also selected similar to the data (see Chapter 6). The acceptance

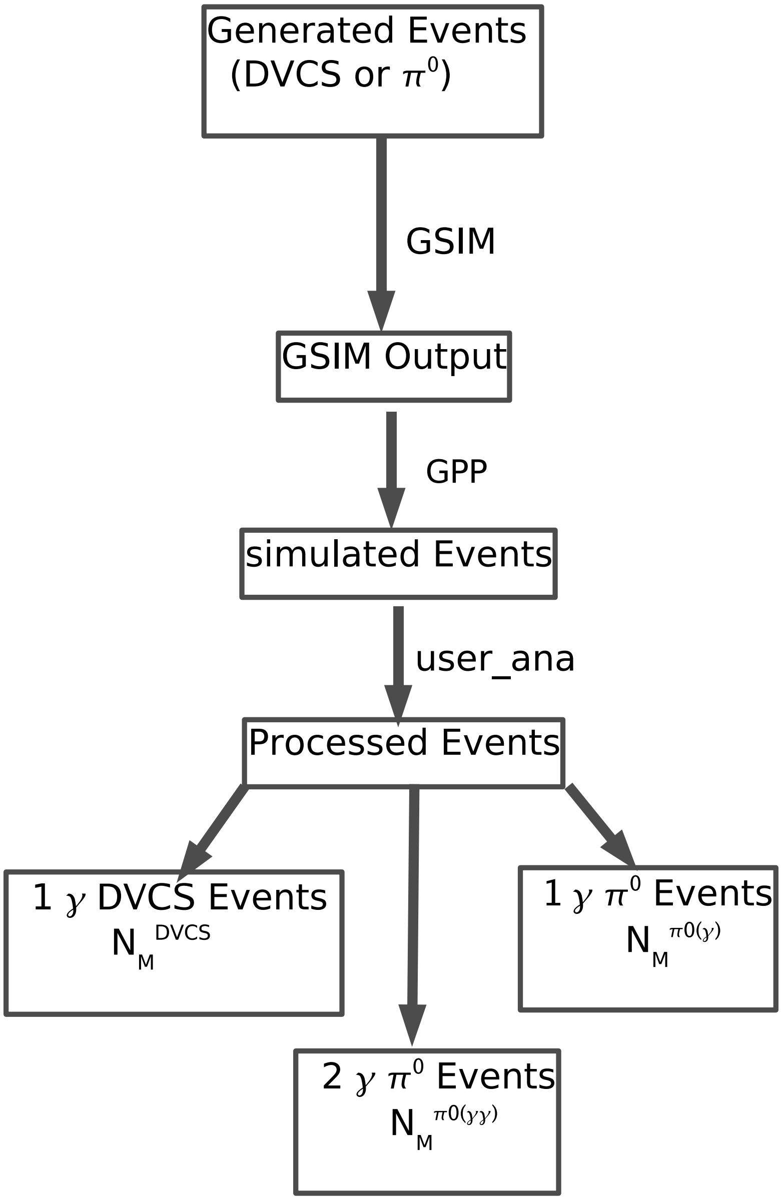

Figure 7.4. Flowchart describing the process of performing MC simulations.

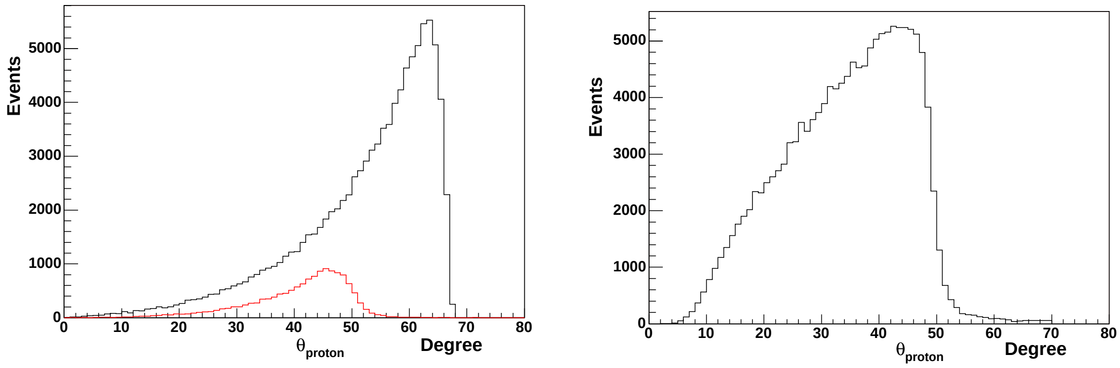

Figure 7.5. Left panel: The distribution of the polar angle for generated protons (black curve) and reconstructed protons (red curve). Right panel: the distribution of the polar angle for protons from EG1b. Due to the target magnet, the acceptance decreases largely to zero for protons with polar angle grade than 48^o for both MC and data. This shows that the target magnet geometry is corretly implemented in GSIM code. Since the protons in right panel is not only from DVCS events, the distributions are different.

$\eta_{\pi^0(\gamma)}$, $\eta_{\pi^0(\gamma\gamma)}$, and η_{DVCS} are defined in the following equations,

$$\eta_{\pi^0(\gamma)} = \frac{N_M^{\pi^0(\gamma)}}{N_G^{\pi^0}} \equiv \frac{N_D^{\pi^0(\gamma)}}{N_P^{\pi^0}} \tag{7.11}$$

$$\eta_{\pi^0(\gamma\gamma)} = \frac{N_M^{\pi^0(\gamma\gamma)}}{N_G^{\pi^0}} \equiv \frac{N_D^{\pi^0(\gamma\gamma)}}{N_P^{\pi^0}} \tag{7.12}$$

$$\eta_{DVCS} = \frac{N_M^{DVCS}}{N_G^{DVCS}} \equiv \frac{N_D^{DVCS}}{N_P^{DVCS}} \tag{7.13}$$

where,

- $N_M^{\pi^0(\gamma)}$ is the accepted number of one photon detected π^0 events from MC,
- $N_G^{\pi^0}$ is the generated number of π^0 events from MC,
- $N_D^{\pi^0(\gamma)}$ is the observed number of one photon detected π^0 events from data which is unknown,
- $N_P^{\pi^0}$ is the produced number of π^0 events from data,

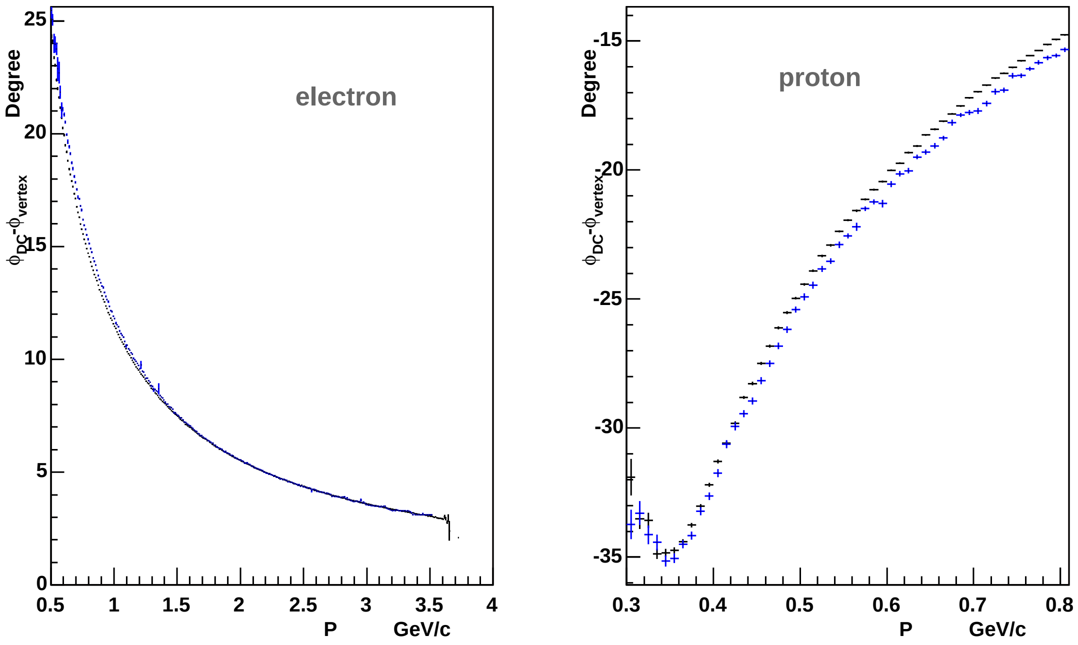

Figure 7.6. $\phi_{DC} - \phi_{vertex}$ vs p for electrons (left plot) and protons (right plot). The black points are from data, and blue points are from MC simulation.

- $N_M^{\pi^0(\gamma\gamma)}$ is the accepted number of two photons detected π^0 events from MC,
- $N_D^{\pi^0(\gamma\gamma)}$ is the observed number of two photons detected π^0 events from data,
- N_M^{DVCS} is the accepted number of photon production events from MC,
- N_G^{DVCS} is the generated number of DVCS events from MC,
- N_D^{DVCS} is the observed number of DVCS events from data which is unknown,
- N_P^{DVCS} is the produced number of DVCS events from data.

As mentioned in the Chapter 5, the observed single photon events(N_D^{γ}) was contaminated by one photon detected π^0 events ($N_D^{\pi^0(\gamma)}$). The observed number of DVCS/BH events can be calculated using equation

$$N_D^{DVCS} = N_D^{\gamma} - N_D^{\pi^0(\gamma)} \tag{7.14}$$

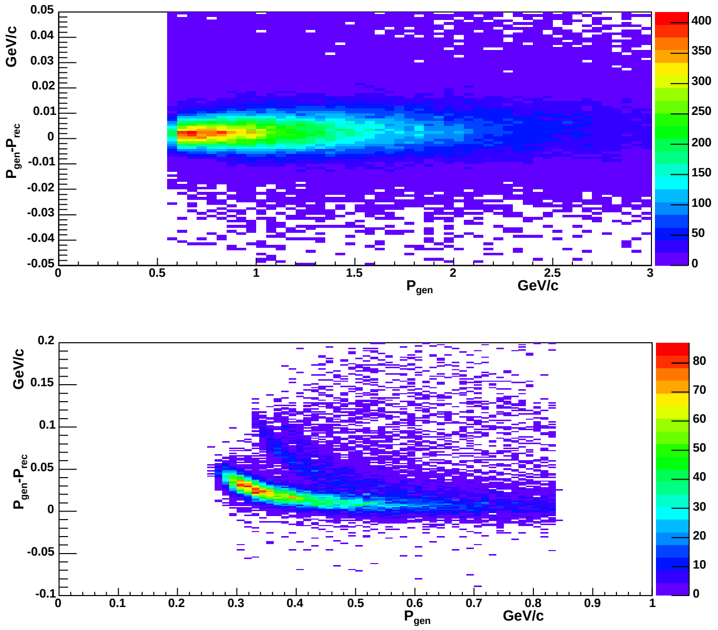

Figure 7.7. The momentum difference between the generated particle and reconstructed particle vs the momentum of the generated particle. The top panel is from electrons, and bottom panel is from protons. In the bottom panel, the up tail is because of proton energy loss, and the upper band is from the protons which hit the edge of Helmholtz coils, and lose much more energy than other protons.

$N_D^{\pi^0(\gamma)}$ can be calculated from Eq.(7.11) and Eq.(7.12),

$$N_D^{\pi^0(\gamma)} = \frac{\eta_{\pi^0(\gamma)}}{\eta_{\pi^0(\gamma\gamma)}} N_D^{\pi^0(\gamma\gamma)} \tag{7.15}$$

Then the ratio r between produced DVCS/BH and produced π^0 can be evaluated with the following formula,

$$r = N_P^{DVCS}/N_P^{\pi^0} = \frac{N_D^{DVCS}}{\eta_{DVCS}} / \frac{N_D^{\pi^0(\gamma\gamma)}}{\eta_{\pi^0(\gamma\gamma)}}. \tag{7.16}$$

Using equations Eq.(7.14) and Eq.(7.15) along with the calculated acceptance via Monte Carlo, the result obtained for the ratio is $r = 4.124 \pm 0.386$

Finally we can easily calculate the fraction of π^0 in photon production events with Eq. 7.17. The π^0 contamination as a function of ϕ is found to range from 10% to 40%, and the π^0 fraction as a function of ϕ is shown in Fig. 7.10.

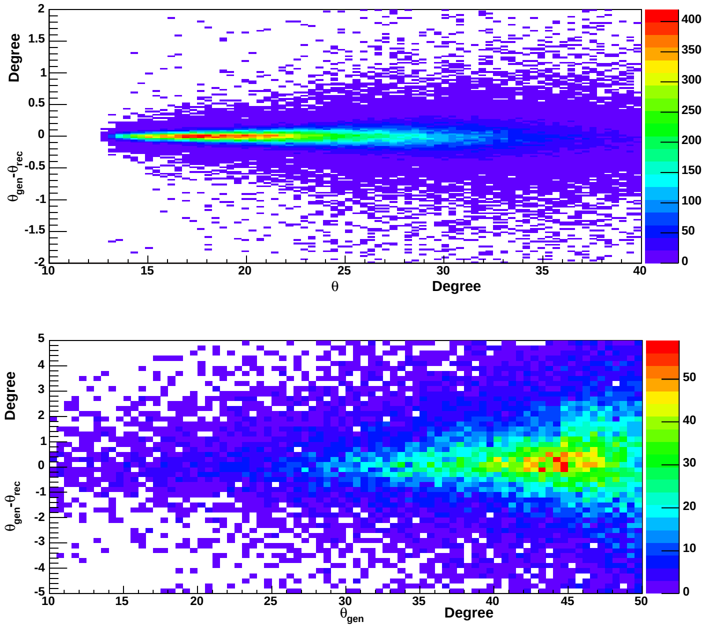

Figure 7.8. The polar angle difference between the generated particle and reconstructed particle vs the polar angle of the generated particle. The top panel is from electrons, and bottom panel is from protons.

$$f_{\pi^0}(\phi) = \frac{N_D^{\pi^0(\gamma)}(\phi)}{N_D^{\gamma}(\phi)} = \frac{N_D^{\pi^0(\gamma\gamma)}(\phi)}{N_D^{\gamma}(\phi)} \frac{\eta_{\pi^0(\gamma)}(\phi)}{\eta_{\pi^0(\gamma\gamma)}(\phi)} \tag{7.17}$$

Where ϕ is the azimuthal angle between reaction plane and scattering plane.

Following the above procedure, the MC simulation is also done for the outbending data (torus current I=-2250A), and the π^0 contamination as a function of ϕ is found as same as before (see Fig. 7.10). Considering the π^0 contribution is similar for both inbending and outbending data sets, the target spin asymmetries for two data sets were combined together before π^0 correction, and the average of π^0 fractions from two sets was used to correct π^0 contamination.

As can be seen from Fig. 7.10, the π^0 contamination is largest at $\phi = 180^o$, and smallest at $\phi = 0$ and $\phi = 360^o$. Qualitatively, this can be understood from the fact that single photon events are dominated by BH photons with peaking rates at very forward angles, which correspond to $\phi = 0^o/360^o$. At angles corresponding to $\phi = 180^o$, the BH/DVCS

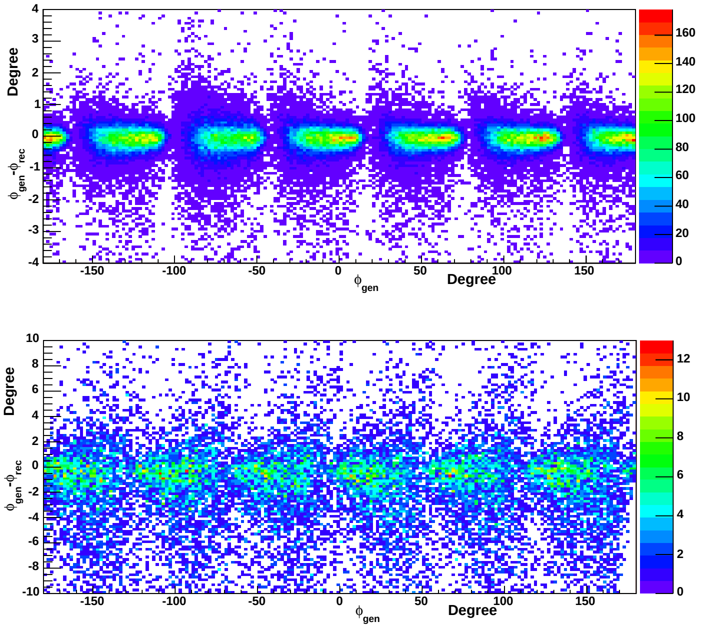

Figure 7.9. The azimuthal angle difference between the generated particle and reconstructed particle vs the azimuthal angle of the generated particle. The top panel is from electrons, and bottom panel is from protons.

rates are much smaller. On the other hand, π^0 rates are more uniformly distributed in angle and drop at a much smaller rate compared to the BH/DVCS rate. The ratio between π^0 production and photon production is therefore expected to be small at $\phi = 0^o/360^o$ and large at $\phi = 180^o$.

The fraction of DVCS in single-photon events is $f_{DVCS}(\phi) = 1 - f_{\pi^0}(\phi)$. This fraction is used to correct π^0 contamination (results are given in Chapter 8).

The acceptance functions for π^0 events of one or two photons detected and DVCS/BH events depend on angular cuts, which could affect the estimation of the π^0 fraction, therefore, variation of that angle cut is part of the estimate of the systematic error on the pion contamination (see Chapter 8).

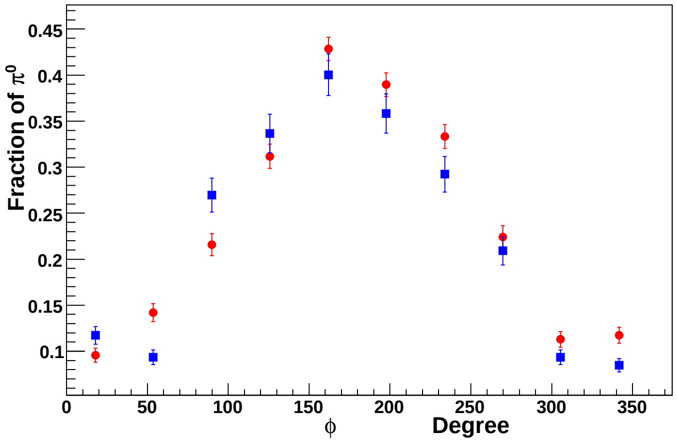

Figure 7.10. The fraction of π^0 in single-photon events as function of ϕ. The blue square denote the inbending data set, while the red circles denote the outbending data set.

7.5 Different π^0 models

In Eq. (7.17), the π^0 contamination fraction ($f_{\pi^0}(\phi)$) depends on the both acceptance functions $\eta_{\pi^0(\gamma)}(\phi)$ and $\eta_{\pi^0(\gamma\gamma)}(\phi)$, which are given by Eq. (7.11) and Eq. (7.12), respectively. These acceptance functions may depend on the π^0 model. To show the dependence, the acceptance functions are written as forms,

$$\eta_{\pi^0(\gamma)} = \frac{\int n_\gamma(x_B, t, Q^2, \phi) dx_B dt dQ^2}{\int N(x_B, t, Q^2, \phi) dx_B dt dQ^2}, \tag{7.18}$$

$$\eta_{\pi^0(\gamma)} = \frac{\int n_{\gamma\gamma}(x_B, t, Q^2, \phi) dx_B dt dQ^2}{\int N(x_B, t, Q^2, \phi) dx_B dt dQ^2}. \tag{7.19}$$

Due to the integration on the x_B, t, and Q^2 variables, it is clear that the acceptance functions depend on the π^0 model. To study the model dependence, one variable, for example, Q^2 dependence of the π^0 cross section is changed, while keeping the other variables t, x_B, and ϕ dependences. The new kinematic dependence of the π^0 cross section is not changed blindly, but changed to agree more with the data than original model. Fig. 7.11 shows the comparison between MC simulations and data where the π^0 model is described in Section 7.2.

In Fig. 7.11, some distributions of MC simulations and data don't agree well with each other, for example, the t distribution. The new π^0 models will remove the discrepancy.

The first new π^0 model is acquired by varying the Q^2 dependence while keeping other kinematic dependences. As discussed in Section 7.2, the π^0 cross section is an order $O(1/Q^6)$, while it is an order $O(1/Q^8)$ in the new model. The kinematic dependences of the π^0 cross section for the new model is shown in Fig. 7.12. The acceptances as a function ϕ from two models are shown in Fig. 7.13, and the discrepancy shows that the acceptance depends on the π^0 model. The comparison between MC simulations and data is shown in Fig. 7.14. With the new π^0 model, the fraction of π^0 contamination is approximated, and listed in Table 7.1.

Table 7.1. The fraction of π^0 acquired using the new π^0 model (varying Q^2 dependence)

ϕ (degree)	f_{π^0}	Δf_{π^0}	ϕ (degree)	f_{π^0}	Δf_{π^0}
$0-36$	0.0897	0.0075	$180-216$	0.4209	0.0223
$36-72$	0.1746	0.0108	$216-252$	0.3521	0.0200
$72-108$	0.2654	0.0186	$252-288$	0.2251	0.0148
$108-144$	0.3063	0.0182	$288-324$	0.1587	0.0112
$144-180$	0.4267	0.0213	$324-360$	0.1751	0.0116

The second new π^0 model is acquired by varying the t dependence. The kinematic dependences of the π^0 cross section for the new model is shown in Fig. 7.15. The acceptances as a function ϕ from the original and new models are shown in Fig. 7.16. The comparison between MC simulations and data is shown in Fig. 7.17, it is clear that the discrepancy on t distributions disappear. With the new π^0 model, the fraction of π^0 contamination is approximated, and listed in Table 7.2.

Table 7.2. The fraction of π^0 acquired using the new π^0 model (varying t dependence)

ϕ (degree)	f_{π^0}	Δf_{π^0}	ϕ (degree)	f_{π^0}	Δf_{π^0}
$0-36$	0.1127	0.0094	$180-216$	0.4087	0.0217
$36-72$	0.1756	0.0109	$216-252$	0.3557	0.0202
$72-108$	0.2770	0.0194	$252-288$	0.1819	0.0119
$108-144$	0.3772	0.0224	$288-324$	0.2208	0.0156
$144-180$	0.4957	0.0248	$324-360$	0.1326	0.0088

The third new π^0 model is acquired by varying the x_B dependence. The kinematic dependences of the π^0 cross section for the new model is shown in Fig. 7.18. The acceptances as a function ϕ from the original and new models are shown in Fig. 7.19. The comparison between MC simulations and data is shown in Fig. 7.20. With the new π^0 model, the fraction of π^0 contamination is approximated, and listed in Table 7.3.

The difference between the new and original π^0 models will be taken into account as the systematic uncertainties, which will be discussed in Chapter 8.

Table 7.3. The fraction of π^0 acquired using the new π^0 model (varying x_B dependence)

ϕ (degree)	f_{π^0}	Δf_{π^0}	ϕ (degree)	f_{π^0}	Δf_{π^0}
$0 - 36$	0.1181	0.0099	$180 - 216$	0.3852	0.0204
$36 - 72$	0.2522	0.0156	$216 - 252$	0.3956	0.0225
$72 - 108$	0.2511	0.0176	$252 - 288$	0.1974	0.0129
$108 - 144$	0.3287	0.0195	$288 - 324$	0.1186	0.0084
$144 - 180$	0.5528	0.0276	$324 - 360$	0.0813	0.0054

7.6 MM_X^2 for DVCS events

In above section, the fraction of π^0 is estimated to be approximately 25% to the observed single photon events. The squared missing mass MM_X^2 of (ep) for identified π^0 events is given in Fig. 6.7. In addition, Fig. 5.16 shows the MM_X^2 of (ep) for observed single photon events which are contaminated by π^0 events. To remove the π^0 contribution from the spectrum shown in Fig. 5.16, the spectrum of MM_X^2 shown in Fig. 6.7 is normalized to 25% of the number of photon production events. This distribution is then subracted from the spectrum shown in Fig. 5.16. The MM_X^2 of (ep) for photon production events after π^0 subraction is shown in Fig. 7.21. Note that the MM_X^2 centroid is 0.0025 ± 0.0017 (GeV/c^2)^2 and the MM_X^2 centroid for π^0 eventa is 0.0217 ± 0.0028, their difference is 138 MeV/c^2 with an uncertainty of 4.8 MeV/c^2, which is at the π^0 mass 135 MeV/c^2. This demonstrates that the pion subtraction is correct.

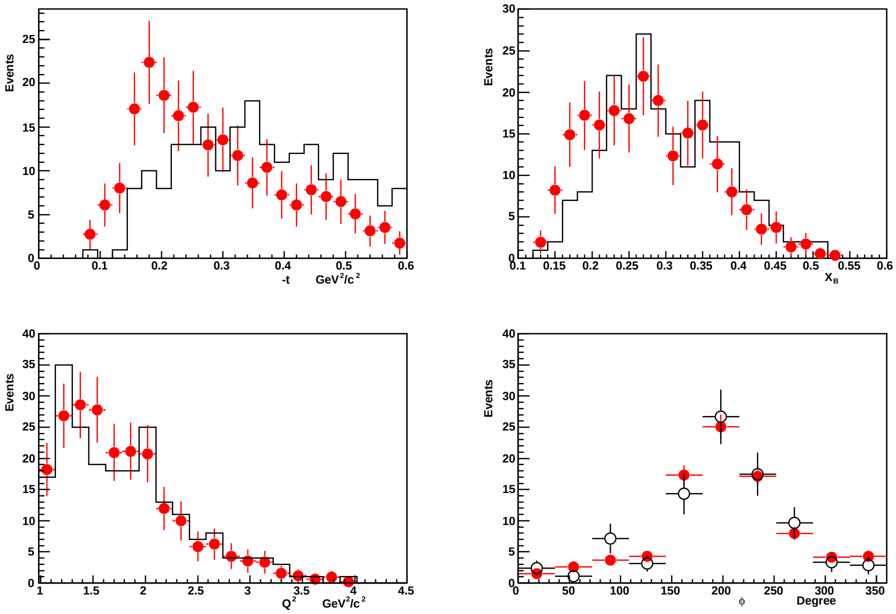

Figure 7.11. The comparison between MC simulations (red points) and the data (black line). Events are π^0s with two decay photons detected. The π^0 model is described in Section 7.2.

7.7 Two topologies of π^0 events

In the above discussion, π^0 events are divided into two topologies, corresponding to one photon detected ($T1$), and two photons detected ($T2$), respectively. The π^0 contamination of the photon production is $T1$, while the target spin asymmetry for π^0 production is measured from $T2$. Therefore, in order to correct the asymmetry of DVCS/BH due to the π^0 contamination, the asymmetry of π^0 production from $T2$ must be shown to be the same as that from $T1$. Since the π^0 asymmetry depends on the kinematics such as Q^2, $-t$, and x_B, the kinematic distributions of $T1$ and $T2$ are compared (see Fig. 7.22). Both $T1$ and $T2$ are from MC simulations. The comparison shows that the kinematic distributions are similar for them. This gives credence that the asymmetry extracted from two photons detected π^0 is the same as that resulting from π^0 background.

To summarize, the fraction of the π^0 background in the observed single photon events is approximated as a function of ϕ using MC simulations. Four π^0 models are tested and

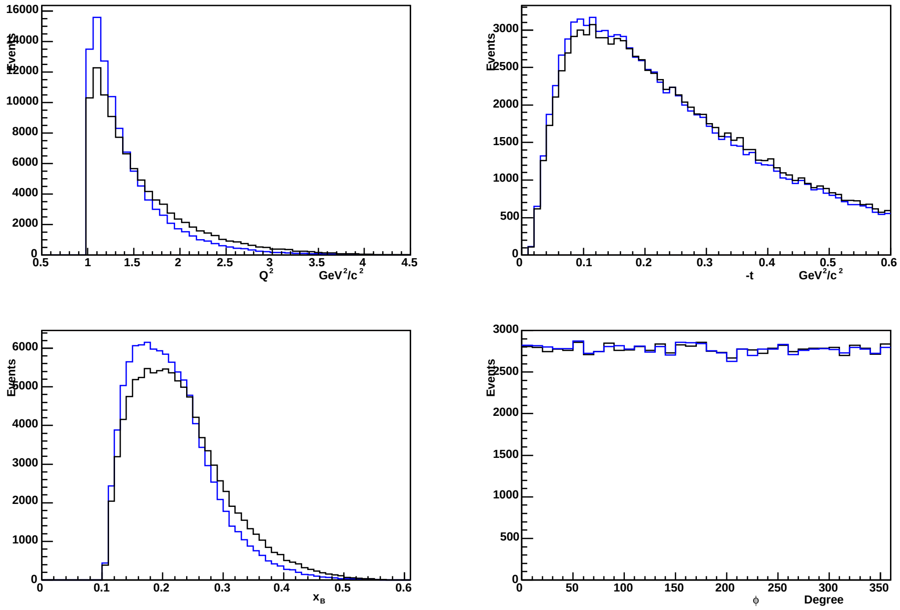

Figure 7.12. The kinematic dependences of the π^0 cross section for the new model (blue curve) and original model (black curve). The π^0 model has a new Q^2 dependence, with an order $O(1/Q^8)$.

compared with the data. The results from different models are considered in the systematic uncertainties. The MM_X^2 of ep for photon productions after subtracting π^0 background is studied, and the centroid shows that the π^0 background is removed. In addition, the kinematic distributions of two topologies of π^0 productions show that the asymmetry from one photon detected π^0 events is close to that from two photons detected. With the fraction of the π^0 background and the asymmetry for π^0 productions, the effect of π^0 contribution is removed from the asymmetry for DVCS production.

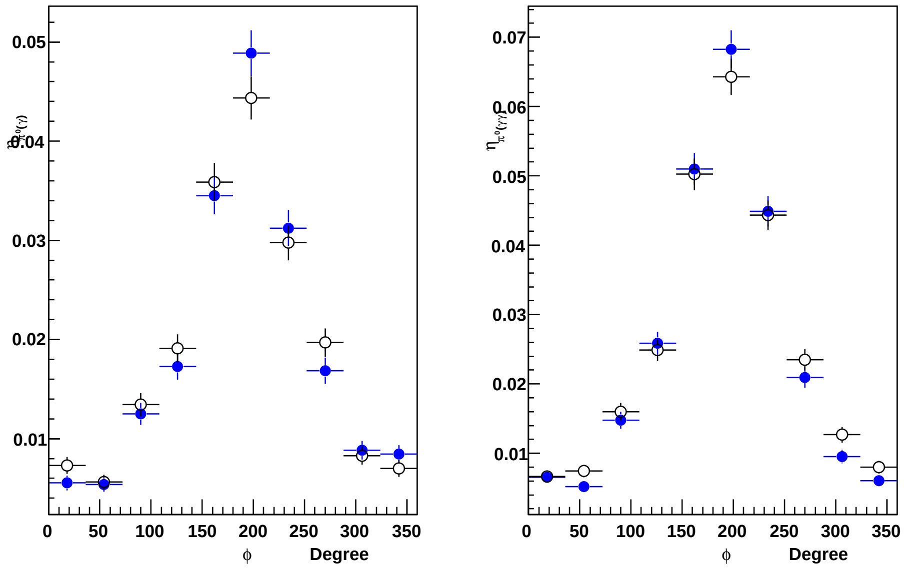

Figure 7.13. The acceptance functions of one photon detected π^0 (left plot) and two photons detected π^0 (right plot). The black empty circles represent the the original model, while blue solid circles represent the new model with different Q^2 dependence. The discrepancy shows that the acceptance depends on the π^0 model.

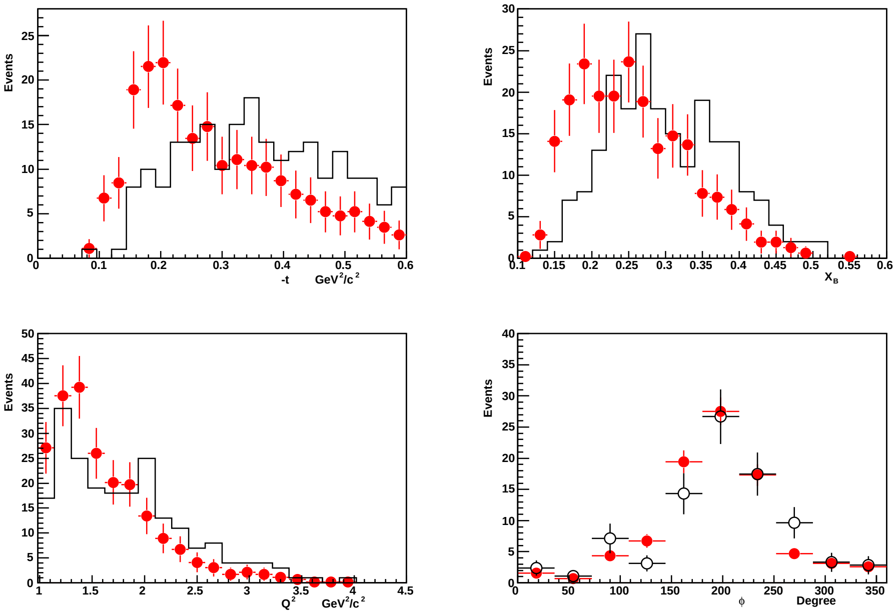

Figure 7.14. The comparison between MC simulations (red points) and the data (black line). Events are π^0s with two decay photons detected. The π^0 model has a new Q^2 dependence, with an order $O(1/Q^8)$.

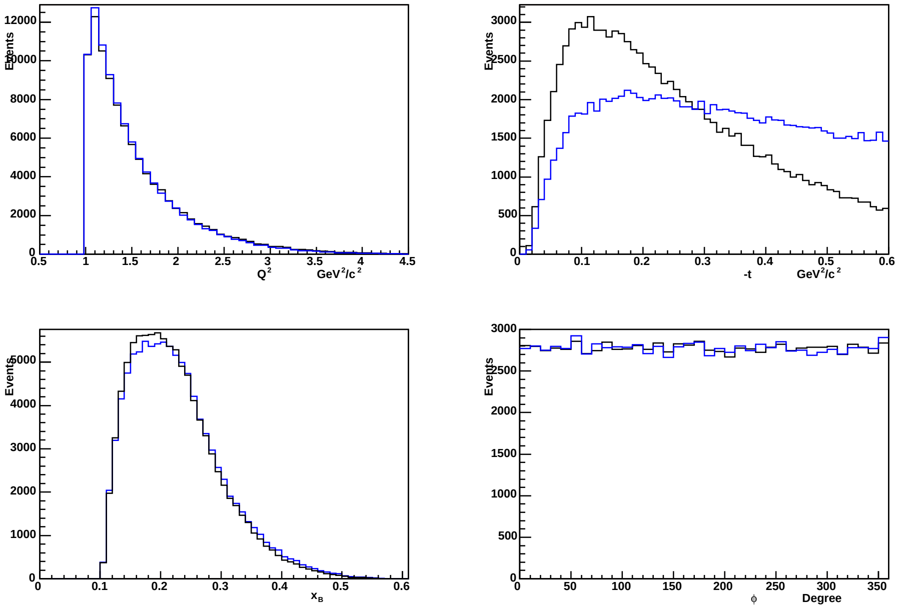

Figure 7.15. The kinematic dependences of the π^0 cross section for the new model (blue curve) and original model (black curve). The π^0 model has a new t dependence.

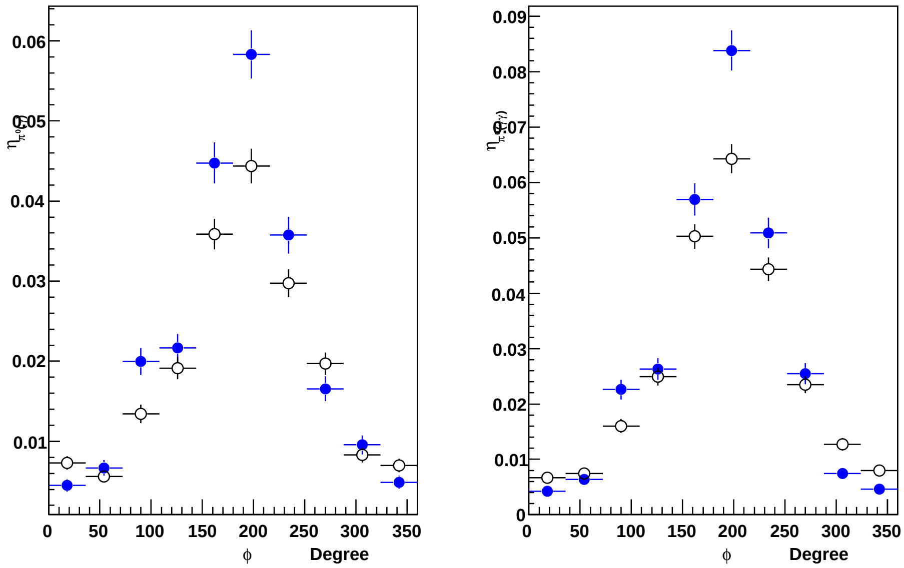

Figure 7.16. The acceptance functions of one photon detected π^0 (left plot) and two photons detected π^0 (right plot). The black empty circles represent the the original model, while blue solid circles represent the new model with different t dependence. The discrepancy shows that the acceptance depends on the π^0 model.

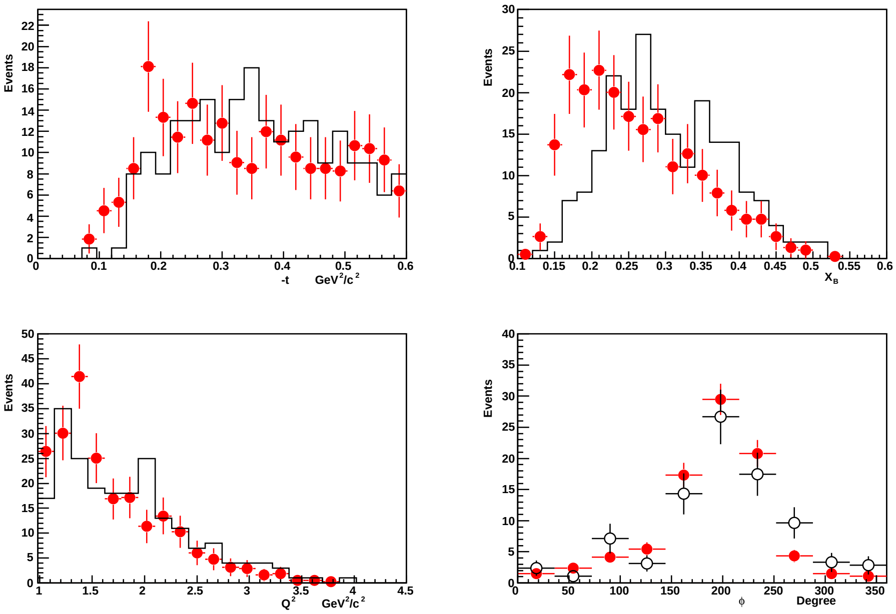

Figure 7.17. The comparison between MC simulations (red points) and the data (black line). Events are π^0s with two decay photons detected. The π^0 model has a new t dependence.

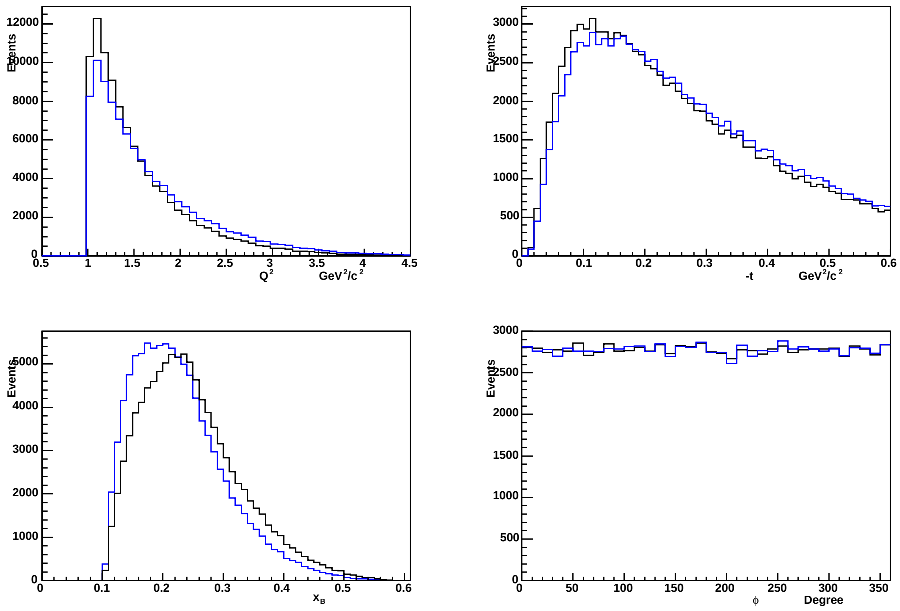

Figure 7.18. The kinematic dependences of the π^0 cross section for the new model (blue curve) and original model (black curve). The π^0 model has a new x_B dependence.

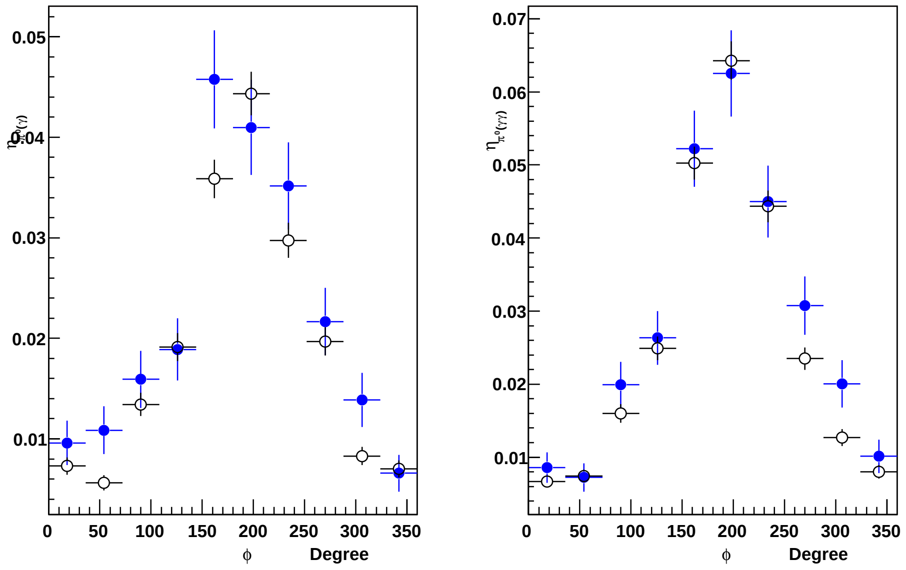

Figure 7.19. The acceptance functions of one photon detected π^0 (left plot) and two photons detected π^0 (right plot). The black empty circles represent the the original model, while blue solid circles represent the new model with different x_B dependence. The discrepancy shows that the acceptance depends on the π^0 model.

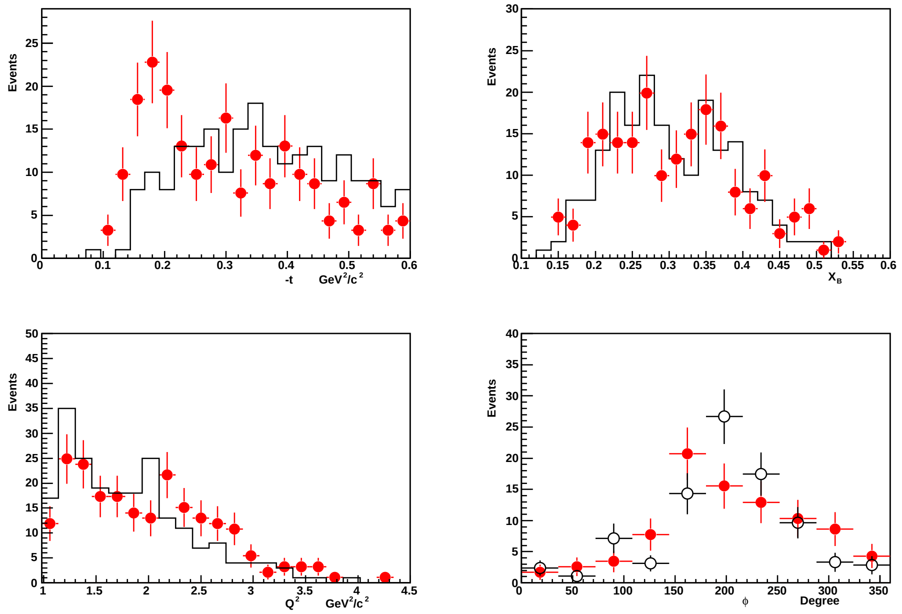

Figure 7.20. The comparison between MC simulations (red points) and the data (black line). Events are π^0s with two decay photons detected. The π^0 model has a new x_B dependence.

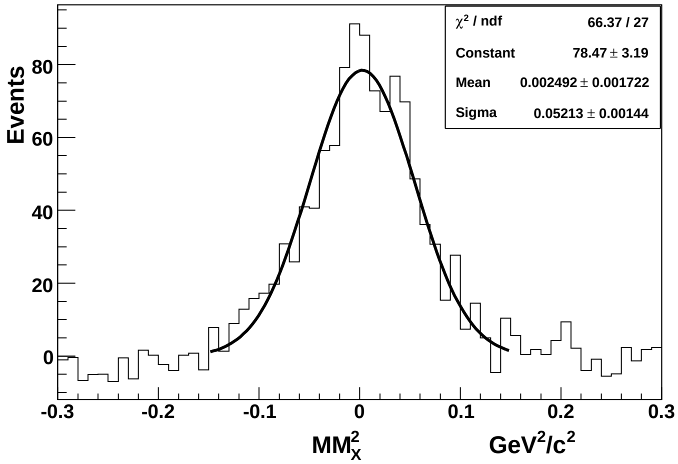

Figure 7.21. The MM_X^2 spectrum of (ep) for DVCS/BH, which is acquired from Fig. 5.16 by subtracting normalized MM_X^2 spectrum of identified π^0 as shown in Fig. 6.7.

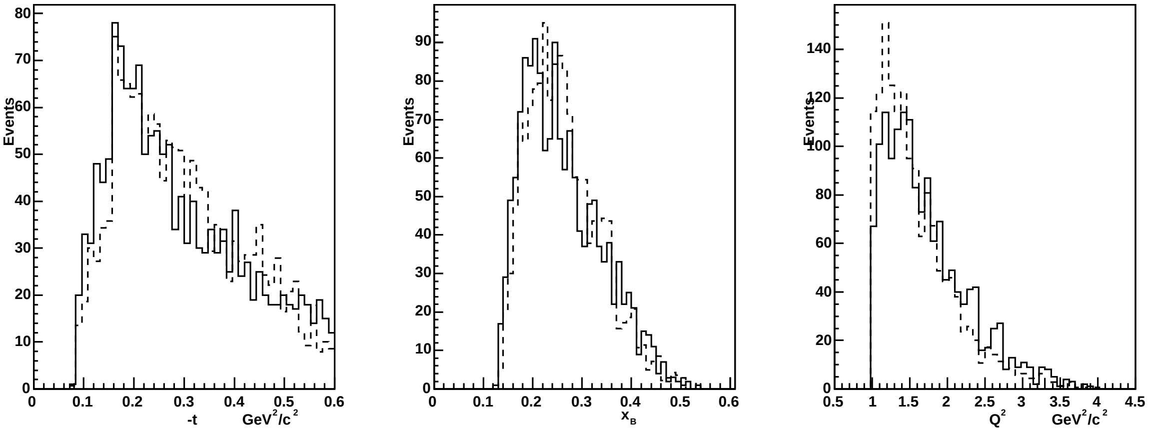

Figure 7.22. $-t$ (left panel), x_B (middle panel), Q^2 (right panel) distributions for two photons detected π^0 (solid curve) and one photon detected π^0 (dashed curve). Both of them have the same kinematic distributions.

CHAPTER 8

RESULTS AND CONCLUSIONS

8.1 Fully corrected target spin asymmetry

With help of the MC simulations, the fraction of the π^0 contamination in observed single photon sample is approximated as a function of ϕ, therefore, the target spin asymmetry for observed single photons can be calculated using the following equation:

$$A_\gamma(\phi) = f_{DVCS}(\phi)A_{DVCS}(\phi) + f_{\pi^0}(\phi)A_{\pi^0}(\phi). \tag{8.1}$$

Here, $A_\gamma(\phi)$ is the target spin asymmetry extracted from observed single photon data with π^0 contaminations, as shown in Fig. 5.14. $A_{\pi^0}(\phi)$ is the target spin asymmetry from two photons detected π^0 productions, as shown in Fig. 6.12. A_{DVCS} is the asymmetry for observed single photon productions without π^0 background.

In the target spin asymmetry for photon productions, the helicity-independent Bethe-Heitler contribution cancels out and only helicity-dependent interference between Bethe-Heitler and Deeply Virtual Compton Scattering remains. As described in Chapter 1, the target spin asymmetry A_{UL} can be written as a Fourier series,

$$A_{\mathrm{UL}}(\phi) = p_0 sin\phi + p_1 sin2\phi + \cdots, \tag{8.2}$$

where the $sin\phi$ moment (p_0) can be described as the general parton distributions with the usual form factors (see Eq. (1.55)).

The fully corrected, final target spin asymmetry is shown in Fig. 8.1, and in Fig. 8.2, which is fitted with different functions, respectively. In Fig. 8.1 and in Fig. 8.2, both dashed and dotted curves are model calculations based on Ref[17].The dashed curve is the full model prediction using the ξ-dependent GPD parameterization (b_{val}=b_{sea}=1, and $\mathcal{E}$= $\widetilde{\mathcal{E}}$=0) based on MRST02 PDFs [17], including leading twist terms only, and target mass corrections applied. The dotted curve shows the asymmetry when $\widetilde{\mathcal{H}}$=0. Since the $sin\phi$ moment does not change too much with different fit functions, and the general parton distribution model predicts the target spin asymmetry as a function of $p_0 sin\phi + p_1 sin2\phi$, we choose $p_0 sin\phi + p_1 sin2\phi$ to fit the final results.

In Fig. 8.2, a significant $sin\phi$ moment (p_0) of the target spin asymmetry is observed, and the $sin2\phi$ moment (p_1) is small. This agrees well with the model predictions. The amplitude of the theory curve decreases by a half with $\widetilde{\mathcal{H}} = 0$, which shows that the target spin asymmetry is sensitive to GPDs $\widetilde{\mathcal{H}}$.

Compared to the target spin asymmetry for observed single photon events with π^0 contaminations (see Fig. 5.14), the $sin\phi$ moment (p_0) is only slightly changed. Therefore, the $sin\phi$ moment (p_0) is not sensitive to the fraction of π^0 contamination, whereas the $sin2\phi$ moment (p_1) is. This is easily understood because the target spin asymmetry for DVCS is dominated by the $sin\phi$ moment (p_0), while the target spin asymmetry for π^0 is dominated by the $sin2\phi$ moment (p_1).

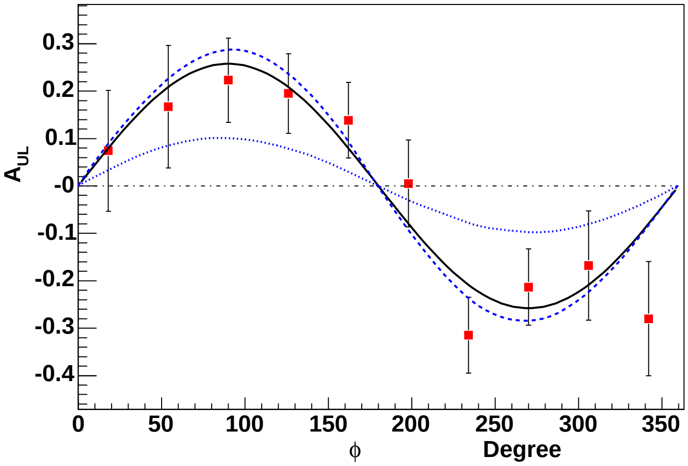

Figure 8.1. The target spin asymmetry in the reaction $e\vec{p} \to ep\gamma$. Points are fitted to the function $F = p_0 sin\phi$, and $p_0 = 0.258 \pm 0.041$. $\chi^2 = 6.6/9$. Dashed and dotted curves are model predictions[17].

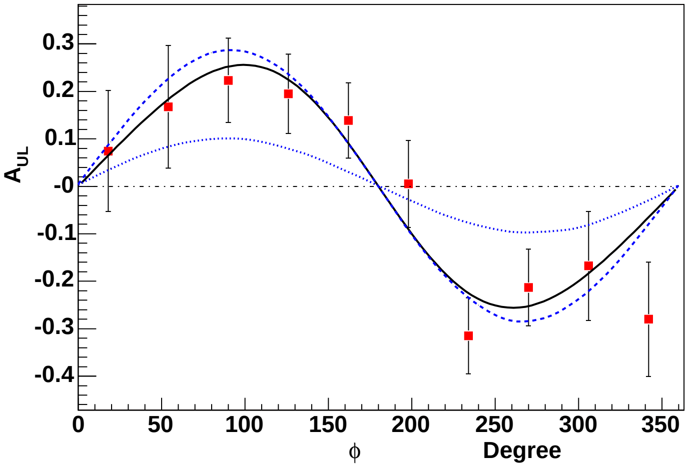

Figure 8.2. The target spin asymmetry in the reaction $e\vec{p} \rightarrow ep\gamma$. Points are fitted to the function $F = p_0 sin\phi + p_1 sin2\phi$, and $p_0 = 0.252 \pm 0.042$, $p_1 = -0.022 \pm 0.045$. $\chi^2 = 6.4/8$. Dashed and dotted curves are model predictions[17].

8.2 Systematic Error

All of the errors shown before were purely statistical. Due to uncertainties in the measurements and in π^0 models, a systematic errors arises. To understand their importance, the possible systematic errors are studied.

To determine the systematic error, the first step is to explore possible the sources (parameters) of systematic errors. Then, each parameter is varied and a new result is determined. The systematic error arising from that parameter is given by the difference between the standard result and the new result. Finally, all of the systematic errors are added in quadrature to give the total systematic error.

In this analysis, the main sources of systematic uncertainties come from the following contributions,

- Dilution factor
- Estimation of target and beam polarization
- ^{15}N polarization

- π^0 model
- Radiative corrections
- Angular cut

8.2.1 Dilution Factor

The dilution factor is extracted as $f = 0.901 \pm 0.035$. Therefore, it gives a relative uncertainty $< 4\%$.

8.2.2 Target Polarization

The target polarization was calculated using the known value of P_e and the product P_eP_t. The beam polarization was measured with a Moller polarimeter to be approximately 0.71 (slightly different for different runs). In the analysis, the maximum error 0.03 was used for all runs. The value 0.71 ± 0.03 covers all of the values measured from the Moller polarimeter. P_eP_t is determined using exclusive elastic *ep* scattering process, and the error is taken into account the systematic error. The error of target polarization is estimated from P_e and P_eP_t. The polarizations and errors are listed in the Table 4.3.

The uncertainty in the target polarization directly enters in the final asymmetry as a systematic error. This error gives a relative uncertainty of $\approx 7\%$.

8.2.3 Polarization of Nitrogen

During the data collection, the ^{15}N in target ^{15}NH$_3$ was slightly polarized. Therefore, the contribution from ^{15}N to the numerator in Eq.(5.8) gives a contribution to the target spin asymmetry. This is taken into account as a systematic uncertainty for the target spin asymmetry.

Although the polarization of nitrogen was not measured during the data run, it was estimated. In the dynamic nuclear polarization process, the polarization of all spin species in the material follow the equal spin temperature hypothesis [62, 63], i.e. they are all at the same spin temperature(T_S). Therefore, the nitrogen polarization can be estimated using the following equations,

$$P_N = tanh\frac{\mu_N B}{KT_S}, \text{ and} P_H = tanh\frac{\mu_p B}{KT_S}, \tag{8.3}$$

where μ_p and μ_N are the magnetic moments for the proton and nitrogen respectively, T_S is spin temperature, and K is Boltzmann constant. In case of $P_H \approx 70\%$, one obtains $P_N = -7\%$. Actually only the unpaired proton is polarized in nitrogen. Therefore, the polarization of the unpaired proton is

$$P_p = -\frac{1}{3}P_N \tag{8.4}$$

The polarization is $\approx 2\%$. Considering that there are less than 10% events from ^{15}N, the increase of the effective proton polarization is $\approx 0.2\%$, therefore the contribution of nitrogen to the asymmetry is negligible.

8.2.4 The π^0 model

As discussed in Section 7.5, for the MC simulations of π^0 events, the acceptance of one photon or two photons detected π^0 events depends on the π^0 models. Three different π^0 models were tested varying Q^2, t, and x_B (see Section 7.5), and the fraction of the π^0 contamination in observed single photon events was also extracted for each case. With these different models, the target spin asymmetry was extracted, and compared with the asymmetry acquired using the original π^0 model (see Fig. 8.3, Fig. 8.4, and Fig. 8.5). The difference between them was taken into account as the systematic error, as shown in Table 8.1. The respective contribution to the systematic error is <2.5%.

8.2.5 Radiative corrections

In leading order in electromagnetic interactions, the Bether-Heitler amplitude alone does not give a target spin asymmetry, while when higher-order electromagnetic corrections are included, QED loop radiative corrections can induce a target spin asymmetry. In Ref[64], the target spin asymmetry for the Bether-Heitler process is calculated showing that it is less than 0.1% for the kinematic range of this experiment.

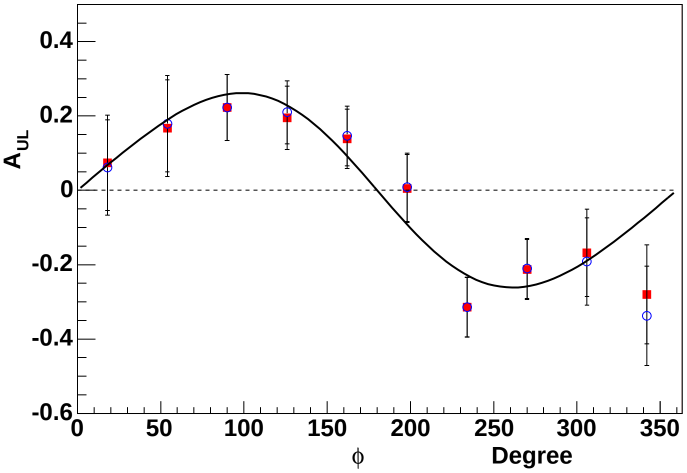

Figure 8.3. Comparison of the target spin asymmetry A_{UL} vs ϕ. The red blocks are results corrected with the original π^0 model, while blue circles are results corrected with the different π^0 model varying Q^2 dependence. Blue circles are fitted to the function $F = p_0 sin\phi + p_1 sin2\phi$, and $p_0 = 0.258 \pm 0.043$, $p_1 = -0.02 \pm 0.046$.

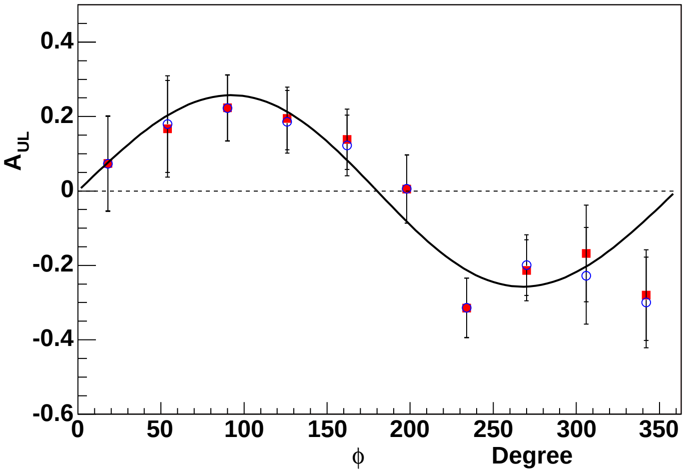

Figure 8.4. Comparison of the target spin asymmetry A_{UL} vs ϕ. The red blocks are results corrected with the original π^0 model, while blue circles are results corrected with a varying t dependent π^0 model. Blue circles are fitted to the function $F = p_0 sin\phi + p_1 sin2\phi$, and $p_0 = 0.257 \pm 0.043$, $p_1 = -0.005 \pm 0.046$.

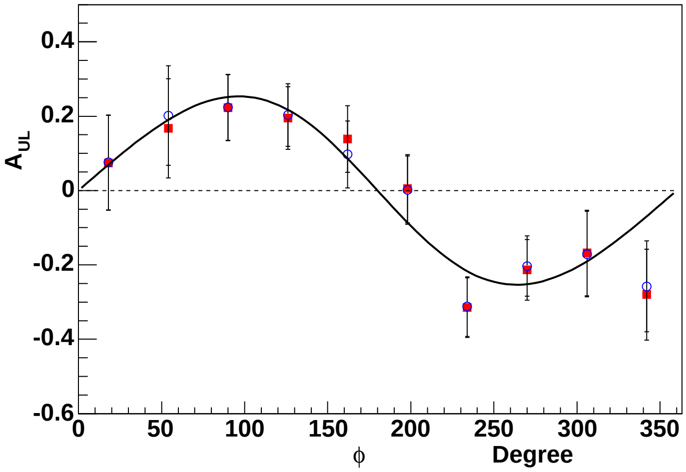

Figure 8.5. Comparison of the target spin asymmetry A_{UL} vs ϕ. The red blocks are results corrected with the original π^0 model, while blue circles are results corrected with a varying x_B dependent π^0 model. Blue circles are fitted to the function $F = p_0 sin\phi + p_1 sin2\phi$, and $p_0 = 0.252 \pm 0.043$, $p_1 = -0.014 \pm 0.046$.

Another radiative correction in the Bether-Heitler process may come from real-photon radiation. In this analysis, an angular cut is imposed to remove events with more than one photon, therefore, the phase space of an undetected photon is relatively small. In this case, it is shown in Ref[64], that polarization observables are not affected.

8.2.6 Angular cut

In order to remove one photon detected π^0 events and suppress nuclear background, the data are selected with a cut on $\theta_{\gamma\gamma'} < 2^o$, which is a loose cut to maximize statistics. To study how much the asymmetry depends on the cut, a tight one, $\theta_{\gamma\gamma'} < 1.5^o$, was tested. The target spin asymmetry was calculated with the same procedure, and the comparison is shown in Fig. 8.6. In each ϕ bin, the difference between the asymmetry obtained using $\theta_{\gamma\gamma'} < 2^o$ and $\theta_{\gamma\gamma'} < 1.5^o$ is considered as the systematic error, as shown in Table 8.1. The contribution to the systematic uncertainty is <5%.

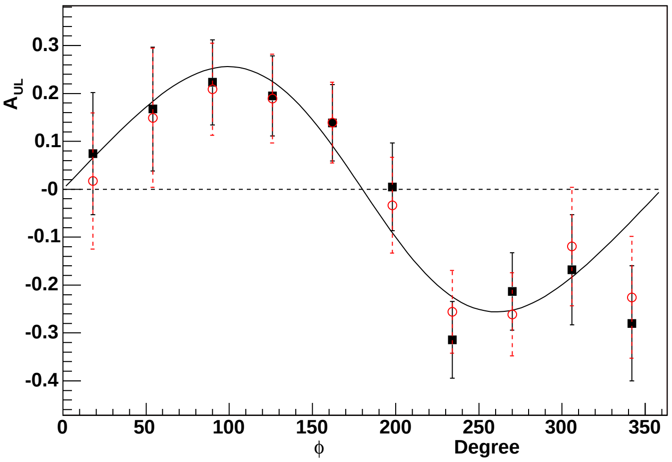

Figure 8.6. Comparison of the target spin asymmetry A_{UL} vs ϕ. The black squares represent A_{UL} obtained using $\theta_{\gamma\gamma'} < 2^o$, while the red circles represent A_{UL} obtained using $\theta_{\gamma\gamma'} < 1.5^o$.

8.2.7 Summary of errors

The systematic errors discussed in this section are largely uncorrelated, and the total systematic uncertainty is the square root of the sum over square of each term. The tested systematic error is shown in Fig. 8.7 as an error band at the bottom of the Figure. Therefore, the final fit result for target spin asymmetry is $p_0 = 0.252 \pm 0.042^{stat} \pm 0.020^{sys}$, and $p_1 = -0.022 \pm 0.045^{stat} \pm 0.021^{sys}$. The target spin asymmetry is dominated by statistical uncertainties.

The systematic uncertainties from different sources in each ϕ bin are listed in the Table 8.1 for A_{UL}.

8.3 Kinematic Dependences

In addition, the kinematic dependence of the $sin\phi$ moment of the target spin asymmetry as functions of $-t$ and x_B was studied. Due to the low statistics, three bins were made for both $-t$ and x_B.

With help of MC simulations, the fraction of π^0 was estimated for each bin. See Appendix D.

Table 8.1. The systematic uncertainty for A_{UL} in summary

ϕ (degree)	f	P_t	π^0 model	Angular cut	Total error
$0 \sim 36$	0.0030	0.0052	-0.0132	0.0714	0.0728
$36 \sim 72$	0.0067	0.0117	0.0117	0.0184	0.0256
$72 \sim 108$	0.0089	0.0156	-0.0001	0.0142	0.0228
$108 \sim 144$	0.0078	0.0136	0.0148	0.0058	0.0223
$144 \sim 180$	0.0055	0.0097	0.0075	-0.0004	0.0134
$180 \sim 216$	0.0002	0.0004	0.0031	0.0384	0.0385
$216 \sim 252$	0.0013	0.0220	0.0006	-0.0591	0.0642
$252 \sim 288$	0.0085	0.0149	0.0027	0.0481	0.0511
$288 \sim 324$	0.0067	0.0117	-0.0239	-0.0483	0.0556
$324 \sim 360$	0.0112	0.0196	-0.0575	-0.0544	0.0822

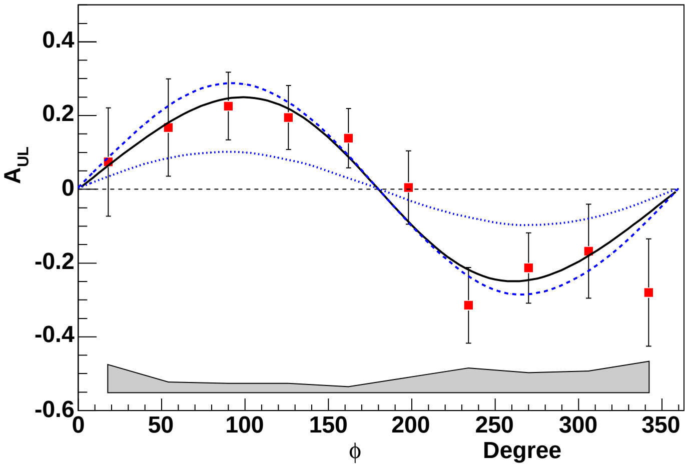

Figure 8.7. The final result for the target spin asymmetry in the reaction $e\vec{p} \rightarrow ep\gamma$. Points are fitted to the function $F = p_0 sin\phi + p_1 sin2\phi$ (solid curve) with parameters $p_0 = 0.252 \pm 0.042^{stat} \pm 0.020^{sys}$ and $p_1 = -0.022 \pm 0.045^{stat} \pm 0.021^{sys}$. Dashed and dotted curves are the model predictions[17]. The error band at the bottom represents the systematic uncertainty.

In order to correct the target spin asymmetry of DVCS due to the π^0 contaminations, the target spin asymmetry of π^0 as a function of ϕ was extracted for each $-t$ bin and x_B bin. For each bin, the asymmetry was fitted to the function $p_0 sin\phi + p_1 sin2\phi$ with free parameters p_0 and p_1. The results are listed in Table 8.2, and are used to correct the target spin asymmetry for observed single photon events.

For each $-t$ bin or x_B bin, both the target spin asymmetry of π^0 and the fraction of π^0 background in observed single photon events were extracted. This allows the target spin asymmetry for single photon production for each $-t$ bin or x_B bin to be extracted and corrected due to the π^0 contaminations. The kinematic dependence of the $sin\phi$ moment of the target spin asymmetry as a function of $-t$ or x_B is shown in Fig. 8.8. In the figure, both dashed and dotted curves are model calculations based on Ref[17]. The dashed curve is the full model prediction using the ξ-dependent GPD parameterization (b_{val}=b_{sea}=1, and $\mathcal{E}= \widetilde{\mathcal{E}}$=0) based on MRST02 PDFs,including leading twist terms only, and target mass corrections applied. The dotted curve shows the asymmetry when $\widetilde{\mathcal{H}}$=0. A strong x_B-dependence of the leading term $sin\phi$ is observed, in agreement with the model predictions.

Table 8.2. The target spin asymmetry of π^0 was function ϕ for each $-t$ bin and x_B bin

bins	p_0	p_1	Δp_0	Δp_1
$< -t >= 0.149$	0.0418	-0.289	0.139	0.148
$< -t >= 0.247$	0.0209	-0.366	0.121	0.135
$< -t >= 0.437$	0.185	-0.376	0.0722	0.0771
$< x_B >= 0.206$	0.0712	-0.291	0.103	0.123
$< x_B >= 0.296$	0.0937	-0.261	0.0790	0.0888
$< x_B >= 0.403$	0.384	-0.434	0.111	0.125

8.4 Summary and Outlook

Recently, the exclusive hard electroproduction of photons, i.e., Deeply Virtual Compton Scattering (DVCS), attracts strong interests from both the experimental and theoretical physicists, because it is one of the simplest processes to access general parton distributions. So far, the cross section of DVCS has been reported by H1 and ZEUS, as well as the beam spin asymmetry for DVCS reported by HERMES and CLAS. The measurements are promising, and agree well with GPDs predictions, but they are far from constraining the GPDs. There are four complex GPDs functions ($\mathcal{H}$, $\widetilde{\mathcal{H}}$, $\mathcal{E}$, and $\widetilde{\mathcal{E}}$), therefore, it is hard to constrain GPDs

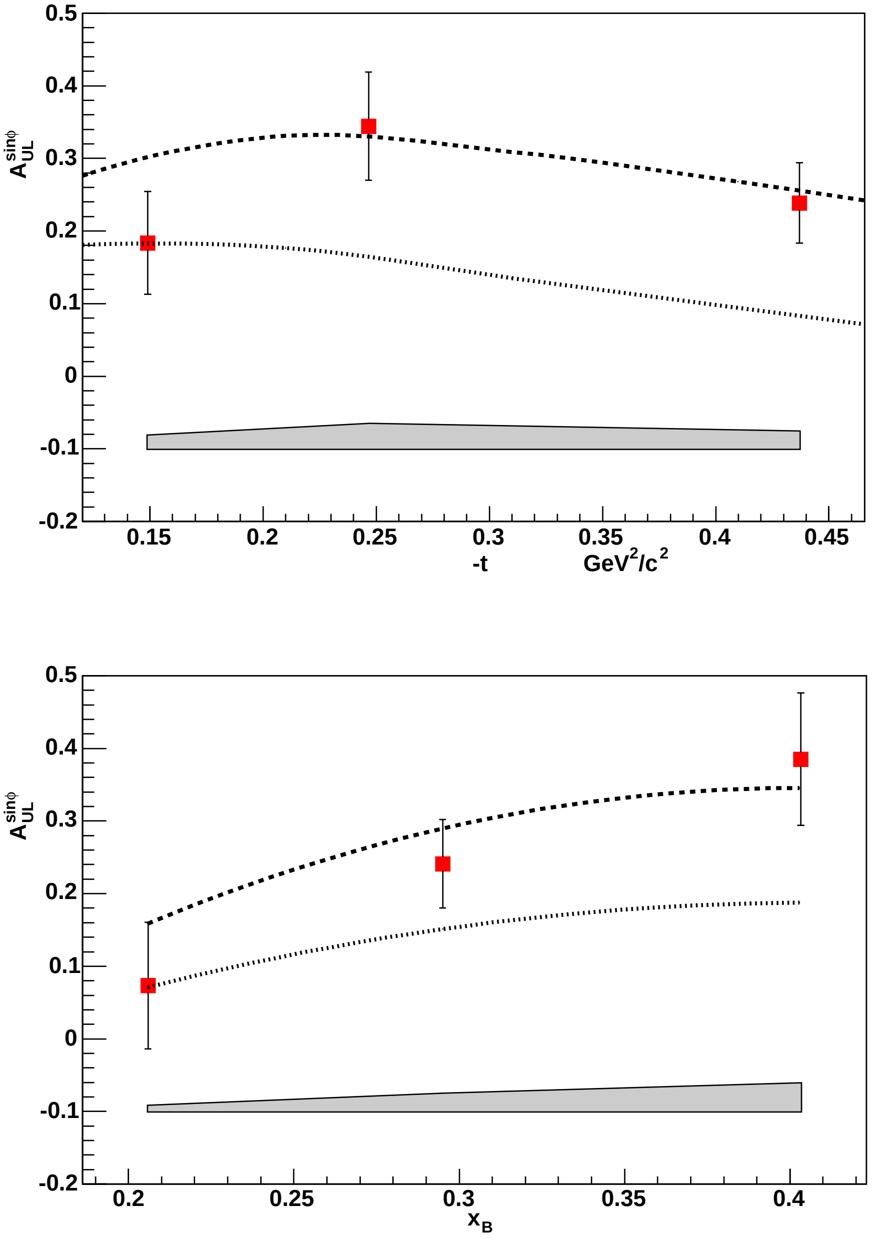

Figure 8.8. The upper panel shows the $-t$ dependence of the $sin\phi$-moment for hard exclusive electroproduction of photons, while the lower shows the x_B dependence. The dashed and dotted curves are model predictions[17].

from one experiment alone. So, a series of experiments are needed, such as diverse azimuthal asymmetries with respect to the spin and the charge.

In this analysis, the target spin asymmetry for exclusive hard electroproduction of photons has been measured for the first time, in addition, the $sin\phi$ moment of the target spin asymmetry as functions of x_B and $-t$ are studied. A significant $sin\phi$ moment of the target spin asymmetry is observed and is consistent with GPDs predictions. The asymmetry shows strong sensitivity to the polarized GPD $\widetilde{\mathcal{H}}$. A small value of $sin2\phi$ moment is observed as predicted by the GPDs theory. The leading term $A_{UL}^{sin\phi}$ has a strong x_B dependence and rises with increasing x_B, in agreement with the model prediction.

The fraction of π^0 contamination in photon productions is estimated by MC simulations. The MC simulations is compared with data, and they agree well each other. In addition, the spectra of MM_X^2 of DVCS after the pion subtraction and exclusive π^0 events are studied, the difference between their centroids is 138 MeV/c^2 with an uncertainty of 4.8 MeV/c^2, which agrees with the π^0 mass 135 MeV/c^2. This clearly shows that the pion subtraction is correct. So, we confidently trust MC simulations.

We also varied the fraction of π^0, and the results show that $sin\phi$ moment (p_0) is only slightly affected by the fraction of π^0. This can be easily understood, because most of π^0 contamination is located around 180^o in ϕ, and π^0 asymmetry is dominated by $sin2\phi$ (p_1). So, it is clear that the significant $sin\phi$ moment of the target spin asymmetry is from photon productions, not pion productions.

The measurement of the target spin asymmetry is based on EG1b data taken with a longitudinally polarized beam and a longitudinally polarized solid proton target from Sep. 2000 to Apr. 2001. The goal of EG1b experiment was to measure the proton and neutron spin structures, therefore, the polarized targets were $^{15}NH_3$ and $^{15}ND_3$, and the beam energy varied from 1.6 GeV up to 5.7 GeV. This analysis is a byproduct and based on only part of EG1b data, with 5.7 GeV beam energy and $^{15}NH_3$ target. The total run time of the data used in this analysis was 12 days, therefore, the data is limited by statistics, and does not allow the extraction of the double spin asymmetry. To decrease the statistical errors and measure the double spin asymmetry, a new proposal[8] based on this analysis was approved to measure the DVCS in Hall B at Jefferson Lab with a 6 GeV longitudinally polarized electron beam, polarized solid $^{15}NH_3$ target, and the CLAS detector with the newly built inner calorimeter[27], which is a photon detector with a polar angle coverage from 3^o to 8^o. The approved running time was 60 days at high luminosity ($1.5 \times 10^{34}\,\mathrm{cm}^{-2}\mathrm{s}^{-1}$).

The new experiment will measure the DVCS in the range of Q^2 from 1 to 4 $\mathrm{GeV}^2/\mathrm{c}^2$ and x_B from 0.15 to 0.55. The main goal will be the extraction of the target azimuthal spin asymmetry as functions of x_B and $-t$. In addition, the double spin asymmetry will be measured for the first time. Due to the inner calorimeter, the efficiency of $\vec{e}\vec{p} \to ep\gamma$ detection will be doubled. With the 5 times longer run time and double acceptance, the statistics should be 10 times of that in this analysis.

APPENDIX A

NUMBER OF OBSERVED SINGLE PHOTON EVENTS FOR EACH DATA SET

Table A.1. Number of observed single photon events from 5.6 GeV inbending data

ϕ (degree)	$N^{\Uparrow}$	$N^{\Downarrow}$	ϕ (degree)	$N^{\Uparrow}$	$N^{\Downarrow}$
$0 - 36$	10	29	$180 - 216$	19	90
$36 - 72$	4	20	$216 - 252$	12	95
$72 - 108$	7	41	$252 - 288$	14	83
$108 - 144$	14	36	$288 - 324$	5	41
$144 - 180$	20	62	$324 - 360$	6	39

Table A.2. Number of observed single photon events from 5.7 GeV inbending data

ϕ (degree)	$N^{\Uparrow}$	$N^{\Downarrow}$	ϕ (degree)	$N^{\Uparrow}$	$N^{\Downarrow}$
$0 - 36$	36	34	$180 - 216$	66	92
$36 - 72$	30	29	$216 - 252$	75	109
$72 - 108$	42	32	$252 - 288$	72	74
$108 - 144$	47	50	$288 - 324$	34	43
$144 - 180$	63	63	$324 - 360$	34	35

Table A.3. Number of observed single photon events from 5.73 GeV outbending data

ϕ (degree)	$N^{\Uparrow}$	$N^{\Downarrow}$	ϕ (degree)	$N^{\Uparrow}$	$N^{\Downarrow}$
$0-36$	11	14	$180-216$	18	16
$36-72$	17	13	$216-252$	31	45
$72-108$	48	49	$252-288$	37	58
$108-144$	50	51	$288-324$	21	28
$144-180$	42	45	$324-360$	13	23

Table A.4. Number of observed single photon events from 5.76 GeV outbending data

ϕ (degree)	$N^{\Uparrow}$	$N^{\Downarrow}$	ϕ (degree)	$N^{\Uparrow}$	$N^{\Downarrow}$
$0-36$	12	27	$180-216$	19	44
$36-72$	30	32	$216-252$	43	80
$72-108$	75	75	$252-288$	59	86
$108-144$	76	46	$288-324$	26	48
$144-180$	69	66	$324-360$	19	41

APPENDIX B

TARGET SPIN ASYMMETRY FOR OBSERVED SINGLE PHOTON EVENTS FOR EACH DATA SET

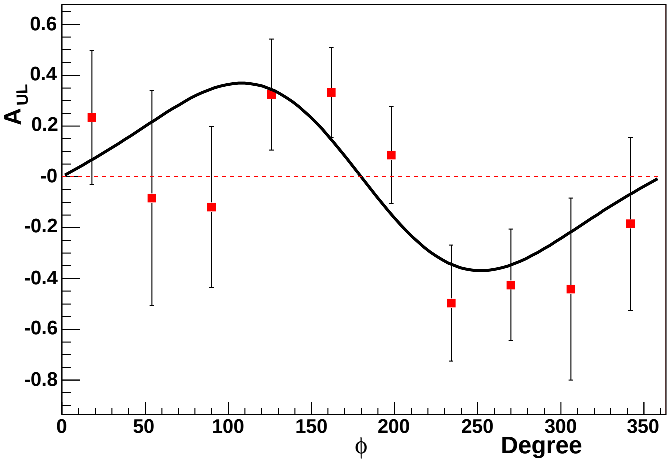

Figure B.1. The target spin asymmetry A_{UL} as a function of the azimuthal angle ϕ from 5.6 GeV inbending data. Points are fitted with function $F = p_0 sin\phi + p_1 sin2\phi$, and $p_0 = 0.347 \pm 0.125$, $p_1 = -0.067 \pm 0.122$. $< Q^2 >= 1.85$, $< -t >= 0.27$, and $< x_B >= 0.28$.

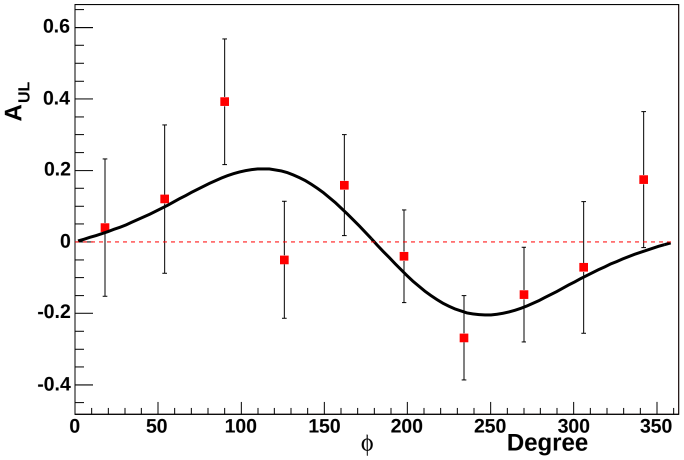

Figure B.2. The target spin asymmetry A_{UL} as a function of the azimuthal angle ϕ from 5.7 GeV inbending data. Points are fitted with function $F = p_0 sin\phi + p_1 sin2\phi$, and $p_0 = 0.182 \pm 0.071$, $p_1 = -0.051 \pm 0.073$. $< Q^2 >= 1.85$, $< -t >= 0.27$, and $< x_B >= 0.28$.

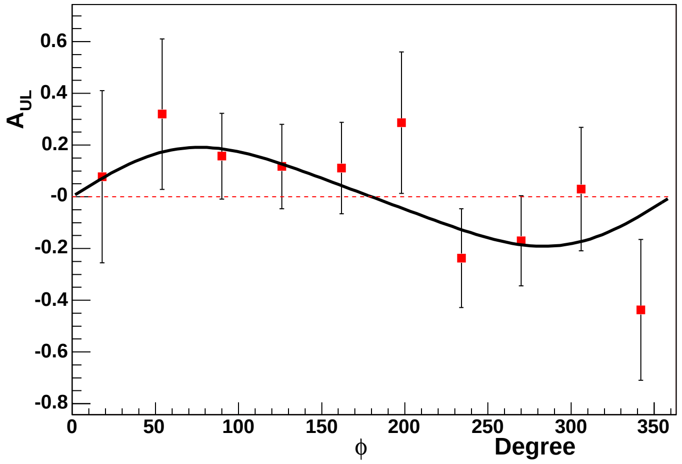

Figure B.3. The target spin asymmetry A_{UL} as a function of the azimuthal angle ϕ from 5.73 GeV outbending data. Points are fitted with function $F = p_0 sin\phi + p_1 sin2\phi$, and $p_0 = 0.185 \pm 0.088$, $p_1 = 0.024 \pm 0.099$. $< Q^2 >= 1.87$, $< -t >= 0.31$, and $< x_B >= 0.29$.

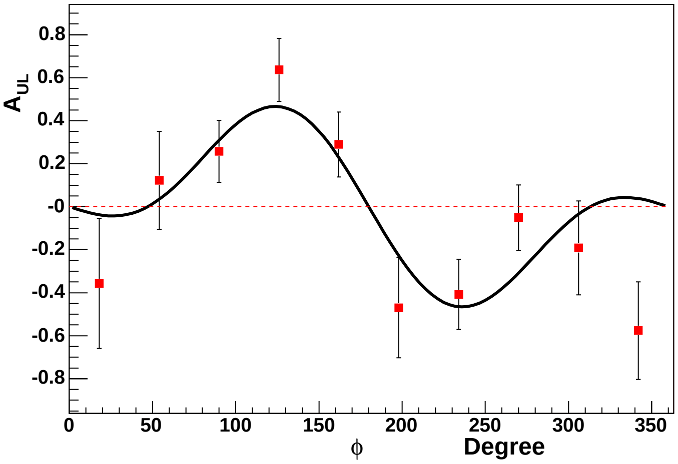

Figure B.4. The target spin asymmetry A_{UL} as a function of the azimuthal angle ϕ from 5.76 GeV outbending data. Points are fitted with function $F = p_0 sin\phi + p_1 sin2\phi$, and $p_0 = 0.309 \pm 0.076$, $p_1 = -0.227 \pm 0.086$. $< Q^2 >= 1.87$, $< -t >= 0.31$, and $< x_B >= 0.29$.

APPENDIX C

NUMBER OF π^0 EVENTS FOR EACH DATA SET

Table C.1. Number of π^0 events from 5.6 GeV inbending data

ϕ (degree)	$N^{\Uparrow}$	$N^{\Downarrow}$	ϕ (degree)	$N^{\Uparrow}$	$N^{\Downarrow}$
$0-36$	0	1	$180-216$	12	26
$36-72$	3	5	$216-252$	18	48
$72-108$	6	11	$252-288$	10	21
$108-144$	20	9	$288-324$	3	4
$144-180$	23	16	$324-360$	3	3

Table C.2. Number of π^0 events from 5.7 GeV inbending data

ϕ (degree)	$N^{\Uparrow}$	$N^{\Downarrow}$	ϕ (degree)	$N^{\Uparrow}$	$N^{\Downarrow}$
$0-36$	4	5	$180-216$	38	35
$36-72$	11	12	$216-252$	33	46
$72-108$	18	10	$252-288$	21	17
$108-144$	26	21	$288-324$	12	9
$144-180$	24	26	$324-360$	6	2

Table C.3. Number of π^0 events from 5.73 GeV outbending data

ϕ (degree)	$N^{\Uparrow}$	$N^{\Downarrow}$	ϕ (degree)	$N^{\Uparrow}$	$N^{\Downarrow}$
$0-36$	0	4	$180-216$	5	12
$36-72$	5	3	$216-252$	26	29
$72-108$	25	24	$252-288$	30	30
$108-144$	37	26	$288-324$	8	12
$144-180$	24	17	$324-360$	4	2

Table C.4. Number of π^0 events from 5.76 GeV outbending data

ϕ (degree)	$N^{\Uparrow}$	$N^{\Downarrow}$	ϕ (degree)	$N^{\Uparrow}$	$N^{\Downarrow}$
$0-36$	1	2	$180-216$	7	11
$36-72$	2	6	$216-252$	21	55
$72-108$	39	32	$252-288$	30	43
$108-144$	40	32	$288-324$	16	9
$144-180$	23	16	$324-360$	5	6

APPENDIX D

THE FRACTION OF π^0 CONTAMINATIONS IN OBSERVED SINGLE PHOTON EVENTS

Table D.1. The fraction of π^0 for $< -t >= 0.149 GeV^2/c^2$

ϕ (degree)	f_{π^0}	Δf_{π^0}	ϕ (degree)	f_{π^0}	Δf_{π^0}
$0 - 36$	0.098	0.008	$180 - 216$	0.287	0.019
$36 - 72$	0.058	0.005	$216 - 252$	0.201	0.015
$72 - 108$	0.173	0.013	$252 - 288$	0.192	0.014
$108 - 144$	0.262	0.018	$288 - 324$	0.108	0.009
$144 - 180$	0.320	0.020	$324 - 360$	0.104	0.009

Table D.2. The fraction of π^0 for $< -t >= 0.247 GeV^2/c^2$

ϕ (degree)	f_{π^0}	Δf_{π^0}	ϕ (degree)	f_{π^0}	Δf_{π^0}
$0 - 36$	0.173	0.013	$180 - 216$	0.307	0.020
$36 - 72$	0.084	0.007	$216 - 252$	0.292	0.019
$72 - 108$	0.229	0.017	$252 - 288$	0.185	0.014
$108 - 144$	0.294	0.019	$288 - 324$	0.077	0.007
$144 - 180$	0.372	0.022	$324 - 360$	0.062	0.005

Table D.3. The fraction of π^0 for $< -t >= 0.437 GeV^2/c^2$

ϕ (degree)	f_{π^0}	Δf_{π^0}	ϕ (degree)	f_{π^0}	Δf_{π^0}
$0 - 36$	0.097	0.008	$180 - 216$	0.481	0.023
$36 - 72$	0.191	0.014	$216 - 252$	0.412	0.023
$72 - 108$	0.374	0.022	$252 - 288$	0.269	0.018
$108 - 144$	0.448	0.023	$288 - 324$	0.085	0.007
$144 - 180$	0.552	0.023	$324 - 360$	0.062	0.005

Table D.4. The fraction of π^0 for $< x_B >= 0.206$

ϕ (degree)	f_{π^0}	Δf_{π^0}	ϕ (degree)	f_{π^0}	Δf_{π^0}
$0 - 36$	0.093	0.009	$180 - 216$	0.367	0.022
$36 - 72$	0.015	0.001	$216 - 252$	0.278	0.019
$72 - 108$	0.292	0.019	$252 - 288$	0.192	0.015
$108 - 144$	0.321	0.020	$288 - 324$	0.129	0.011
$144 - 180$	0.392	0.022	$324 - 360$	0.132	0.011

Table D.5. The fraction of π^0 for $< x_B >= 0.296$

ϕ (degree)	f_{π^0}	Δf_{π^0}	ϕ (degree)	f_{π^0}	Δf_{π^0}
$0 - 36$	0.103	0.009	$180 - 216$	0.344	0.021
$36 - 72$	0.103	0.009	$216 - 252$	0.324	0.021
$72 - 108$	0.258	0.018	$252 - 288$	0.213	0.016
$108 - 144$	0.340	0.021	$288 - 324$	0.102	0.009
$144 - 180$	0.405	0.022	$324 - 360$	0.082	0.007

Table D.6. The fraction of π^0 for $< x_B >= 0.403$

ϕ (degree)	f_{π^0}	Δf_{π^0}	ϕ (degree)	f_{π^0}	Δf_{π^0}
$0 - 36$	0.136	0.011	$180 - 216$	0.244	0.017
$36 - 72$	0.120	0.010	$216 - 252$	0.280	0.019
$72 - 108$	0.263	0.018	$252 - 288$	0.228	0.016
$108 - 144$	0.384	0.022	$288 - 324$	0.074	0.006
$144 - 180$	0.492	0.023	$324 - 360$	0.072	0.006

REFERENCES

[1] R. Hofstadter, *Ann. Rev. Nucl. Sci.* **7**, 231 (1957).

[2] F.M. Dittes *et al.*, *Phus. Lett. B* **209**, 325 (1988).

[3] D. Müller *et al.*, *Fortschr. Phys.* **42**, 2101 (1994).

[4] X. Ji, *Phys. Rev. Lett.* **78**, 610 (1997).

[5] A.V. Radyushkin, *Phys. Lett. B* **380**, 417 (1996).

[6] S. Stepanyan *et al.*, *Phys. Rev. Lett.* **87**, 182002 (2001).

[7] A. Airapetian *et al.*, *Phys. Rev. Lett.* **87**, 182001 (2001).

[8] L. Elouadrhiri *et al.*, "Deeply Virtual Compton Scatterng (DVCS) at 6 GeV with polarized beam and polarized target using the CLAS detector", Proposal 05-114 at Jefferson Lab.

[9] http://www.jlab.org/Hall-B/clas12/

[10] N. Bianchi and R. Jakob, *CERN Courier*, **V42**, N6 (2002), http://www.cerncourier.com/main/article/42/6/16.

[11] A. Belitsky, X. Ji, F. Yuan, *Phys. Rev. D* **69**, 074014 (2004).

[12] A. Belitsky and A. Radyushkin, *Phys. Rept.* **418**, 1 (2005).

[13] M. Burkardt, *Int.J.Mod.Phys.A* **18** 173-208 (2003); M. Burkardt, hep-ph/0509316.

[14] M. Diehl *Phys. Rep.* **41**, 388 (2003).

[15] X. Ji *Annu. Rev. Nucl. Part. Sci.* **54**, 413 (2004).

[16] K. Goeke, M. Poliakov, and M. Vanderhaeghen, *Prog. Part. Nucl. Phys.* **47**, 401 (2001).

[17] M. Vanderhaeghen *et al.*, *Phys. Rev. D* **60**, 094017 (1999).

[18] A. Belitsky, D. Müller, and A. Kirchner, *Nucl. Phys. B* **629**, 323 (2002).

[19] A. Belitsky and D. Müller, *Phys. Lett. B* **417**, 129 (1998).

[20] X. Ji and J. Osborne, *Phys. Rev. D* **58**, 094018 (1998).

[21] L. Mankiewicz *et al.*, *Phys. Lett. B* **425**, 196 (1998).

[22] C. Adloff *et al.*, *Phys. Lett. B* **517**, 47 (2001).

[23] A. Aktas *et al.*, arXiv:hep-ex/0505061.

[24] S. Chekanov *et al.*, *Phys. Lett. B* **573**, 46 (2003).

[25] F. Ellinghaus, arXiv:hep-ex/0410094.

[26] B. Krauss, arXiv:hep-ex/0505016.

[27] D. Doughty *et al.*, "Deeply Virtual Compton Scatterng (DVCS) with CLAS at 6 GeV", Proposal 01-113 at Jefferson Lab.

[28] D.I. Sober *et al.*, *Nucl. Instr. and Meth.* **A 440**, 263 (2000).

[29] M.D. Mestayer *et al.*, *Nucl. Instr. and Meth.* **A 449**, 81 (2000).

[30] D.S. Carman *et al.*, *Nucl. Instr. and Meth.* **A 419**, 315 (1998).

[31] L.M. Qin *et al.*, *Nucl. Instr. and Meth.*, **A 411**, 265 (1998).

[32] E.S. Smith *et al.*, *Nucl. Instr. and Meth.*, **A 432**, 265 (1999).

[33] M. Amarian *et al.*, *Nucl. Instr. and Meth.*, **A 460**, 460 (2001).

[34] S. Taylor *et al.*, *Nucl. Instr. and Meth.*, **A 447**, 424 (2000).

[35] G. Adams *et al.*, *Nucl. Instr. and Meth.*, **A 465**, 414 (2001).

[36] http://www.jlab.org/ shifeng

[37] B.A. Mecking *et al.*, *Nucl. Instr. and Meth.*, **A 503**, 513 (2003).

[38] C.D. Keith *et al.*, *Nucl. Instr. and Meth.*, **A 501**, 327 (2003).

[39] R.De Vita, "Measurement of the double spin asymmetry in π^+ electroproduction with CLAS", PHD Thesis, University of Genova, (2000).

[40] Y. Prok, "Measurement of the spin structure function $g_1(x, Q^2)$ of the proton in the resonance region", PHD Thesis, University of Virginia, (2004).

[41] V. Burkert, *et al.*, "Charged Particle Identification in Electron Scattering Experiments with CLAS", CLAS-NOTE 2002-006.

[42] A. Klimenko and S. Kuhn, "Momentum Corrections for E6", CLAS-NOTE-2003-005.

[43] V. Burkert, *Private Communication.*

[44] Vipuli G. Dharmawardane, Spin Structrue Functions of the Deuteron Measured with CLAS in and above the Resonance Region, *Ph.D. Thesis*,Old Dominion University,(2004).

[45] A. Vlassov, http://www.jlab.org/ vlassov/cc/index.htm

[46] C.D. Keith *et al.*, *Nucl. Instr. and Meth. A* **501**, 327 (2003).

[47] R. De Vita, *Private Communication.*

[48] M. Anghinolfi, M. Battaglieri, R. De Vita, "Measure of the target per beam polarization in EG1 data", CLAS-NOTE-2000-001.

[49] T. W. Donnelly and A. S. Raskin, *Ann. Phys.* **169**, 247 (1986).

[50] A. Biselli,*et al. Phys. Rev. C* **68**, 035202 (2003).

[51] P. E. Bosted, *Phys. Rev. C* **51**, 409 (1995).

[52] P. E. Bosted, "Spin structure functions g_1^p and g_1^d from Eg1b at 1.x and 5.x GeV", CLAS ANALYSIS NOTE 2004-112.

[53] P. E. Bosted, *Private Communication.*

[54] R. De Vita, M. Anghinolfi, "Measurement of the Double Spin Asymmetry in π^+ electroproduction with CLAS", *CLAS-ANALYSIS*, (2001).

[55] A. Biselli, "Study of the $\Delta(1232)$ using double polarization asymmetries", *CLAS-ANALYSIS*, (2002).

[56] A. Biselli, "Double and target asymmetries for $\vec{e}\vec{p} \to e'p\pi^0$ from EG1b data",*CLAS-ANALYSIS*, (2005).

[57] V. A. Korotkov, W.-D. Nowak, *Eur. Phys. J.* **C23**, 455 (2002).

[58] X. Ji, W. Melnitchouk, X. Song, *Phys. Rev. D* **56**, 5511 (1997).

[59] P. A. M. Guichon *et al.* hep-ph/0305231

[60] J. Pochodzalla *et al.* hep-ph/9909534

[61] C. Smith, *Private Communication.*

[62] D. G. Crabb *et al.*, *Nucl. Instr. and Meth.* **356**, 9 (1996).

[63] M. Goldman, *Spin temperature and nuclear magnetic resonance in solids,* Oxford Clarendon Press (1970).

[64] A. V. Afanasev, M. I. Konchatnij and N. P. Merenkov, Preprint JLAB-PHY-05-379, [arXiv:hep-ph/0507059 v1]

BIOGRAPHICAL SKETCH

Shifeng Chen

Shifeng Chen is from Shan-Dong Province, P. R. China. He did his undergraduate studies at Tsinghua University, Beijing, P. R. China, where he received a Bachelor of Engineering in engineering physics in July 1997. That fall he entered the master program of the nuclear energy and technology at Tsinghua University, and received his Master of Engineering degree in July 2000. He was accepted in the doctoral program of the physics department at Florida State University in Fall 2000. He received a Master of Science degree in spring 2002 from Florida Stat University. This dissertation was defended on February 28, 2006 at Florida State University.